Design and Characterization of a Flame Spray Pyrolysis Apparatus to Compare Soot Emissions from Liquid Fuels

by

Jason Scott

A thesis submitted to the Faculty of Graduate and Postdoctoral Affairs in partial fulfillment of the requirements for the degree of

Master of Applied Science

in

Aerospace Engineering

Carleton University
Ottawa, Ontario

Abstract

This study investigates flame spray pyrolysis (FSP) as a simple bench-top tool for comparison of soot emissions from different liquid jet fuels. A sampling assembly is designed for soot collection and particle property analysis. Soot agglomerate size distributions and elemental to total carbon ratios (EC/TC) are measured for three liquid fuels and flame conditions with Reynolds numbers and burner equivalence ratios ranging from 6000 to 9100 and 6.7 to 13.1. Day-to-day variations in the dilution ratio resulted in up to 20% variability in the measured total agglomerate number density and mobility diameters. Geometric mean primary particle ($\overline{d_p}$) and mobility diameter ($\overline{d_m}$) values are below 21 and 113 nm, respectively, in excellent agreement with those emitted from jet engines and earlier works using FSP. EC/TC is higher than 0.8 for all flames burning Jet A1, but values as low as 0.55 are measured for soot emitted from SAF burning flames.

Acknowledgements

The research leading to these results has received funding from the Canada Research Chair Program (Grant # CRC-2019-232527), the Natural Sciences and Engineering Research Council of Canada (Discovery Grant # RGPIN-2019-06330), Early Career Supplemental Award # DGECR-2019-00220, and the National Research Council Canada.

Special thanks to my supervising professor, Reza Kholghy, for the endless support towards my research and academic growth, and for providing me with the tools and guidance to complete this thesis.

Thank you to the entire team at the Energy and Particle Technology Laboratory of Carleton University, for their guidance and support throughout my entire program.

Thank you to Prem Lobo, Greg Smallwood, Dan Clavel, Brett Smith, Simon-Alexandre Lussier, Joel Corbin, and the entire Black Carbon Metrology team at the National Research Council Canada for supporting this project with the lab space, personnel support, and resources for assembly and testing.

Thank you to Alex Proctor and the team of technicians at the Carleton University machine shop for design support and specific component manufacturing for this test assembly.

Table of Contents

List of Tables

List of Figures

Nomenclature

Acronym	Description
APU	Auxilary Power Unit
ATJ	Alcohol to Jet
ATJ-SPK	Alcohol to Jet Synthetic Paraffinic Kerosene
DMA	Differential Mobility Analyzer
EI	Emission Index
FSP	Flame Spray Pyrolysis
FT-SKA	Fischer-Tropsch Synthetic Kerosene with Aromatics
FT-SPK	Fischer-Tropsch Synthetic Paraffinic Kerosene
HAB	Height Above Burner
HEFA	Hydrotreated Esters and Fatty Acids
HiaT	Hole-in-a-Tube
ICAO	International Civil Aviation Organization
IPCC	Intergovernmental Panel on Climate Change
LII	Laser Induced Incandescence
LS-FSR	Lab-scale Flame Spray Reactor
MAC	Mass Absorption Cross Section [m^2/g]
MW	Molecular Weight [g/mol]
NJFCP	National Jet Fuels Combustion Program
NRC	National Research Council Canada
nvPM	non-volatile particulate matter
PM	Particulate Matter
SAE	Society of Automotive Engineers
SAF	Sustainable Aviation Fuel
SIP	Synthesized Iso-Paraffinic
SMPS	Scanning Mobility Particle Sizer
SN	Smoke Number
TEM	Transmission Electron Microscopy
TOA	Thermal Optical Analysis

Chemical Symbols	Description
CO_2	Carbon Dioxide
CH_4	Methane
$C_{11.4}H_{21.7}$	Jet A1
$C_{9.7}H_{18.7}$	C10
$C_{12.5}H_{27.1}$	ATJ
O_2	Oxygen
H_2O	Water

Latin Symbols	**Description**
D_g	Diameter of gas stream [mm]
D_l	Diameter of liquid stream [mm]
d_m	Mobility diameter [nm]
$\overline{d_m}$	Geometric mean mobility diameter [nm]
d_p	Primary particle diameter [nm]
$\overline{d_p}$	Geometric mean primary particle diameter [nm]
$\bar{h}$	Arithmetic Average Flame height [mm]
Kn	Knudsen Number
M	Momentum flux ratio per unit volume
N_{tot}	Total number concentration [#/cm^3]
Re_{eff}	Effective Reynolds number
Re_g	Reynolds number of gas flow
Re_l	Reynolds number of liquid flow
U_g	Velocity of gas [m/s]
U_l	Velocity of liquid [m/s]
v_g	Kinematic viscosity of gas [mm^2/s]
v_l	Kinematic viscosity of liquid [mm^2/s]
$\bar{x}$	Arithmetic average geometric mean mobility diameter [nm]

Greek Symbols	**Description**
Φ	Overall equivalence ratio
λ	Mean free path [nm]
ρ_g	Density of gas [g/cm^3]
ρ_l	Density of liquid [g/cm^3]
σ	Standard deviation
σ_g	Geometric standard deviation

Chapter 1: Introduction

1.1 Background

Soot is a byproduct of the incomplete combustion of hydrocarbon fuels and a significant contributor to global warming when emitted into the atmosphere [1]. Every year, over 6.6 megatonnes of soot particles are released into the atmosphere from anthropogenic (e.g., transportation, flaring, heating, and industrial activities), and natural (forest fires) sources [2]. This makes soot the third largest contributor to global warming with a direct radiative forcing of 0.11 W/m^2, resulting in a 0.1°C increase in the global mean surface temperature of the earth [3]. Aviation has a strong impact on global soot emissions at high altitudes [4], contributing up to 50% of soot emissions near the tropopause [5]. These high-altitude soot particulate emissions have an increased ability to absorb and retain radiation energy before they settle compared to similar soot emitted at lower altitudes or around sea level [3]. Soot is considered a short-lived climate pollutant [2] and therefore, reducing soot emissions can have an immediate impact on global warming and delay climate change [6]. This reduction of short-lived soot particles could immediately reduce their overall effective radiative forcing and effect on global mean surface temperature. In a 2021 report, the Intergovernmental Panel on Climate Change (IPCC) classified soot as the third highest contributor to global warming [3], however, recent work by Kelesidis et. al states that the IPCC may have significantly underestimated the radiative forcing effects of atmospheric soot due to inaccurate models of soot morphology and optical properties [6]. Meaning, the effects of soot on global warming could be stronger than currently reported and need to be further studied and reduced to limit their adverse environmental effects.

To mitigate soot emission at high altitudes, the International Civil Aviation Organization (ICAO) has regulated non-volatile particulate matter (nvPM) emissions, which includes soot, from jet engines exceeding 26.7 kN of thrust [7]. Engines rated >26.7kN of thrust are primarily used for commercial passenger and freight aircraft which tend to dominate airport and total aircraft emissions [7]. ICAO also controls regulations on aircraft with <26.7kN of thrust. However, the ICAO's most recent standardized regulation on nvPM emissions is for aircraft with thrust >26.7kN.

Improvements in aircraft fuel efficiency and air traffic control for efficient and sustainable air travel have led to carbon emission reductions up to, but not exceeding, 15% [8]. However, Boeing has estimated that operating a commercial jet engine on a biojet fuel could reduce its carbon emissions by up to 80% compared to conventional fossil fuels, through an airplane lifecycle [8]. A sustainable aviation fuel (SAF) is any fuel that is produced from a sustainable feedstock. Biojet fuels are a specific category of SAF that are produced from a biomass feedstock. Research in biojet fuels is in the early stages and most production techniques require four or more functional process units, which refers to the steps required to refine the fuel from its base source to an operational liquid fuel. Early stage four-step (or more) fuels require processing steps such as addition of sugars, fatty acids, fermentation, and other processes before a biojet fuel is produced. This is because the feedstock mixture includes a variety of biomasses that require specific treatments. This increases cost, energy, and labor to commercialize a new fuel. However, technology for lignin-based (complex organic polymers found in biomass) biojet fuels, where the starting feedstock is strictly lignocellulosic biomass, show very promising results due to its one step conversion process requiring only a hydrodeoxygenation to convert to the feedstock to long-chain hydrocarbons, making its production cost more comparable to that of fossil fuels [8]. As of 2021, Jet A/A1 is the only fuel source allowed to power commercial aircraft, but there are currently five main biojet fuel technologies that have met ASTM D7566 specification standards. This standard allows a SAF to be blended with Jet A or Jet A1 and used to operate a non-commercial aircraft. Those fuels are Fischer-Tropsch Kerosenes (FT-SPK and FT-SKA), Hydrotreated Esters and Fatty Acids (HEFA), Synthesized Iso-Paraffinic (SIP), and Alcohol (isobutanol) to Jet Synthetic Paraffinic Kerosene (ATJ-SPK). The sources of these fuels are outlined in Table 1.1.

Table 1.1: Approved biojet fuels for mixture with Jet A/A1 and their sources [8]

Approved Alternative Fuel for Mixture	Source
Fischer-Tropsch Synthetic Paraffinic Kerosene (FT-SPK)	Lignocellulosic biomass, municipal solid waste
Fischer-Tropsch Synthetic Kerosene with Aromatics (FT-SKA)	Lignocellulosic biomass
Hyrdotreated Esters and Fatty Acids (HEFA)	Vegetable oil, animal fat, recycled oil
Synthesized Iso-Paraffinic (SIP)	Juice, lignocellulosic biomass
Alcohol (isobutanol) to Jet Synthetic Paraffinic Kerosene (ATJ-SPK)	Lignocellulosic biomass and starch

SAFs are advantageous for minimizing global harmful effects caused by the aviation industry as they directly reduce CO_2 by emitting recycled CO_2 that has already been absorbed by the biomass used in the fuel feedstock. Fossil fuels add to the overall increase of CO_2 by emitting carbon that has previously been locked away in the earth's surface. Soot emissions can also be reduced using SAFs because their chemical composition typically has lower mass percentages of poly-cyclic aromatics and cyclo-alkanes compared to conventional fossil-fuel aviation fuels. Reducing aromatics and cyclo-alkanes often lead to a decrease in soot emissions when the fuel is combusted [9]. However, SAF production processes require expensive testing and evaluation before implementing as a mixture approved for drop-in fuel [10]. Ideally, compatible drop-in SAFs are the end goal, to reduce overhauls of current operational engines and components.

When a fuel is developed, it must complete the Standard Practice for Qualification and Approval of New Aviation Turbine Fuels and Fuel additives, also known as ASTM D4054, before the fuel is cleared for drop-in use. This process is broken into four different tiers followed by a research report that is either accepted or rejected for ASTM specification. Tiers 1 and 2 include fuel property analysis and fit-for-purpose property tests. These tests check whether the fuel produces sufficient energy release when combusted, but also meet other jet fuel interdependencies such as acting as a coolant, seamlessly working with current pumps and seals, remain stable in long-term storage, and react safely under severe operability conditions [10]. Tiers 1 and 2 remain relatively inexpensive, do not require large volumes of fuel, and can be completed within six months [10]. Examples of these tests include two-dimensional gas chromatography (GCxGC) to quantify the chemical composition of the hydrocarbons in each fuel, and surrogate modelling with simplified mixtures to identify important reaction pathways that control combustion [11]. More recently, hybrid approaches, like the one seen in the JETSCREEN program [11], where kinetic models are numerically optimized and fine-tuned for specific fuel palettes, have been used to help estimate sooting tendencies and emissions for developing fuels [10]. The JETSCREEN program specifically focused on safety, environmental, and operation-related subprocesses. One example of their findings was that lowering aromatic contents reduced soot emissions significantly; however, it increased risk of O-ring shrinkage and fuel leaks

[12]. Tier 3 consists of fuel compatibility tests with specific components followed by engine/APU testing in tier 4. This phase can take much longer (2-3 years) and increases testing costs as more personnel, equipment, and large volumes of fuel are required [10]. JETSCREEN's hybrid approach has shown potential for synthesizing and identifying soot from a variety of jet fuels by using flow reactor experiments and burning velocity measurements with the help of kinetic modelling [11]. However, this study focuses more on fuel reactivity and does not identify the properties of produced soot particles such as their size, composition, mass, and optical properties.

These are important properties when considering the harmful effects of jet fuel emissions on the environment. For example, mobility diameter, d_m, size distributions of soot particles govern their transport properties [13] while their primary particle diameter, d_p, is inversely proportional to their specific surface area that is linked to the toxicity of soot particles [13]. Another important property of soot particles is their mass absorption cross section (MAC) which defines the direct radiative forcing of soot particles in the atmosphere and is strongly dependent on the soot particle mass and the number of primary particles in each agglomerate [14]. Most studies that identify these properties are utilizing test techniques from tier 3 and 4, with full-size engines, requiring expensive resources and longer timeframes. For example, in 2011, Lobo et. al used a CFM56-7B commercial jet engine to burn conventional Jet A1 and biomass-based fuels to measure particulate matter (PM) number and size distributions [15]. That study identified potential for large PM emission reductions at the engine exit plane by using alternative fuels with low aromatic content, high hydrogen to carbon ratios and low viscosities. However, the fuels tested did not meet current ASTM standards for aviation fuel and could not be certified as replacement fuels.

In 2019, a CFM56-5C4 engine was used by Schripp et al. to compare particle mobility size distributions for Jet A1 and Gevo alcohol-to-jet (ATJ) fuels, like the ones used in this work, where Jet A1 geometric mean mobility diameters, $\overline{d_m}$, ranged from 13-39 nm and ATJ $\overline{d_m}$ from 13-35 nm in ground idle to takeoff conditions [16]. It was concluded that alternative jet fuels do not necessarily reduce CO_2 emissions, but affirmed that fuels with little to no aromatics, like the ATJ fuel, will achieve reduction in PM emissions.

More recently in 2021, a study by Durdina et al. looked at mobility size distributions of soot from a CFM56-7B26 engine operating on Jet A1 vs. a 32% hydrotreated esters and fatty acids (HEFA-SPK) blended (with Jet A1) fuel, where $\overline{d_m}$ ranged from ≈8-40 nm for both fuels [17]. That study provided evidence for the improvement of air quality around airports by using SAFs that reduce PM emissions. They found reductions in nvPM mass and number emissions by as much as 20% and 25%, respectively. Full-sized engine testing like the ones mentioned above require large volumes of fuel and the main challenge faced in the fuel screening process, especially in tiers 3 and 4, is to extract as much information from as little fuel as possible and minimize the need for full size engine tests [8].

1.2 Sampling

Soot particle mobility diameters found in aviation emission plumes are most often in the nanoscale region [18] and can be sampled and analyzed with a variety of techniques, depending on the design of the experiment. Sampling probes are used to draw soot samples directly from the primary emission flow or plume exiting a jet engine or open flame.

Wey et al. [19] sampled and analyzed exhaust plumes from a stationary DC-8 aircraft operating with a CFM56-2C1 engine. Soot mobility size distributions and emission indices (EI) were analyzed and calculated at different jet fuel flow rates and distances from the engine exhaust exit plane. An EI gives quantification to the mass- or number-based concentration of an emitted gas or PM per mass of the fuel. In this experiment, sampling was done with a probe rake that had a total of 18 individual probes: 6 gas, 6 particle, and 6 external probes, where the external probes were used for raw sample collection with no integrated dilution. The gas and particle probes were designed with concentric flow of dry nitrogen, downstream of the probe tip, to quickly dilute the entering collected sample to limit condensation, agglomeration, and gas to particle conversion processes. The external probes were used when the rake was positioned 30 m away from the exhaust exit plane to sample the plume without dilution gas. The sample rake also used water-cooling to protect particle and gas samples from thermal degradation as the sample travelled through the probe.

Lobo, Hagen, and Whitefield [20] used the same sampling rake and compared PM emissions from a commercial jet engine (CFM56-7B) mounted in an open-air test cell with varying mixtures of conventional, biomass, and Fischer-Tropsch fuels. Here, the engine thrust settings were adjusted, and particle size distributions were compared for varying fuel mixture percentages at different thrust levels. Soot mobility size distributions were successfully measured with the rake sampling probe from Wey, et al. [19]. Mass and number EIs were calculated and compared between the different fuels and thrust settings. Alternative fuel candidates used in this study provided potential for large PM emissions reductions compared to conventional Jet A1.

Lobo et al. [21] used a similar multipoint rake-style sampling probe to extract gaseous and PM emissions of a small (<26.7 kN thrust) mixed turbofan aircraft engine. Both diluted and undiluted samples were measured by switching the flow through different sampling paths. The diluted path used a Dekati DI-1000 ejector diluter to dilute samples with filtered dry nitrogen by a factor of 8-13. Soot mobility size distributions and PM number- and mass-based EIs were defined for varying engine thrust settings in the landing take-off cycle, using Jet A1 and SPK.

Christie et al. [22] experimented with a Garrett Honeywell GTCP85-129 auxiliary power unit (APU), often used on a Boeing 737, to find a correlation between PM emissions and Smoke Number (SN) using conventional and alternative fuels. Gas turbine APUs offer a good model for main aircraft engine combustion characteristics and are considerably less expensive to operate [22]. SN is a way of estimating soot emissions from a given source. Measurement of SN is done by placing a filter in way of the primary smoke flow and measuring the reduction in reflectance of the filter caused by the smoke blackening the surface. To collect soot and gas samples, Christie et al. used two single point probes (one for PM emissions and one for gas emissions), side-by-side, placed ~0.15 m from the engine exit plane. Downstream of the PM sampling probe, a Dekati ejector diluter (model DI-

1000) was added to the flow path to dilute the PM sample with particle-free dry nitrogen. Samples were corrected for dilution and line losses. PM size and mass- and number-concentrations, as a function of SN, were identified for conventional, alternative, and mixed fuels.

Kinsey et al. [23] compared multiple configurations of a sampling rake, placed within 8 m of the engine exhaust plane, for both gas and nvPM collection from a J85-GE-5 turbojet engine. Samples were diluted downstream, after collection at the engine exhaust, by an ejector diluter (Dekati DI-1000 or equivalent) with filtered nitrogen or air, achieving dilution ratios of 8-14. Analysis instruments for measuring nvPM mass, size, and number concentrations were used to get soot mobility size distributions, and nvPM number and mass concentrations. Configurations within the sampling assembly were adjusted to compare variabilities within the analyzed samples when dilution, sample paths, and fuels were changed.

In another experiment, Lobo et al. [24] completed a comparison study between common standardized sampling and measurement reference systems for aircraft engine nvPM emissions. In this study they used two exhaust sampling probe assemblies placed within 1 m of the exhaust exit plane and with 8 mm inner diameters. One of the sampling probes was made from Inconel 625 alloy and had a cruciform design with six sampling orifices on each of the four arms. Orifices were systematically positioned radially from the center of the cruciform. The multiple orifice positions provided various configurations for sampling positions within the exhaust stream. The other sampling probe was made from Inconel 600 alloy and was placed 0.8 m away from the exhaust exit plane. The collected sample travelled through the probes before being split to three different measurement reference systems: Swiss (developed by Empa), North American (developed by Missouri University of Science and Technology), and European (developed by Cardiff University). In this study, samples were not diluted in the probe, but diluted at the beginning of each measurement reference system by a Dekati DI-1000 ejector diluter. This way, samples could be pulled off the first sample line for raw emission measurement without dilution.

Table 1.2: Sampling probe literature review summary table for aviation engines.

Authors	Sampling Probe	Distance from exhaust exit plane	Dilution Ratio for PM*	Emission Source	Measurements
Wey et al. [19]	Sampling rake with water-cooled stainless-steel PM probe	1, 10, 30 m	10 at 10 m 30 at 30 m (ambient air) 8-13 (controlled N_2)	Exhaust flow of CFM56-2C1 engine on chocked DC-8 aircraft	Soot mobility size distributions, PM and gas EIs
Lobo, Hagen, Whitefield [20]		1 m	> 10	Core exhaust flow of CFM56-7B engine in open air test cell	Soot mobility size distributions, soot EI
Lobo et al. [21]	Rotating multipoint probe for gaseous and PM emissions	Within half exhaust nozzle diameter	8-13 (Dekati DI-1000)	Small mixed turbofan aircraft engine (<26.7 kN thrust)	Soot mobility size distributions, PM mass- and number-EI
Christie et al. [22]	Side-by-side single point probes for gaseous	~0.15 m	Dekati DI-1000	GTCP85-129 APU	Smoke number, PM size, mass concentration,

	and PM emissions				number concentration
Kinsey et al. [23]	Sampling rake for gas and PM collection	N/A	8-14 (Dekati DI-1000)	J85-GE-5 turbojet engine	Soot mobility size distributions, PM number and mass concentrations
Lobo et al. [24]	Cruciform with 6 sampling orifices	1 m	8-14 (Dekati DI-1000)	CFM56-7B26/3	Soot mass, PM EI, Soot mobility size distributions

*Dilution ratios noted in this column either take place at the probe inlet, due to the sampling probe design, or are caused by diluters added to the flow path downstream from collection (e.g., Dekati diluter).

Dilution of PM sample flows is often used to limit unwanted conversion processes, such as coagulation and thermophoretic wall losses [25], while the particles travel to analysis instruments. Overall, in the case of jet engine testing, dilution of PM samples is often done in one or two stages. If only one stage of dilution is required, a Dekati DI-1000 ejector diluter, with air or nitrogen, is commonly used. This style of diluter creates a venturi effect caused by the injected diluting gas that pulls sample air into the main mixing region. The dilution factor is adjusted by the inlet pressure of the diluting air. Some studies use two stages of dilution where the sampling probe is designed in a way that an inert gas (often nitrogen) is supplied to the probe and mixes with the sample flow close to the probe inlet to stop conversion processes caused by probe sampling, as soon as possible. Engine sampling often takes place at distances far enough from the engine exit plane, where PM, such as soot agglomerates, have matured and changes to morphology properties in the sampling line are minimal. However, when collecting soot from open flame lab-scale burners, if the soot is not collected soon enough, high oxidation rates due to excessive surrounding ambient air cause particles to drastically reduce in size and effectively change the morphology of the produced soot [7]. Thus, the design method of an inert gas meeting the sample as soon as it enters the sampling probe is employed much more often in soot sampling of open flame burners.

Two common probe designs for open flame collection are the hole-in-a-tube (HiaT) and straight tube sampling probes. A HiaT design can be seen in Figure 1.1 and uses a pinhole of desired size in a cylindrical tube as the inlet for sample collection. The pinhole is often positioned facing downward, opposing the direction of the emission gas flow. An inert gas, often nitrogen or argon, is supplied to one side of the tube and a negative pressure, downstream from the pinhole, pulls both the inert gas and sample flow through the tube where it is mixed, and the sample is diluted. The flow continues downstream to any respective analysis instruments connected to the system.

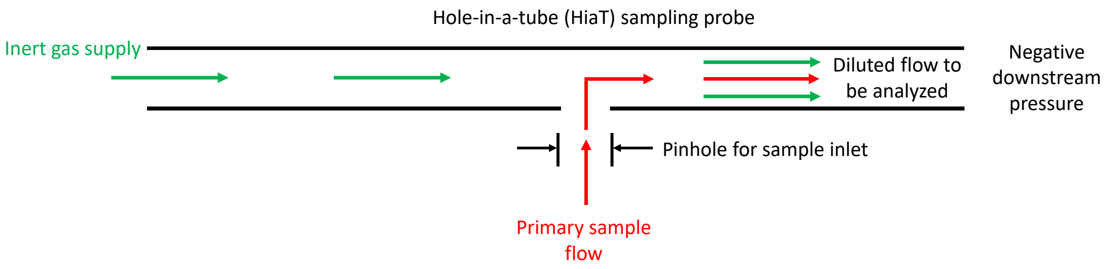

Figure 1.1: HiaT sampling probe design with inert gas dilution, where sample gas flow is sucked into the tube by a negative downstream pressure and meets a horizontal inert gas flow. Mixing between the two flows takes place and the collected sample is diluted.

The straight tube sampling design is similar in that it uses an inert gas to meet the collected sample as it enters the flow. However, instead of using a single tube with a pinhole, the straight tube uses a tube-in-tube design where the inert gas is supplied to the outer tube on one end, and travels toward the open pinhole to meet the sample being drawn in by a negative downstream pressure. In most cases, the collected sample travels a short distance through the probe tip before it mixes with the inert gas and is diluted. The diluted sample continues through the inner tube to be analyzed. A general schematic of this design is shown in Figure 1.2.

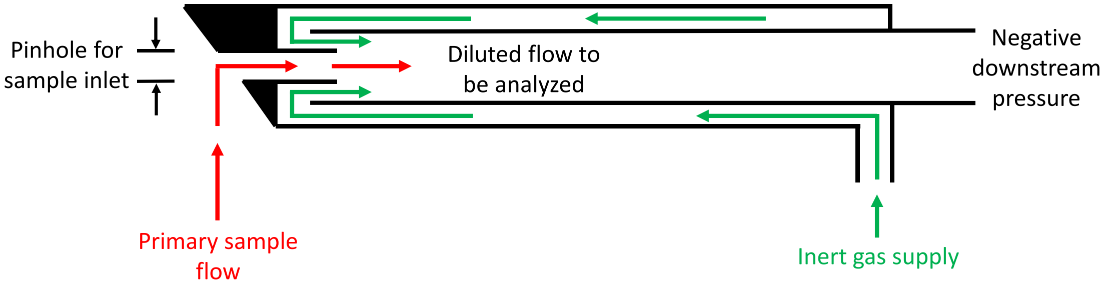

Figure 1.2: Straight tube sampling probe with inert gas dilution, where sample gas flow is sucked into the probe tip by a negative downstream pressure and inert gas is drawn towards the pinhole inlet before being forced around a corner to meet the incoming sample flow. Mixing between the two flows takes place and the collected sample is diluted.

A HiaT sampling design has been the most popular for open flame particle sample collection from both the flame tip and within the flame. Experiments by Zhao et al. in 2003 [26], Commodo et al. in 2015 [27], and Kazemimanesh et al. in 2017 [28], used HiaT sampling probes to collect particles from diffusion or premixed laminar flames and dilute the flow with nitrogen. Zhao et al. improved on an original HiaT design from Kasper et al. [29], using a stainless-steel tube with an outer diameter of 9.53 mm (3/8”) and 0.71 mm (0.028”) wall thickness. After many tests, Zhao et al. found that a pinhole of 0.2 mm diameter provided the best result for maximum dilution which was >10,000. They also incorporated water cooling sleeves around the tube, on either side of the pinhole, to further cool the sample flow and limit chemical reactions in the line.

Commodo et al. [27] used a similar HiaT design, having the same pinhole size of 0.2 mm, but used a slightly larger stainless-steel tube with 10 mm outer diameter, 0.5 mm wall thickness, and no water cooling. This design ensured dilution ratios of ≈3000. Kazemimanesh et al. [28] also did not use water cooling and operated with a stainless-steel tube that was smaller in size with a 3.2 mm outer diameter and wall thickness of 0.52 mm. The pinhole size in this experiment was 0.5 mm but needed to be unclogged by a fine wire periodically through testing. They found that a pinhole size $<$ 0.5 mm clogged too quickly and did not allow enough time for particle measurements. In this experiment, immediate dilution ratios reached up to ≈6000.

Although these examples with HiaT sampling probes provided a range of dilution ratios and successfully measured particle size distributions from open flames, the HiaT design risks a higher flame perturbation, with respect to the flow field and temperature profiles, compared to the straight tube design [30]. Straight tube sampling probes can also be adjusted to meet a range of dilution ratios by changing tube sizes, pinhole inlet diameters, and dilution gas flows. Within these straight tube designs, there is more opportunity to design the probe to minimize flame disturbance, compared to HiaT designs, due to the geometry [30]. Recent straight tube sampling probe designs were used for particle collection from liquid fuel burner exhaust plumes by Heath in 2012 [31], co-flow diffusion flames by Dreyer et al. [30] and Tan et al. [32], and flame spray pyrolysis burners by Goudeli, Gröhn, and Pratsinis [33], Trivanovic, Kelesidis, and Pratsinis [34], and Kholghy and DeRosa [35].

In 2012, Christopher Heath of the NASA Glenn Research Center designed a stainless-steel straight tube probe for isokinetic sampling of submicron particle measurements at high altitudes [31] using Numerical Propulsion System Simulation code and computational fluid mechanics. Combustion was modelled with a low pressure (1-2 atm) burner capable of burning jet fuel. The straight tube probe was inserted into the altitude emission chamber, positioned in different axial and radial distances from the exhaust injection site, and pointed downward, directly into the rising exhaust flow. Dilution gas was supplied to the straight tube, resulting in a dilution ratio of 26. The internal sampling tube, carrying nitrogen diluted sample flow, had a 6.35 mm (1/4") outer diameter with 0.89 mm (0.035") wall thickness and the outer tube, carrying the nitrogen gas, had a 9.53 mm (0.375") outer diameter with a 0.89 mm (0.035") wall thickness. The tip was custom made and interfaced with the tube sizes. The sample flow entered the tip through a 1.04 mm (0.041") hole and travelled 21.7 mm (0.854") through the probe tip before it met the nitrogen dilution gas and expanded into the 6.35 mm (1/4") tube. As the dilution gas met the sample flow, particle concentration decreased rapidly. However, computational fluid dynamics results on this design predicted particle losses near 50% for all particle sizes during the 21.7 mm (0.854") travel distance before the sample met nitrogen. It was thought to be caused by diffusion losses due to increased velocity in the inlet region of the probe tip [31].

The straight tube sampler in experiments by Dreyer et al. [30] and Tan et al. [32], in 2018 and 2021, was composed of a combination of stainless-steel and quartz components. A quartz tube was used as the outermost tube to house the nitrogen dilution gas. This way, it could be custom formed to incorporate the inlet pinhole in one piece. The quartz tube had an outer diameter of 12 mm, wall thickness of 4 mm, and an inlet pinhole 0.4 mm in diameter. The geometry of the tip was developed to minimize flame disturbance and residence time of the sample to reduce particle losses due to diffusion [30]. The nitrogen diluted sample then travelled through a stainless-steel tube with a 6 mm outer diameter and a 1.5 mm wall thickness. Dilution ratios in these experiments were 170-250 and 1200, respectively.

Goudeli, Gröhn, and Pratsinis [33], Trivanovic, Kelesidis, and Pratsinis [34], and Kholghy and DeRosa [35] used a lab scale-flame spray reactor (LS-FSR) designed by Wegner Consulting to synthesize ZrO_2 [33] and soot [34, 35] particles. These three experiments used straight tube sampling probes to collect and dilute the nanoparticles before analysis. The straight tube sampler in Goudeli, Gröhn, and Pratsinis', and Trivanovic, Kelesidis, and Pratsinis' experiment had a 2.5 mm pinhole inlet where the sample flow traveled for 15 mm before expanding to a 5 mm inner diameter tube when the nitrogen dilution mixed with the sample. Dilution ratios by the straight tube were not specifically defined in Goudeli, Gröhn, and Pratsinis' experiment, but Trivanovic, Kelesidis, and Pratsinis supplied a constant 10 L/min of nitrogen dilution gas to the probe, while collecting 12 L/min of soot aerosol sample flow.

Table 1.3: Sampling probe literature review summary table for lab-scale burners.

Authors	Sampling Probe	Pinhole Size	Dilution Ratio	Emission Source	Measurements
Zhao et al. [26]	HiaT with water-cooling	0.2 mm	>10,000	Laminar premixed ethylene-oxygen-argon flame from porous plug burner.	Soot mobility size distributions
Commodo et al. [27]	HiaT	0.2 mm	≈3000	Laminar premixed ethylene-air flame from	Soot mobility size distributions, primary

				McKenna burner.	particle distributions, at different phases of the flame
Kazemimanesh et al. [28]	HiaT	0.5 mm	≈6000	Laminar methane jet diffusion flame from co-flow burner.	Soot mobility size distributions
Heath [31]	Straight tube	1.041 mm (0.041”)	26	Liquid fuel, low pressure burner	CFD modelling
Dreyer et al. [30] Tan et al. [32]	Straight tube	0.4 mm	170-250 [30] 1200 [32]	Laminar n-heptane/toluene co-flow diffusion flame from Yale burner.	Soot mobility size distributions at different phases of the flame
Goudeli, Gröhn, and Pratsinis [33] Trivanovic, Kelesidis, and Pratsinis [34]	Straight tube	2.5 mm	N/A [33] 12 L/min sample, 10 L/min N_2 dilution [34]	Turbulent diffusion zirconium-xylene precursor solution flame from LS-FSR [33]. Turbulent diffusion Jet A1-oxygen-air flame from LS-FSR [34].	ZrO_2 mobility size distributions, primary particle diameter [33]. Soot mobility size distributions, composition, primary particle size [34].
Kholghy and DeRosa [35]	Straight tube with water-cooling	2.5 mm	N/A	Turbulent diffusion Jet A1-oxygen-air flame from LS-FSR	Soot mobility size distributions, primary particle distributions, composition, optical properties.

1.3 Soot Generating Burners

A recent review of jet engine soot morphological properties by Saffaripour et al. [36] identified that geometric mean mobility diameters ($\overline{d_m}$) generally measured < 70 nm with geometric standard deviations (σ_g) ranging from 1.5-1.8. All particle size distributions showed lognormal distributions [36]. The composition, referring to elemental to total carbon ratio (EC/TC), of soot produced by jet engines operating on conventional jet fuels like Jet A1, remains > 0.8 at medium and high thrust levels [37]. Due to this, optical diagnostic tools that rely on the composition of soot, for the measurement of its refractive index, are often calibrated to measure particles with EC/TC > 0.8 [37]. Lab-scale burners like the mini-CAST [37], the inverted burners [38, 39], and the McKenna burner [40], have been used to burn gaseous fuels in laminar premixed and diffusion flames to synthesize soot particles with morphological and composition properties like those found in jet engine soot emissions. However, these burners fail to meet both particle size and composition of jet engine-like soot, in the desired range [37], and cannot burn liquid fuels. Flame spray pyrolysis has recently been used to generate soot particles using liquid fuels, including Jet A1, and has shown capability to produce soot agglomerates with $\overline{d_m} < 70$ nm and EC/TC > 0.8 [41, 42].

A study by Durdina et al. [37] used two mini-CAST burners (models 5201C and 6203C) to generate soot particles of different sizes and compositions from a co-flow diffusion propane flame. The global fuel-air equivalence ratio was altered in the range of 0.49-1.01 for different flame conditions. Elemental carbon contents remained high, with all flame conditions producing EC/TC > 0.8, but only two conditions at low equivalence ratios produced particles with $\overline{d_m} < 70$ nm. However, they found that adjusting the global fuel-air equivalence ratio produced unpredictable $\overline{d_m}$ and EC/TC results when working with different models of mini-CAST. They also found that mini-CAST soot EC content reduces with decreasing $\overline{d_m}$, that generating soot with EC/TC > 0.8 and $\overline{d_m} < 50$ nm was not feasible, and that other sources should be investigated.

In 2019, Kazemimanesh et al. [38] experimented with a novel inverted co-flow ethylene-air diffusion flame burner that had interchangeable fuel and co-flow air tube sizes. The goal was to investigate the effect of tube geometry on flame stability and soot particle emissions. After initial testing, it was found that the largest tube size design, which had identical geometry to the Argonaut Scientific Corporation inverted burner (model MISG-1), worked best for soot particle production. Global equivalence ratios were adjusted from 0.124 to 0.186 to generate various number concentrations and particle sizes. For these conditions, EC/TC ratio was very high (0.88-0.98), but mode mobility diameter did not go below 89 nm, and most conditions were around 230 nm. It was concluded that this burner could be used as a stable source of soot particles in applications where high EC content is desired. However, this design did not show the capability to produce soot with high EC/TC and $\overline{d_m} < 70$ nm.

Experiments with the novel inverted burner were continued by Moallemi et al. [39] using a co-flow propane-air diffusion flame. The goals of this work were like that of Kazemimanesh et al. [38]; to find optimal burner operating conditions and assess stability and repeatability. Again, global equivalence ratios were varied to produce a range of soot properties, including morphology, composition, and optical properties. Elemental carbon contents in this study remained high with a mean value of ∼0.94 for all conditions, and mode mobility diameters ranged from ∼100-200 nm.

A study by Ghazi et al. [40] experimented both with a McKenna burner operating with premixed ethylene-air, and an inverted-flame burner operating with methane and air in co-flow. Median mobility diameters ranged from 93-148 nm and 62-163 nm, respectively, with only the leanest inverted-flame condition producing median mobility diameters < 70 nm. Organic content and volatile material on inverted burner soot was deemed minimal and immeasurable; however, McKenna burner soot contained substantial, flame condition dependent, volatile material.

Recently in 2021, Kholghy and DeRosa introduced flame spray pyrolysis (FSP) as a technique to synthesize jet engine-like soot using conventional Jet A1 liquid fuel [35]. The burner used was an LS-FSR by Wegner Consulting Group, and the flame was left open to surrounding air within a large fume hood. The turbulent diffusion flame produced $\overline{d_m}$ and $\overline{d_p}$ in the range of 13-91 nm and 13-22 nm while maintaining EC/TC > 0.8. The range of size distributions were created by adjusting common FSP parameters such as fuel and oxidizer flow rates. They operated with fuel and oxygen flow rates between 9-12 mL/min and 1-1.75 L/min, respectively. Trivanovic, Kelesidis, and Pratsinis used the same burner with liquid Jet A1 but enclosed the flame with quartz tubing (60 cm in height) and provided nitrogen gas half-way up the quartz tube enclosure to reduce particle oxidation before sample collection [34]. This allowed synthesis of soot agglomerates with similar size to

Kholghy and DeRosa’s work ($15 < \overline{d_m} < 153$ nm, $\overline{d_p} \cong 14$ nm) but with a reduced fuel flow rate of 4.5 mL/min and oxygen flow rate of 1.5-3 L/min.

Table 1.4: Lab-scale burner literature review summary table.

Authors	Burner used	Flame	EC/TC ratio	Particle Diameter
Durdina et al. [37]	Mini-CAST	Co-flow propane-air diffusion	0.81-0.93	55-161 nm (Geometric mean mobility diameter)
Kazemimanesh et al. [38]	Novel miniature inverted-flame burner	Inverted co-flow diffusion ethylene-air	0.88-0.98	89 nm, 230 nm (Mode mobility diameter)
Moallemi et al. [39]		Inverted co-flow diffusion propane-air	~0.94	100-200 nm (Mode mobility diameter)
Ghazi et al. [40]	McKenna burner, inverted burner	Premixed ethylene-air, inverted co-flow diffusion methane-air	N/A	93-148 nm 62-163 nm (Median mobility diameter)
Kholghy and DeRosa [35], Trivanovic, Kelesidis, and Pratsinis [34]	Flame Spray Pyrolysis burner (LS-FSR)	Turbulent diffusion flame with liquid Jet A1, oxygen, and sheath air flow	≥ 0.89, 0.81-0.83	13-91 nm, 15-153 nm (Geometric mean mobility diameter)

1.4 Motivation

This study seeks the use of FSP as a bench-top rapid screening device to compare agglomerate size distribution, morphology, composition, and optical properties of soot particles generated from three different standardized liquid jet fuel samples with certified POSF numbers. Jet fuel soot samples collected from field tests are classified by their size, having average d_m and d_p less than 70 [41] and 20 nm [42], respectively, elemental to total carbon ratios, EC/TC, greater than 0.8 [42], and MAC of ~7.5 and ~5.2 m^2/g at 532 and

870 nm, respectively [43]. Current bench-top scale reactors such as Mini-CAST [44], the Argonaut Inverted Burner [45], and the McKenna burner [46] attempt to synthesize jet engine-like soot but fail to meet the EC/TC and d_m thresholds mentioned above. The soot produced by the mini-CAST can reach EC/TC > 0.8 but only when $\approx d_m > 60$ nm [44]. The Argonaut Inverted Burner met EC/TC values of 0.88 but failed to produce soot particles with $d_m < 90$ nm [45]. The McKenna burner produced smaller particles ($d_m <$ 30 nm) within the jet engine thresholds but did not exceed EC/TC = 0.8 [46]. These burners operate on gaseous fuels such as propane or ethylene mixtures and do not have the capability to burn liquid jet fuels. However, there are emerging tests that use vaporized liquid fuel burnt in a co-flow diffusion flame to measure soot volume fractions and smoke point as a measure of the sooting tendency of each fuel [47].

Liquid SAFs are continuously evolving as certification standards, emissions restrictions, and compatibility with current rigs and components continue to advance. Fuel pre-screening processes get expensive when large volumes of fuel, increased numbers of personnel, and full-sized jet engines are required for testing. Current pre-screening standards estimate soot emissions based on fuel composition and chemical stoichiometry [10] but rarely synthesize soot with combustion. Previous work by Kholghy & DeRosa [35] has shown that flame spray pyrolysis (FSP) can synthesize jet fuel soot, maintaining the size, composition, and optical properties within the same threshold as soot collected from full-sized engine field tests [28]. Based on the literature discussed in Section 1.3, there are not many lab-scale reactors capable of generating jet engine-like soot from liquid fuels. The contribution of this research is to provide a lab-scale liquid fuel reactor and sampling assembly capable of generating soot similar to that emitted from full-size turbofan engines. Knowing that FSP can produce soot from liquid Jet A1 fuel comparable to engine test samples, this work aims to use FSP to estimate properties of soot formed from developing SAFs and compare them with reference Jet A1.

1.5 Flame Spray Pyrolysis

FSP was originally designed for scalable synthesis of inorganic nanoparticles [29]. FSP provides a versatile approach to synthesize nanoparticles with excellent control of oxidation states, band gap, morphology and surface area in a way that is both scalable and affordable [50]. As such, FSP is usually operated under very fuel lean conditions to prevent soot which is often considered as a contaminant. However, FSP has also been used for the synthesis of carbon-coated [51] or -supported [52] nanoparticles, which demonstrates the potential of this technique for synthesis of organic nanoparticles such as soot. Recently, Kholghy & DeRosa [35] and Trivanovic, Kelesidis, and Pratsinis [34] used FSP to generate soot particles from liquid Jet A1 fuel in both open [35] and enclosed [34] flames, where thresholds for size, composition, and optical properties of jet engine soot were met.

FSP uses a liquid fuel to generate spray combustion turbulent flames. Liquid fuel is supplied through a central capillary in the burner where it is atomized by surrounding dispersion oxygen supplied with a choked flow at a pressure drop of 2 bar and ignited by the premixed methane pilot flame, seen in Figure 1.1. Open flames, like the ones tested in this study, entrain surrounding air, which affects soot oxidation and is difficult to quantify

[52]. To minimize this, a quartz tube was placed on top of the FSP burner, surrounding the base of the flame.

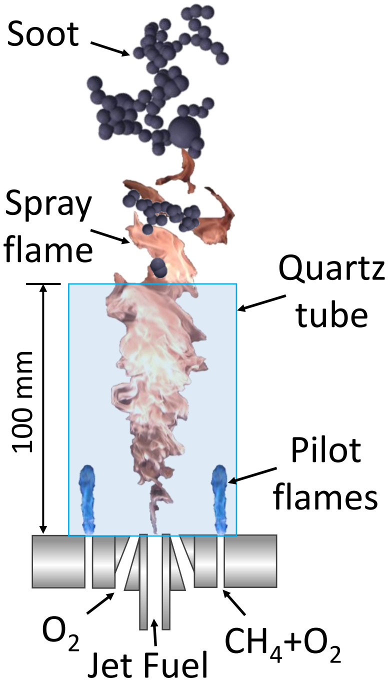

Figure 1.3: An illustration of the FSP burner and the resulting turbulent flame used for soot formation. Liquid jet fuel is supplied through the central capillary and oxidized with a surrounding ring of dispersion oxygen. Atomized jet fuel is then ignited by the surrounding premixed, methane-oxygen pilot flame. A quartz tube (ID: 42mm, OD: 46mm, height: 100mm) is placed on the surface of the burner to reduce entrained air caused by the nature of a turbulent diffusion flame.

1.6 Outline of Thesis

The following chapters of this thesis detail the planning, design, and experimental steps of building a FSP assembly for synthesis of soot from liquid jet fuels and sampling it for analysis and characterization. Chapter 2: Methodology covers fuel and flame conditions, soot sampling techniques, and the tools used for analysis. The particle size distribution, morphology, and composition results from samples are analyzed and discussed in Chapter 3: Results. Chapter 4: Conclusions and Outlook concludes the thesis and discusses further work for this project.

Chapter 2: Methodology

2.1 Flame Spray Pyrolysis Burner

The FSP burner used in this study was designed and built by Wegner Consulting Group. It is a refined design from the original FSP burner used by Mädler et al. in 2002 to synthesize nanostructured particles and systematically control the specific surface area of the generated particles by adjusting oxidant and fuel flow rates [48]. This specific burner was chosen for this study because of its capability to generate soot with the size, composition, and optical properties of aviation like soot, while other common lab-scale soot generators failed to meet these thresholds as discussed in Section 1.3.

A schematic (not to scale) of the FSP is shown in Figure 2.1 to illustrate the geometry and location of flow paths for fuel, oxygen (the atomizing oxidizer), the pilot flame, and sheath gas flow. The sheath gas flow (green) is shown as eight individual points in this schematic, but the physical design for the burner used in this work is a porous plate and can be better visualized in Figure 2.2. The sheath flow function was not used for the experiments and data outlined in this work.

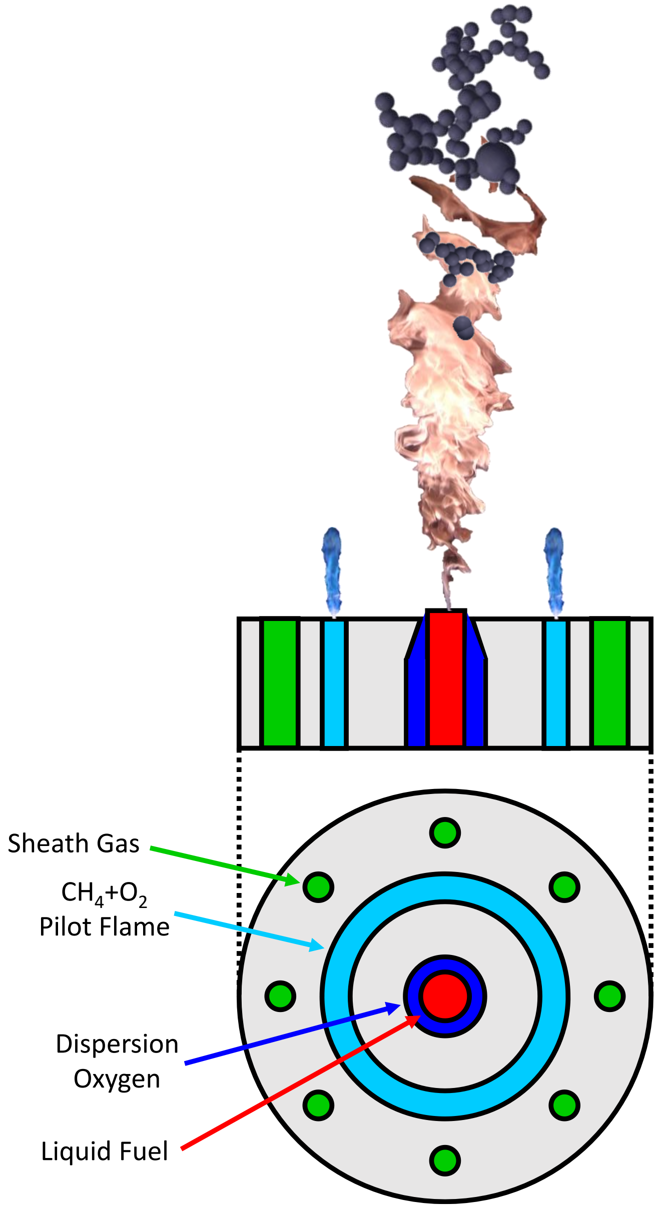

Figure 2.1: Side section and top view schematic of an FSP burner with liquid fuel supply (red), dispersion (atomizing) oxygen (blue), methane-oxygen pilot flame (turquoise), and sheath gas flow (green).

Detailed top, bottom, and side views can be seen in Figure 2.2 with bubble labels coinciding with the parts list in Table 2.1. Liquid fuel is supplied through a capillary (E), via a liquid pump (Teledyne 1000D), where it is atomized at the surface of the central body (C) by dispersion oxygen exiting an annulus (ID = 0.71 mm, OD = 0.95 mm) at 2 bar back pressure, gauged upstream from the nozzle, to ensure choked flow at nozzle exit. Atomization and evaporation of the fuel droplets in the spray is much faster when using oxygen as opposed to compressed air because pure oxygen accelerates the fuel combustion process [48]. The atomized spray is then ignited by a premixed methane-oxygen support flame, which continues to burn during operation to prevent flame liftoff, with flow rates of 1.25 L/min and 2.5 L/min, respectively, with an equivalence ratio of 1. Cooling water for the reactor body flow in and out of A1, while the cooling water for the capillary is supplied through D1 and exits out of C3.

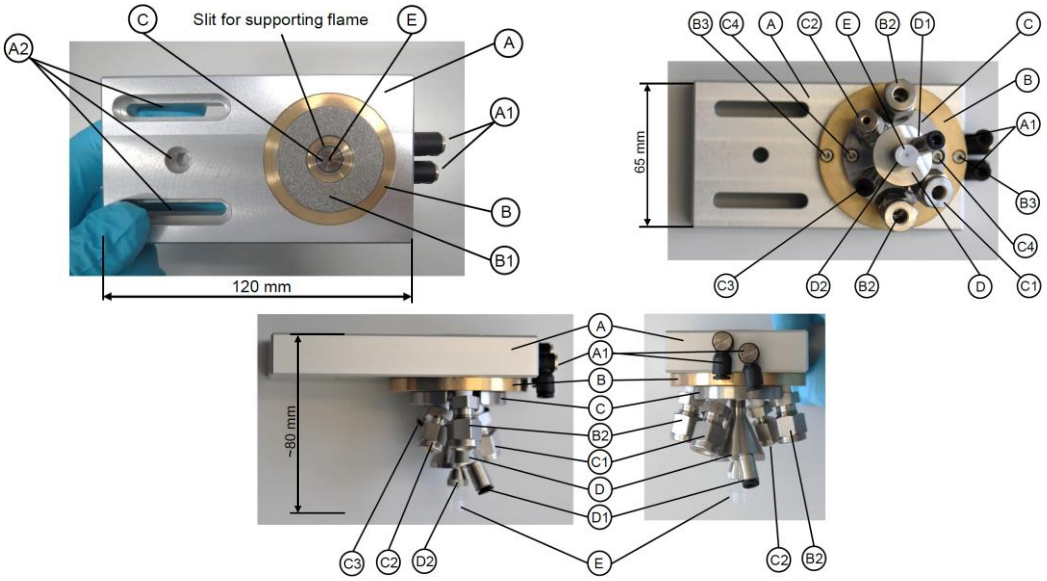

Figure 2.2: Top, bottom, and side views of the lab scale flame spray reactor (LS-FSR) designed by Wegner Consulting Group with water cooling, dispersion oxygen supply, and a sheath flow option for the flame. Table 2.1 identifies the labeled parts for the LS-FSR burner [53].

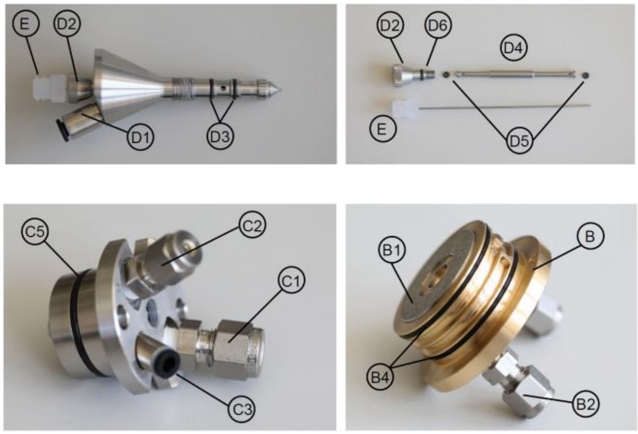

Figure 2.3: Central insert and liquid fuel supply capillary (top) and the central body with sheath gas homogenizer (bottom). Table 2.1 identifies labeled parts for the central inserts, capillary, and homogenizer [53].

In the top two quadrants of Figure 2.3, the liquid fuel supply capillary is identified by bubble E. This is the stock capillary that comes with the purchase of an LS-FSR burner and simply slides into D2 and holds position with an interference fit. Tolerances and fits are very tight surrounding the capillary and thus require precise positioning to ensure proper co-flow of the liquid fuel and surrounding dispersion oxygen. It was noticed early on that any small forces or moments on the capillary caused disruptions in the co-flow, resulting in incomplete atomization and asymmetric spray flames. This was a major source of error when attempting day-to-day repeatability in size distributions. To reduce this error, a threaded capillary was ordered that threaded into D2 instead of using an interference fit. This threaded capillary can be seen in Figure 2.4, with the red arrow identifying the modified threading.

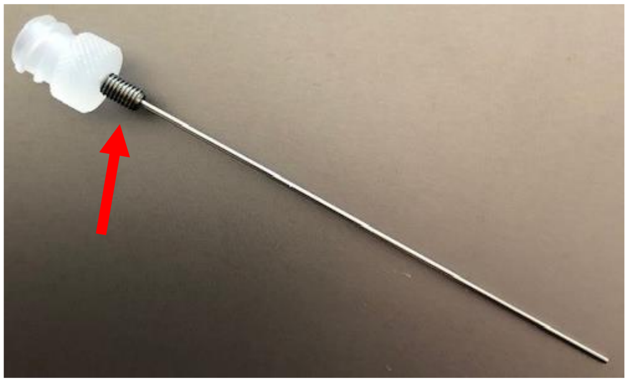

Figure 2.4: LS-FSR fuel supply capillary with a threaded modification to improve precise positioning and consistency in co-flow of the liquid fuel and surround dispersion oxygen.

Table 2.1: List of parts of the lab-scale flame spray reactor (LS-FSR) [53].

Bubble Label	Part Name
A	Rectangular burner holder
A1	Connectors for reactor cooling water, Legris 4mm
A2	Mounting holes for M6 screws
B	Sheath gas body
B1	Sheath gas homogenizer
B2	Connectors for sheath gas, Swagelock® ¼”
B3	Screws fixing reactor to holder, M3x12mm
B4	O-rings of sheath gas body
C	Central body
C1	Connector for dispersion gas, Swagelock® ¼”
C2	Connector for supporting flame gases, Swagelock® 1/8”
C3	Capillary cooling water outlet, Legris 4mm
C4	Screws connecting central body and sheath gas body, M3x12mm
C5	Central body O-ring
D	Central insert
D1	Capillary cooling water inlet, Legris 4mm
D2	Capillary locking nut
D3	Upper and lower central insert O-ring
D4	Spacer
D5	Capillary O-rings
D6	Locking nut O-ring
E	Liquid feed capillary with Luer Lock connector

2.2 Fuels and Flame Conditions

For this study, three different liquid aviation fuels were used: Jet A1 (POSF10325), Gevo ATJ (POSF11498), and a custom fuel that will be referred to as “C10” (POSF12345) due to its 74% composition of C10 iso-paraffins. As of 2021, Jet A1 is the only fuel cleared to be used in commercial aircraft [10], but the ATJ and C10 fuels are currently being used by the National Jet Fuels Combustion Program (NJFCP) as potential SAFs for future commercial use [54]. For this study, Jet A1 was chosen as a benchmark fuel, the ATJ was chosen as it is an approved biojet fuel for mixture with Jet A1 and operated on non-commercial flights, and the C10 was chosen because of its high aromatic content. These three fuels were recently compared in a study by the National Research Council of Canada (NRC) in 2017 which operated a 1.15kN-thrust Microturbo TRS-18 turbojet engine housed inside an altitude chamber [54]. These fuels were available for this study and specific batch properties were provided. Further fuel details and properties, including the fuel POSF number (number given by the US Air Force Research Laboratory to identify specific batches of fuel), are outlined in Table 2.3 and detailed chemical compositions are displayed in the supplementary material, Section A.3.

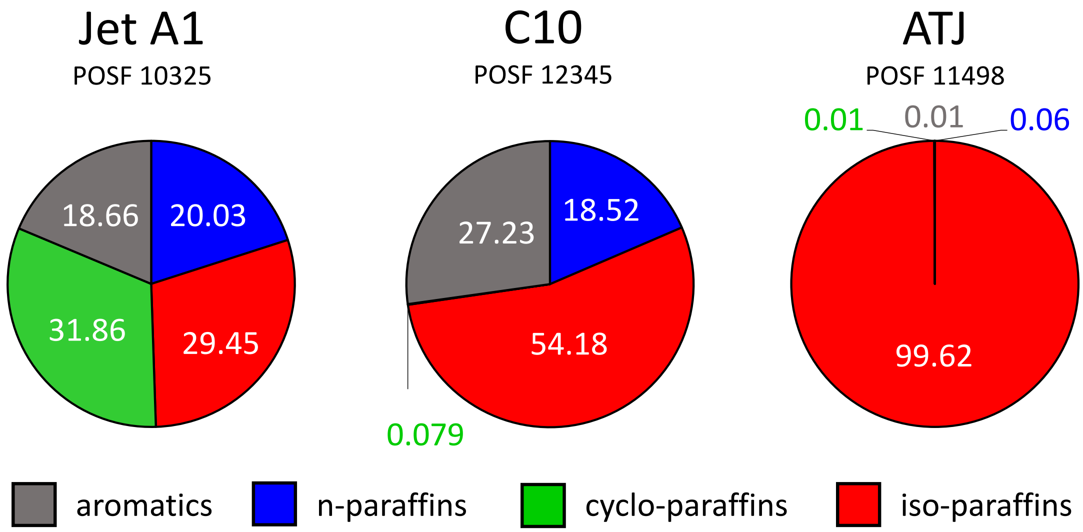

Figure 2.5: Alkane and aromatic mass percent composition of the three test fuels [54].

Figure 2.5 identifies the alkane and aromatic mass percentages of the three test fuels. The alkanes are subdivided into n-paraffins, cyclo-paraffins, and iso-paraffins. These four categories are a good envelope for estimating sooting tendencies regarding aviation fuel combustion processes in jet engines [22]. Most studies involving newly developed SAFs and/or conventional and SAF mixtures will identify these properties of their testing fuel at minimum, which makes this figure beneficial for comparison with literature. Since the sooting tendencies (including size and composition) for Jet A1 have been highly tested and are considered known, based on previous literature (discussed earlier in Section 1.2), predictions can be made for the SAF fuels. Typically, higher aromatic content and cyclo-paraffins results in increased sooting tendencies and larger particles [22]. The C10 fuel has a high mass percent of aromatics (27%) but little to no cyclo-paraffins compared to Jet A1. This could result in similar sooting tendencies in regards for size, shape, or concentration. The ATJ fuel has little to know aromatics or cyclo-paraffins and is almost completely comprised of iso-paraffins. This is expected to greatly reduce sooting tendencies compared to Jet A1, including smaller sized agglomerates, smaller primary particles, and reduced number concentrations for similar combustion conditions.

Table 2.2: Test fuel designation and properties [56]

Fuel Name (POSF#)	Average Formula	Viscosity [mm^2/s] at -20°C	Density [g/cm^3]	MW [g/mol]
Jet A1 (10325)	$C_{11.4}H_{21.7}$	4.5	0.803	158.6
C10 (12345)	$C_{9.7}H_{18.7}$	1.9*	0.769	135.4
ATJ (11498)	$C_{12.5}H_{27.1}$	4.9	0.760	178.0

*C10 kinematic viscosity at room temperature was unknown, so it is important to note that the Re number for C10 flames could change by up to a factor of ≈2 from the Jet A1 and ATJ flames because the viscosity of Jet A1 has been used to calculate Re of C10 flames.

The fuel and dispersion oxygen flow rates were adjusted to produce a variety of flame conditions. Three different flame conditions were chosen for testing and comparison that offered a range of Reynolds numbers and burner equivalence ratios. The flame conditions are specified in Table 2.3 by a ratio, the first number being the flow rate of fuel in mL/min and the second number being the flow rate of dispersion oxygen in L/min. Due to the nature of an open flame condition, true global equivalence ratios of the flames were difficult to quantify because of an immeasurable volume of entrained air. The flow rates and their associated Reynolds numbers and burner equivalence ratios are shown in Table 2.3. Respective Reynolds number and burner equivalence ratio calculations are outlined in Sections 2.2.1 and 2.2.2.

Table 2.3: Reynolds numbers and burner equivalence ratios for flame conditions.

Flame Condition (fuel [mL/min]/oxygen [L/min])	Reynolds Number (gas)	Reynolds Number (liquid)	Effective Reynolds Number*	Fuel	Burner Equivalence Ratio**
10/3.00	2800	180	9100	Jet A1	7.0
				C10	6.7
				ATJ	6.7
12/2.50	2400	210	7600	Jet A1	10.2
				C10	9.8
				ATJ	9.9
12/2.00	1900		6100	Jet A1	13.1
				C10	12.6
				ATJ	12.7

*Jet A1 kinematic viscosity and density values at 273K used for all Reynolds number calculations
**Burner equivalence ratios do not account for entrained air and are calculated using gas and liquid flow rates supplied directly to the burner.

2.2.1 Reynolds Number Calculation

The design of this reactor imitates a coaxial jet, with liquid flow at the center and a surrounding dispersion oxygen gas flow. The displayed Reynolds numbers in Table 2.3 are the effective Reynolds numbers, and do not consider flow effects from the supporting flame or varying volumes of entrained air. The effective Reynolds number for a coaxial jet is a combination of the Reynolds number for both the liquid, Re_l, and gas, Re_g, flows (equation 1) [57].

$$Re_l = \frac{U_l D_l}{v_l}, Re_g = \frac{U_g D_g}{v_g} \tag{1}$$

where U, D, v represent the velocity of the liquid or gas, the diameters of the liquid or gas streams, and the kinematic viscosity of the liquid or gas, respectively. The effective Reynolds number for both flows, Re_{eff}, is then calculated with equation (2) [58]

$$Re_{eff} = \left(\frac{U_g D_g}{v_g}\right)[(1 - \frac{D_l^2}{D_g^2}) + \frac{D_l^2}{M D_g^2}] \tag{2}$$

where M is the momentum flux ratio per unit volume.

$$M = \frac{\rho_g U_g^2}{\rho_l U_l^2} \tag{3}$$

2.2.2 Burner Equivalence Ratio

The FSP burner in this study uses a coaxial flow design with liquid flow through the center capillary, surrounded by a ring of dispersion oxygen flow, and an outermost ring of a premixed methane-oxygen pilot flame. The equivalence ratios calculated for the various flame conditions in this study will be referred to as a burner equivalence ratio, as it will incorporate all gas and liquid flows provided to the burner. However, it is important to note that this burner equivalence ratio does not include the amount of entrained air caused by the turbulent nature of the flame.

Calculations were done at standard temperature and pressure, and used average formulas, densities, and molecular weights (MW) found in Table 2.3. For the premixed pilot flame, a stoichiometric combustion of methane, CH_4, requires twice the molar flow of oxygen, O_2, to fully combust a single mole of CH_4, seen in Equation (4).

Methane: $$CH_4 + 2\ O_2 \rightarrow\ CO_2 + 2\ H_2O \tag{4}$$

This oxygen flow must be subtracted from the total O_2 available for combustion with jet fuel, resulting in the net molar flow of O_2 [34]. The required O_2 to combust each jet fuel under stoichiometric conditions was calculated and is shown in the equations below.

Jet A1: $$C_{11.4}H_{21.7} + 16.825\ O_2 \rightarrow 11.4\ CO_2 + 10.85\ H_2O \tag{5}$$

C10: $$C_{9.7}H_{18.7} + 14.375\ O_2 \rightarrow 9.7\ CO_2 + 9.35\ H_2O \tag{6}$$

ATJ: $$C_{12.5}H_{27.1} + 19.275\ O_2 \rightarrow 12.5\ CO_2 + 13.55\ H_2O \tag{7}$$

The burner equivalence ratio (Φ) is calculated with Equation (8), where B is the molar ratio of O_2/jet fuel required to achieve stoichiometric conditions [34].

$$\Phi = \frac{B}{\frac{Net\ molar\ flow\ of\ O_2}{Molar\ flow\ of\ jet\ fuel}} \tag{8}$$

The molar flow of O_2 is calculated by:

$$\frac{flowrate\ O_2\ [\mathrm{L/min}]}{60\ \mathrm{s/min} \cdot 22.4\ \mathrm{L/mol}} = flowrate\ O_2\ [\mathrm{mol/s}] \tag{9}$$

where $22.4\ \mathrm{L/mol}$ is the density of gas at standard temperature and pressure. The molar flow of jet fuel is calculated by:

$$\frac{flowrate\ fuel\ [\mathrm{mL/min}]}{60\ \mathrm{s/min}} \cdot \frac{\rho_{fuel}\ [\mathrm{kg/m^3}]}{MW\ [\mathrm{g/mol}]} \cdot \frac{1}{1000} = flowrate\ fuel\ [\mathrm{mol/s}] \tag{10}$$

Table 2.4: Molar oxygen/fuel ratios required to achieve stoichiometric conditions.

Fuel	***B***
Jet A1	17
C10	14
ATJ	19

2.3 Sample Collection

The sampling probe is located above the burner at a height-above-burner (HAB) of 23 cm. This height allows sampling to take place from above the flame, the flame tip, and within the flame depending on which flame condition is tested. For uniformity, the HAB remained constant for all flame conditions, although the assembly was designed for easy adjustment of sampling HAB. Sample soot size properties are very sensitive to changes in sampling HAB due to oxidation rates. The farther away the sampling probe inlet is from the flame tip, the more time the particles have to oxidize by surrounding air, reducing overall particle concentration and particle diameters. For this experiment, positions that sampled from above the flame, at the flame tip, and from within the flame, were tested by keeping the sampling HAB constant but changing the flame condition. One of the goals of this work was to compare soot concentration and size distribution between fuels and identical flame and sampling conditions, so keeping the sampling HAB constant for identical flame conditions but different fuels was imperative. For the 10/3.00 flame condition, the probe sampled from just above the flame tip. For the 12/2.50 flame condition the probe was generally just below the flame tip, and for the 12/2.00 flame condition the probe sampled about two thirds up the flame.

The probe is a straight-tube design with an additional water-cooling sleeve as the most external tube. The water-cooling sleeve was desirable for this experiment because recent literature using similar designs for soot collection found that cooling the hot sample gas soon after extracting from the flame helped to reduce further chemical reactions of the collected aerosol within the sampling line, causing aerosol properties to drift further from the produced aerosol at the point of interest. This design is modified from an original design by Tan et al. [32] and improved from a proof of concept by Kholghy and DeRosa [35]. Immediate nitrogen dilution is used to quench reactions with surrounding air, reducing particle oxidation rates, and preserving soot particle properties as they are from the flame. Nitrogen was chosen as the dilution gas because of its inert gas properties and cost effectiveness.

Shown in Figure 2.6, cooling water is supplied into the left 1” Swagelock tee and travels through the largest diameter tube, exiting out the 1” tee on the right, acting as a cooling sleeve for the hot sample. It is completely closed off from all gas and sample flows. The primary nitrogen dilution gas is supplied through the ½” tee that is sealed on the right-most side, forcing the gas to flow left. An angled cap was welded onto the end of the ½” tube carrying the nitrogen to help direct the gas around the corner and mix with the entering sample (see Figure 2.6, detail A). A 3 mm diameter hole was drilled through the cap where the sample travels ~10 mm before mixing with the dilution nitrogen. The 3 mm inlet hole size was chosen to ensure no clogging due to extended testing periods. Previous work, as discussed in Section 1.2, found that inlet holes ≤ 2 mm in diameter clog when sampling aviation-like soot. A negative pressure downstream generated by a vacuum pump and Dekati diluter pulls the cooled and diluted sample from the flame, through the innermost ¼” tube, to the appropriate devices for analysis. Tube diameter sizes were roughly based off previous literature of successful straight-tube sampling designs discussed in Section 1.2 but adjusted to fit standard and readily available tube sizes if needed.

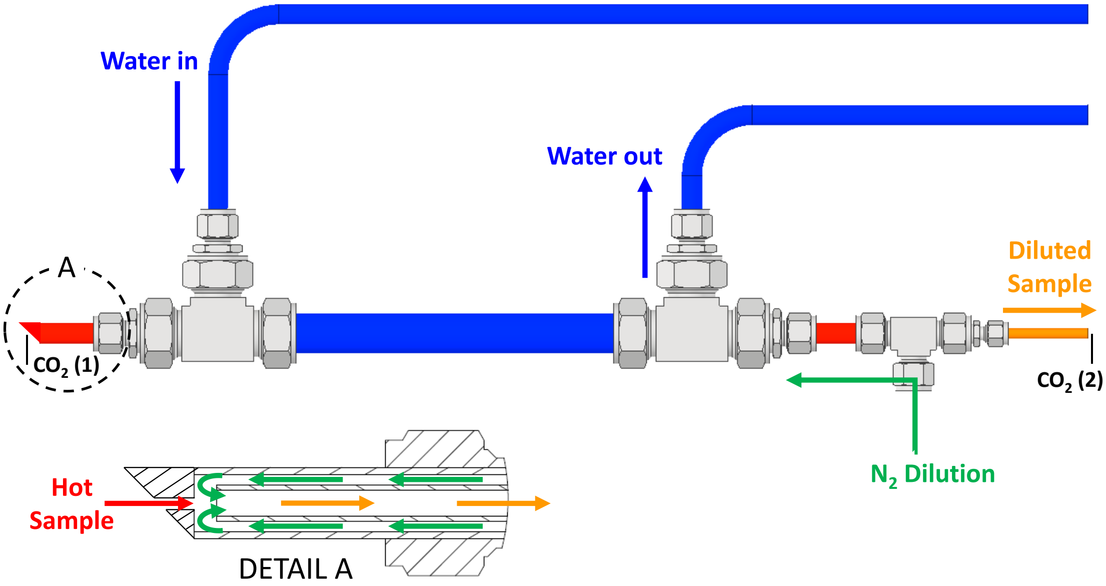

Figure 2.6: Sampling probe with a three-tube design incorporating a 1” water-cooling sleeve tube and a ½” nitrogen gas supply to dilute the collected sample at the probe inlet (A). The hot sample meets the nitrogen and is diluted (see detail A), and travels from left to right through the innermost ¼” tube due to a vacuum pressure downstream. Points CO_2 (1) and CO_2 (2) are the locations of CO_2 concentration measurement to characterize the dilution ratio (DR) of the sampling probe.

The primary dilution by nitrogen was adjusted by changing the supply flowrate with a mass flow controller (Brooks SLA5851, 0-150 SLPM). To identify the dilution ratio created by nitrogen joining the sample at the probe inlet, cold tests (no active flame) were completed, and all flowrates as well as CO_2 concentrations at point 1 and 2 were measured while varying the nitrogen flow rates. Two CO_2 analyzers (LI-COR LI-850) were used to measure active CO_2 concentrations at points CO_2 (1) and CO_2 (2) as shown in Figure 2.6. A Sensidyne Gilibrator-2 was connected to the probe inlet to measure the suction flow rate of the sample. The sample flow passes through the Gilibrator-2 wet calibration cell where bubble films are generated by the push of a button, using a liquid bubble solution. An infrared sensor reads the bubble flow rate and displays it on the digital controller [59]. Ten bubble flows were measured and averaged to confirm each changing inlet flow. A mass flow controller was connected to the right end of the probe to measure the flowrate of the exiting nitrogen diluted sample. Panel (a) of Figure 2.7 shows the varying concentrations of CO_2 in parts-per-million (ppm), measured at CO_2 (2) in Figure 2.6, as the nitrogen dilution flowrate increases from 5 L/min to 30 L/min, compared to the ambient CO_2 content measured at CO_2 (1) in Figure 2.6. By dividing these two CO_2 contents, a dilution ratio (solid bars shown in Figure 2.7, panel b) was calculated and then compared with a theoretical dilution ratio (hashed bars in Figure 2.7, panel b) calculated based on measured volumetric flows of all inlets and outlets of the probe.

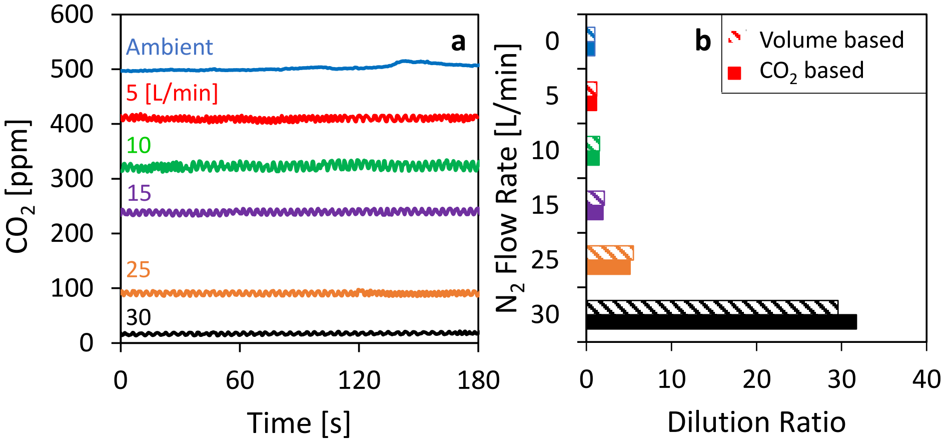

Figure 2.7: Primary dilution ratio characterization of the sampling probe. Panel (a) shows CO_2 concentrations measured with a LI-COR LI-850 CO_2 analyzer at the exit of the sampling probe with changing nitrogen flowrates being supplied for first stage dilution. Panel (b) shows estimated dilution ratios using volumetric flow rate measurements from calibrated mass flow controllers and compares it with the calculated dilution ratio from measured ambient and downstream CO_2 concentrations taken at points CO_2 (1) and CO_2 (2) in Figure 2.6.

It should be noted that all results discussed in the following sections were collected using a primary dilution nitrogen flowrate of 24 L/min, which resulted in a primary dilution ratio of ~4.5 based on cold test results. First stage dilution was further analyzed during flame tests in Section 3.2.1. The nitrogen flowrate of 24 L/min was chosen because it was noticed that when the nitrogen was set to 25 L/min, during flame testing, there would be moments when zero sample was pulled through the probe and nitrogen was the only gas travelling to the analysis instruments. Any nitrogen flowrate >25 L/min resulted in no sample being collected and making it to the analysis instruments.

Figure 2.8 shows the path and flowrates at which the sample travels. Much of the sample is pulled through the vacuum pump (28 L/min) and exhausted, while 3 L/min of sample is drawn off the vacuum line and through the Dekati diluter, model DI-1000, for a second stage dilution before travelling to the scanning mobility particle sizer (TSI SMPS 3938) for particle size distribution analysis. The Dekati diluter uses pressurised air passing by an ejector nozzle to cause a pressure drop and draw the sample into the diluter through a supply nozzle. The sample is then instantaneously diluted with the pressurised airflow. The SMPS is a benchmark multi-component-based tool that is capable of measuring mobility size distributions of particles in the nanoscale. It combines electrical mobility sizing and single particle counting to identify nanoparticle concentrations in discrete size channels [60]. The SMPS components include an electrostatic classifier, differential mobility analyzer (DMA), and condensation particle counter (CPC). The electrostatic classifier and DMA column use the electrical mobility technique to determine mobility diameters of particles or fractal-like structures. The CPC exposes the aerosol particles to a supersaturated vapor (water or butanol depending on the model) that condenses onto the surface of the particle and grows it large enough to be detected and counted by internal optical instruments.

There are two CO_2 analyzers that determine CO_2 mole fraction at the flame tip before the first stage dilution and after the second stage dilution before particles enter the SMPS to measure the overall dilution ratio of the collected sample. These analyzers have an internal pump to draw $\approx$0.75 L/min from the flame front and sample flow where an infrared detector is then used to detect CO_2 gas and benchmark it against a reference tube with zero CO_2 content. The placements of these CO_2 analyzers are shown in Figure 2.8. Soot agglomerates were collected on carbon coated copper grids for transmission electron microscopy (TEM) using a particle sampler (Naneos Partector TEM Sampler V2_3) to capture nano-scale images and measure d_p of the agglomerates. The thermal optical analysis (TOA) quartz filter placed before the SMPS was used to collect soot samples which were then used to measure composition (elemental and organic carbon contents) of the produced soot. TOA uses a heating process to detect organic and elemental carbon from a punch-out of a quartz filter. Continuous optical measurements with a laser confirm the original organic carbon and compare it to the burned off elemental carbon as the filter is heated in stages. Further explanation on the TOA analysis is provided in the supplementary material, Section A.7.

Laser induced incandescence (LII) was used to identify soot volume fractions in the sample flow upstream of where the quartz filter was placed. LII is a laser-optical technique for measuring thermophysical properties of soot. It uses a high-energy pulsed laser to heat soot particles to incandescent temperatures where the resulting thermal emission is recognized by laser diagnostics to quantify soot volume fraction [61]. In this work, LII was used to ensure sufficient soot particulate mass concentration where the quartz filter was placed, and to simply check that the filter would not be over- or under-loaded. LII-measured soot volume fractions were checked on the least and most sooting flame conditions and results confirmed sufficient soot mass concentration in the sample flow for effective filter loading. Further detailed and specific LII testing was not completed.

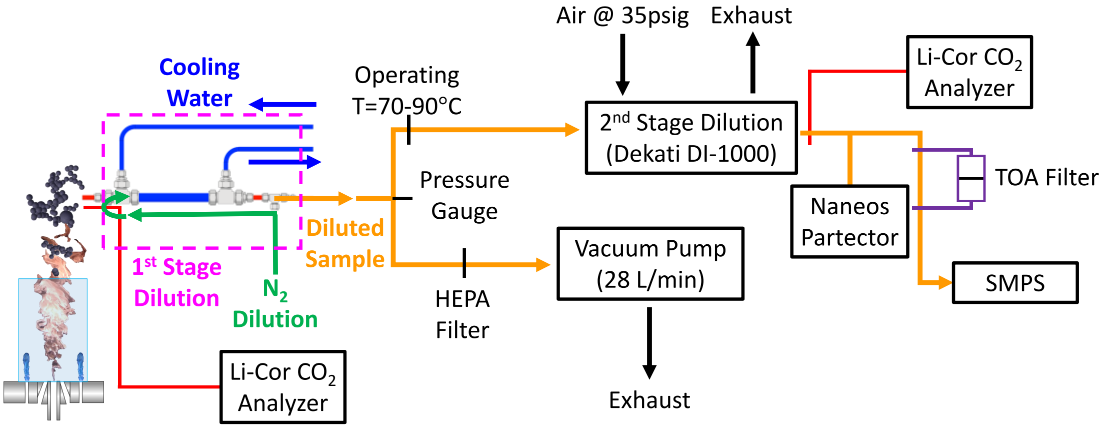

Figure 2.8: Schematic of the FSP burner and sampling assembly showing the pathway of the sample as it is collected from the flame and brought to the SMPS for particle mobility size distribution analysis. The hot sample is pulled through the probe by a negative pressure created downstream by the vacuum pump and the Dekati diluter. Most of the primary diluted and cooled sample (28 L/min) travels through the vacuum pump and to first exhaust line, while a smaller portion (3 L/min) travels through the Dekati diluter for further dilution with compressed air at 35 psig, and 1.5 L/min of that is directed to SMPS for analysis and the CO_2 sensor to quantify overall DR.

2.4 Assembly Model and Flame Imaging

Figure 2.9 illustrates the main framing of the FSP assembly showing the locations of the sampling probe, camera, height measurement reference stick, and burner positioning. The burner frame (Figure 2.9, parts 2 and 7) has linear rail bearings to allow burner positioning in the x, y, and z directions, making the HAB easily adjustable.

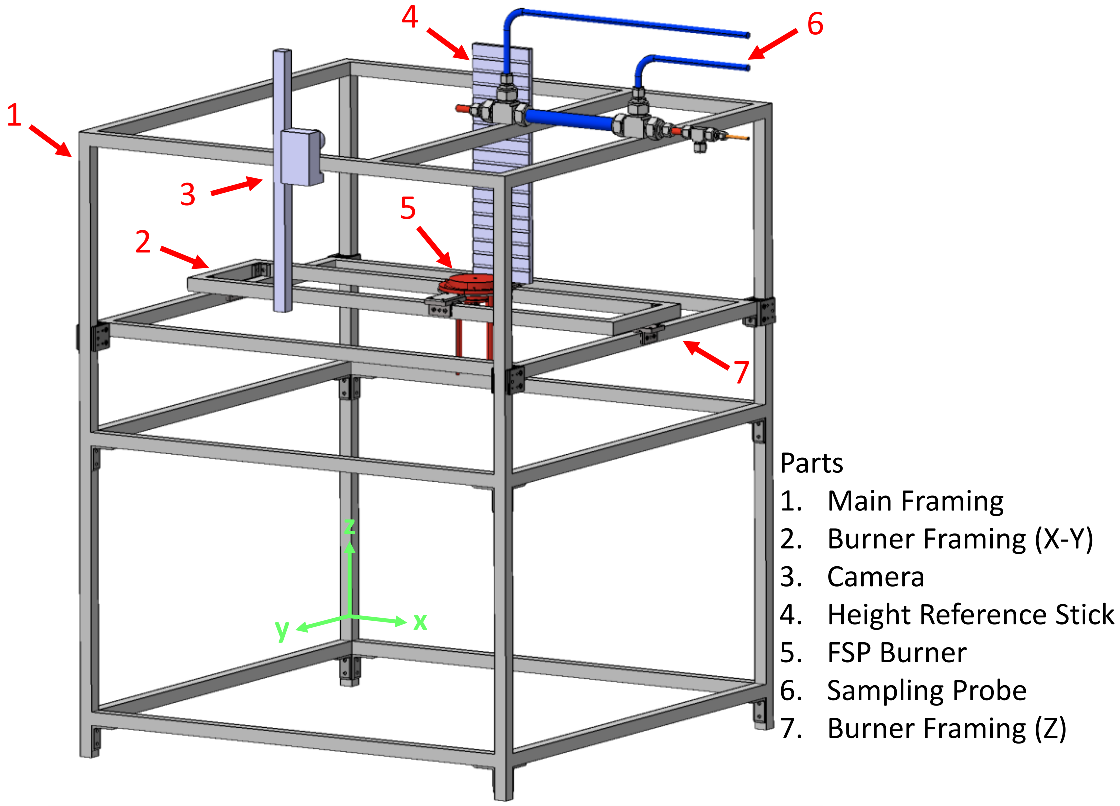

Figure 2.9: 3D model of the FSP framing assembly with main components labeled. The main framing (parts 1, 2, 7) composed of standard parts from McMaster-Carr including linear rail bearings on the burner framing (parts 2, 7) to position the burner in the x, y, and z directions. The camera (part 3) is fastened to the side of the main framing in a static position for repeatable images.

A camera (Figure 2.9, part 3) was fixed to the main frame of the FSP setup to take images of each flame. Camera settings remained constant for each fuel at individual flame conditions and are noted in Table 2.5. The flame heights were interpolated and calculated by using ImageJ software (further discussed in Chapter 3 and the Supplementary Materials) and the reference measuring stick that can be seen on the left-hand side of each flame image. Ten photos of each flame condition were taken, and the displayed flame heights are the averages of the measurements taken from the ten photos.

Table 2.5: Camera settings and flame height for all fuels and flame conditions.

Flame Condition	Exposure Time [s]	ISO	Aperture	Average Flame Height, $\bar{h}$ [mm]		
				Jet A1	C10	ATJ
10/3.00	1/8000	2000	*f*/3.6	231	222	217
12/2.50		1000		303	275	267
12/2.00		500		322	306	321

*All images taken with a 20 mm focal length.

Chapter 3: Results

3.1 Flame Heights

A DSLR camera (Canon EOS 60D) was fastened to the burner assembly main framing and used to take pictures of the varying flame conditions. A specific combination of settings was used for each flame condition, and that setting remained consistent for the condition when the fuels changed. These setting combinations are outlined in Table 2.5. A height reference stick was positioned behind the flame with markings at intervals of 50 mm. By using ImageJ software, a scale for the distance-to-pixels in the image was defined, and lines were drawn from the tip of the flame across to the measurement stick. A correction for the height difference between the surface of the burner and bottom of the measurement stick was applied, and the height of the flame from the burner surface to the unseparated flame tip was defined. A detailed measurement procedure is outlined in the supplementary material, Section A.5.

Figure 3.1 illustrates example photos for varying fuels and flame conditions. The 10/3.00 flames (refer to Table 2.3 for flame condition details), with the highest Reynolds number of 9100 and lowest burner equivalence ratio of 7, are consistently the shortest and brightest flames. However, it is important to note that these flames are highly turbulent, and the camera shutter speed was set high (1/8000 s), so flame heights spread considerably from the average. Despite this, trends for flame conditions were still identified, but differences between fuels for each flame condition are minimal. This made it too difficult to draw any conclusions on how chemical compositions of the fuels changed visual effects of the flame.

Figure 3.2 shows the average flame heights and variability across ten different images for each fuel and flame condition. The box and whisker chart identifies the 2nd and 3rd quartiles (boxes) where 50% of the data resides, and the whiskers extend to show the total spread of the flame heights measured. Unique height measurement spreads are identifiable for each flame condition with little to no overlap in the 2nd and 3rd quartiles, but the data is too widespread to identify unique spreads across different fuels, for the same flame conditions. The arithmetic averages stay rather consistent across the changing fuels with heights of 217-231 mm, 267-303 mm, and 306-322 mm for 10/3.00, 12/2.50, and 12/2.00 flame conditions, respectively. However, these arithmetic averages were taken from only 10 images of each flame condition, and thus the calculated values do not constitute sufficient sample size to be statistically significant. Further improvements to the imaging procedure need to be made to have significant flame height measurements and imaging comparison between fuel and flame conditions.

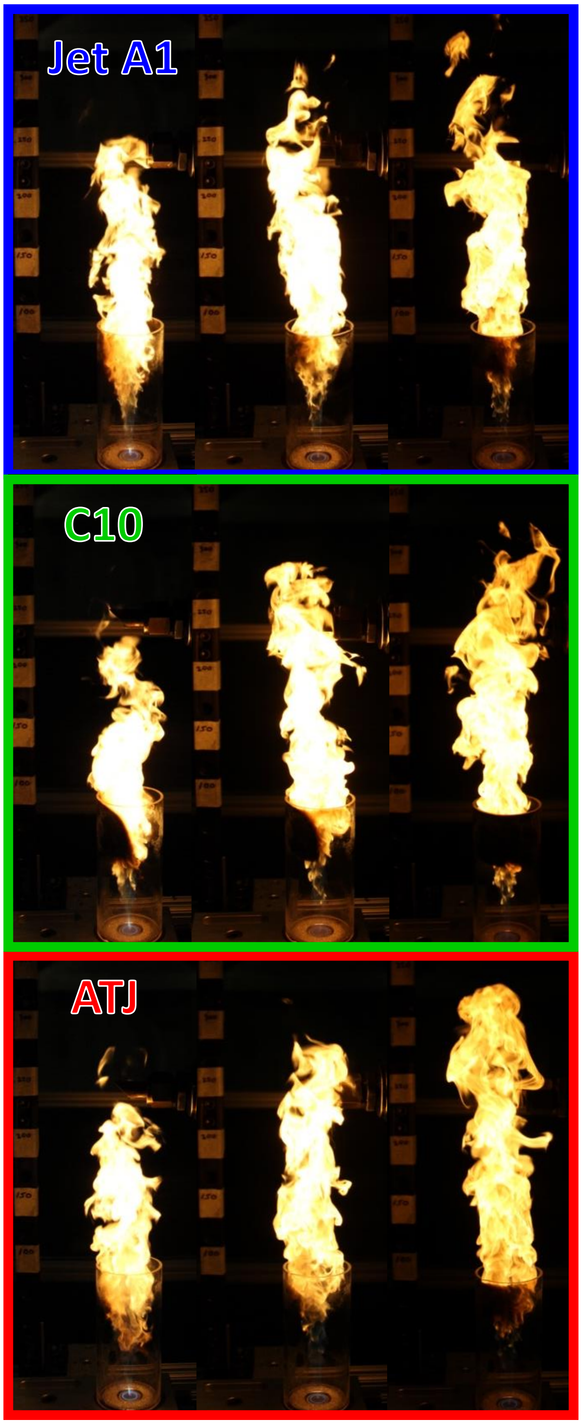

Figure 3.1: Flame imaging matrix showing photos taken for Jet A1 (blue), C10 (green), and ATJ (red) fuels and their three different flame conditions. Flame conditions from left to right are 10/3.00, 12/2.50, and 12/2.00. The average flame heights are labelled below each flame image. Camera settings for individual flame conditions across the different fuels were identical and are identified in Table 2.5.

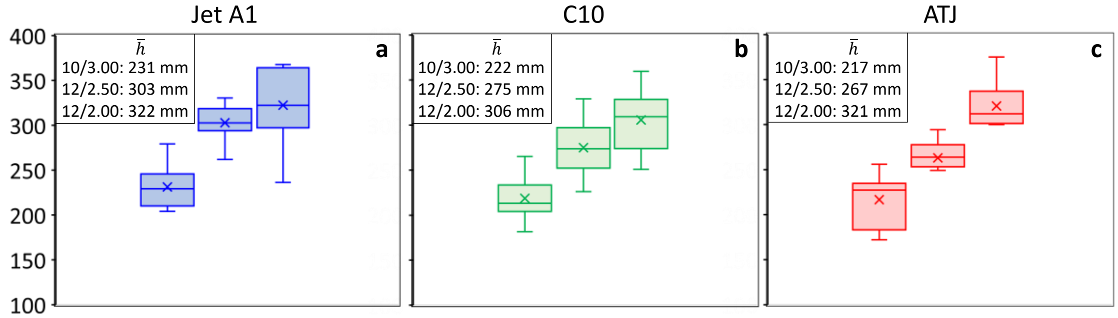

Figure 3.2: Box and whisker chart for flame heights of Jet A1, C10, and ATJ flame conditions measured from ten photos for each condition. The boxes represent the 2^{nd} and 3^{rd} quartile, where 50% of the flame heights reside, and the whiskers extend to identify the total spread of the measured flame heights. The "×" symbols denote the average heights ($\bar{h}$), which are also listed in the top left corner of each panel. Datasets in each panel, from left to right, represent flame conditions of 10/3.00, 12/2.50, and 12/2.00.

3.2 Particle Mobility Diameter Size Distributions

Particle mobility diameter size distributions are collected and characterized by a SMPS device operating with sheath and aerosol flows of 15 and 1.5 L/min, respectively, and a neutralizer and DMA column (model 3081) that characterized mobility diameters of soot particles within the size range of 6 nm to 220 nm. The aerosol flowrate setting is what controls how much sample is pulled into the SMPS for mobility size classification, while the sheath flow controls how the sample travels through the DMA column. Optimal SMPS settings are when the sheath to aerosol flow ratio is 10:1 [62]. The neutralizer uses bipolar diffusion charging to bring the sampled aerosol to a defined, steady-state charge distribution. The SMPS measures and counts particle mobility sizes in timed scans where an equal amount of time is allocated for each size bin to count particles in that size range before moving on to the next bin. The total scan time is preset by the user. In this work, four 45-second scans, immediately following one another, are taken for each flame condition. The first scan is considered a test run and allowed for any leftover particles from previous tests to be flushed through the system, and the results from the following three tests are then averaged. Within these three scans, the overall dilution ratio does not vary outside of 5%. All scans are completed with a collected sample temperature between 70 and 90°C, measured after the flow split seen in Figure 2.8. If the measured sample flow temperature was outside the desired range at any time during the scan, if fuel supply ran out mid-scan, or if the burner needed to be shut off for safety precautions, the scan was not included in the average and repeated to meet the specified test conditions.

The goal for this work was to produce repeatable size distributions where total number concentrations (N_{tot}) and mobility diameters (d_m) of soot maintain consistent values with variability $< 10\%$. This will minimize overlap of size distributions and morphology properties between different flame conditions so that fuel and flame settings will have unique and distinguishable sample measurements.

The d_m of an agglomerate is the equivalent diameter to a sphere that would experience the same migration velocity in a constant electric field [63]. The SMPS can measure agglomerate mobility diameter by using a force balance between the electrical force of a constant electric field on the net charges on the particle and the drag force the particle experiences [64]. Figure 3.3 shows a schematic of d_m and d_p with monodisperse primary particles.

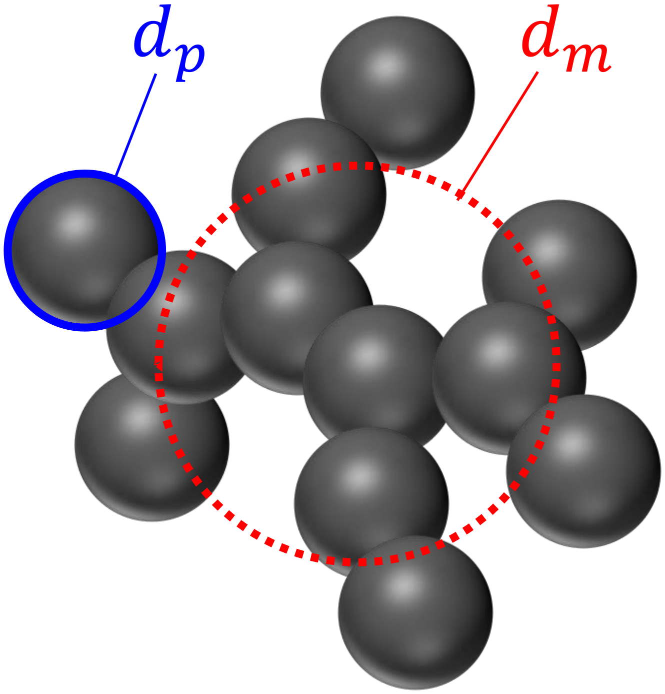

Figure 3.3: Schematic of a soot agglomerate identifying d_m and d_p with monodispersed primary particles.

3.2.1 Dilution Ratio

When soot interacts with surrounding air as it leaves a flame, particles oxidize and their concentration, size, and composition change [65]. High temperatures and excess reagents increase oxidation rates and reactions [65]. The soot samples collected during this study were cooled and quickly diluted due to the design of the sampling probe discussed earlier. This limited the composition and morphology changes in the soot sample as it travelled through the sampling assembly.

The overall dilution ratio, associated with the results discussed in this work, was measured by recording the CO_2 mole fraction at the probe inlet and after the second stage dilution, before the sample continues to the SMPS. The dilution ratio varied from 12-32 throughout all the recorded tests in this study which resulted in associated inconsistencies in the N_{tot}.

This, in turn, affected size distributions and geometric mean d_m values, as more dilution results in less coagulation and smaller agglomerates. Currently, the main cause of the highly variable N_{tot} and magnitude of size distribution curves is attributed to this change in dilution ratio. The dilution ratio was calculated by dividing the CO_2 concentration measurement after second stage dilution by the CO_2 concentration measured at the flame tip. Figure 3.4 illustrates the average CO_2 concentration (solid lines) for each measurement location and the variability (shaded areas) for each flame condition using Jet A1 fuel. The Dekati CO_2 concentration (blue) showed a step decrease in average CO_2 and less variability from the 10/3.00 to 12/2.00 flame conditions, whereas the probe CO_2 concentration (red) remained consistent from flame to flame for both the average and variability. Since no correction was made to the probe CO_2 concentration, and it was measured directly from the flame, there was no control of limiting that variation. Due to the turbulent nature of the flame, variability was expected in the probe; however, the CO_2 concentration after second stage dilution (Dekati) was expected to remain relatively constant. This was not the case throughout the experiments, and speculations as to why are discussed later in this section. Note that the Dekati and probe CO_2 concentrations are on different scales by an order of magnitude.

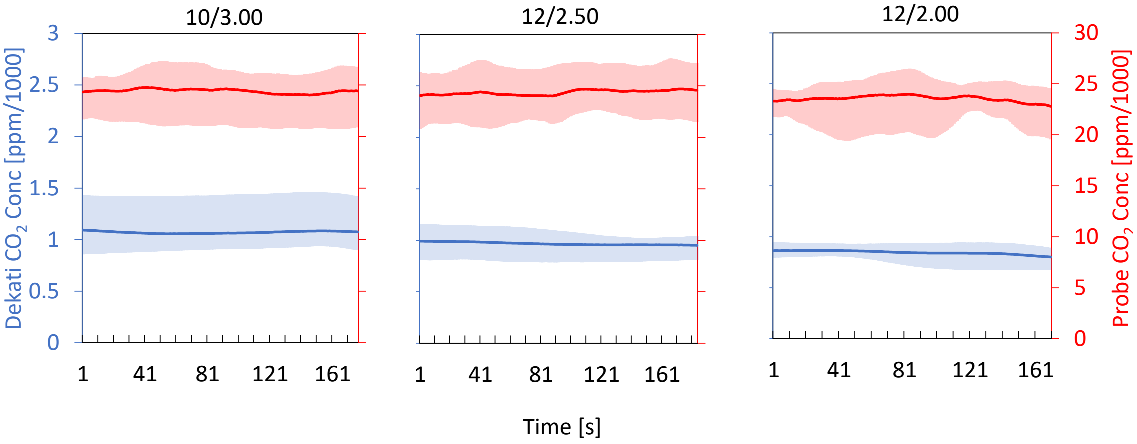

Figure 3.4: The average Jet A1 CO_2 concentration at the tip of the probe (red) and after the Dekati dilution (blue) for the three flame conditions (10/3.00, 12/2.50 and 12/2.00). The shaded area represents the maximum and minimum value at any given second. As the flame becomes less turbulent (10/3.00 compared to 12/2.00), there is less variation in the Dekati CO_2 concentration, with the average content around 1000 ppm. The average probe CO_2 concentration remains constant throughout the various flames, at just below 25000 ppm, with limited deviation.

A complete solution for producing a constant and repeatable dilution ratio has not been found for this setup yet. Current factors that affect the dilution ratio include: inconsistent CO_2 content in the compressed air supply, filter soot cake build-up (Figure 3.5) reducing exhaust flowrates, and soot sample flow temperatures (although sample gas temperatures are not always controllable).

Figure 3.5: Two filters that are used in the sampling line before the vacuum pump. The top filter (black) is after a days-worth of flame testing, and the bottom filter (white) is an unopened replacement. The blackness seen on the top filter is soot cake build-up filtered out of the exhaust flow before passing through the MFC and vacuum pump. As the soot builds up, flow is restricted through the vacuum.

The overall dilution ratios listed in the results of this work are calculated by dividing the measured concentration of CO_2 downstream of the 2nd stage dilution from the measured concentration of CO_2 at the point of sampling in the flame. This technique assumed that the compressed air, provided from a central building compressor, for the second stage dilution had the same CO_2 concentration as the ambient room. This is generally a fair assumption as the compressor takes outside or ambient room air as the source air, compresses it, and then provides it to wall ports throughout the lab. The surrounding outdoor CO_2 concentration around the building of this experiment took place in was about 450 ppm, and the CO_2 concentration in the FSP lab was 430-470 ppm depending on how many people were present.

As discussed later in Figure 3.10 and Figure 3.11, the dilution ratio varied between 12-30, and as discussed earlier, this variation was random from day-to-day. There is currently not a clear answer as to why this was the case. Further investigation into the overall dilution ratio and in-depth analysis on both first and second stage dilutions are examined in this section.

A characterization of all the inlets and outlets in the two-stage dilution assembly was completed with and without the flame operating. When the flame was not in operation, both CO_2 analyzers were calibrated and ran for 10+ minutes to measure ambient room CO_2 concentrations on multiple days. Concentrations between 430-470 ppm were observed depending on the number of people present in the lab. Next, the CO_2 concentration in the compressed air supplied from the central building compressor was measured for 10+ minutes on multiple days. These results are shown in Figure 3.6 and unexpected values and oscillations were observed. It was assumed that the CO_2 concentration in the wall would be within 10% of the lab room concentration and constant. Seen in Figure 3.6, this was not the case; CO_2 concentrations oscillated with varying amplitudes and wavelengths on two different days of testing.

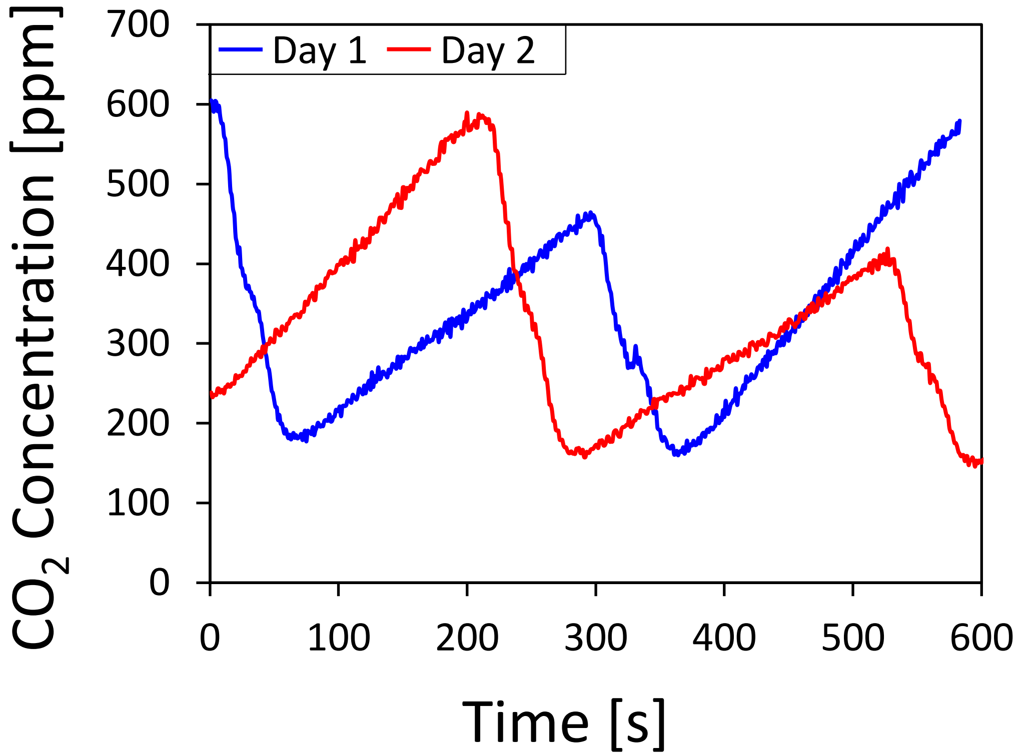

Figure 3.6: Concentrations of CO_2 measured from the compressed air wall connection in the FSP lab on two different days. The wall air source comes from a central compressing unit in another building about 500 m down the road.

Following this, another test was completed where room air mixed with the oscillating compressed wall air in the Dekati diluter, and the output CO_2 concentration was measured. This was done on multiple days and the results of the output CO_2 concentration can be seen in Figure 3.7. These results show similar oscillations, although the CO_2 concentrations reduced to oscillate between 100-275 ppm. The central compressor that supplies compressed air to this lab room has been investigated and discussions with the engineers responsible for operation were had, but no definitive reason was given as to why there were regular oscillations in the CO_2 concentrations or why it dropped below ambient or outside air concentration levels.

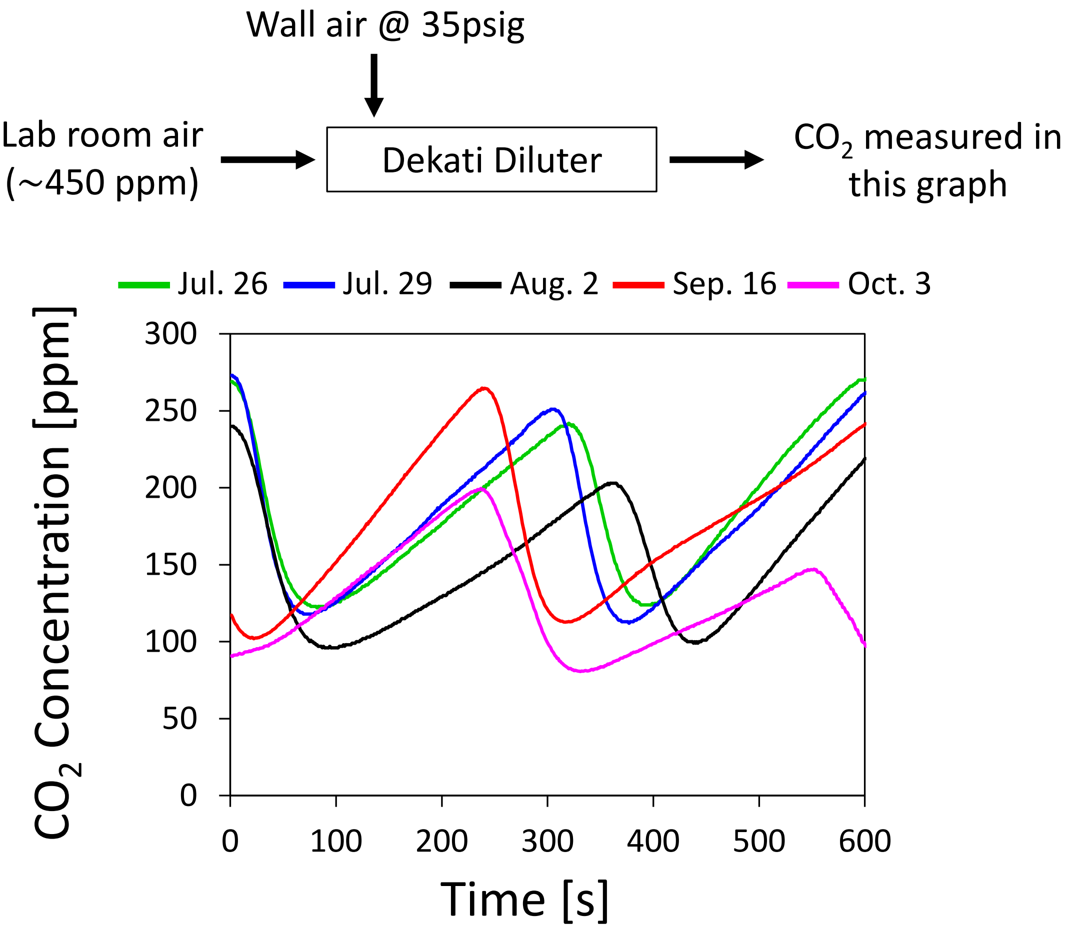

Figure 3.7: Concentrations of CO_2 measured after mixing compressed air from the wall and mixing it with ambient lab room air.

Upon this discovery, a full assessment on the dilution and sampling assembly during flame testing was completed using the CO_2 analyzers at four points of interest. The flame used for the following results was a 12/2.50 flame condition with Jet A1 fuel. The measurement points were at the flame (a), after primary dilution in the probe with N_2 gas (b), the sample after secondary dilution that is sent to the analyzers (c), and the wall air (d). Figure 3.8 illustrates the four points of interest along with their associated CO_2 concentration measurements. It is important to note that only two CO_2 analyzers were used and thus the data in Graph (1) was measured at the same time, then the analyzers were moved to measure the data in Graph (2). Graph (1) shows that after 1st stage dilution the CO_2 content in the sample was relatively constant (green) before entering 2nd stage dilution. Once the sample passed through 2nd stage dilution, the oscillation of CO_2 concentration from the wall air (blue) propagated into the sample and a resulting damped oscillation is seen in the final sample (black) before analysis. As mentioned before, the dilution ratio was calculated by taking the average CO_2 concentration at the flame (red) and dividing it by the average CO_2 concentration of the sample (black). However, the analysis seen in Figures 3.6 – 3.8 was only completed after the particle mobility size distributions were taken and extreme day-to-day dilution variability was recognized, so it is not possible to confirm if the variation was only due to the unpredictable wall air supply.

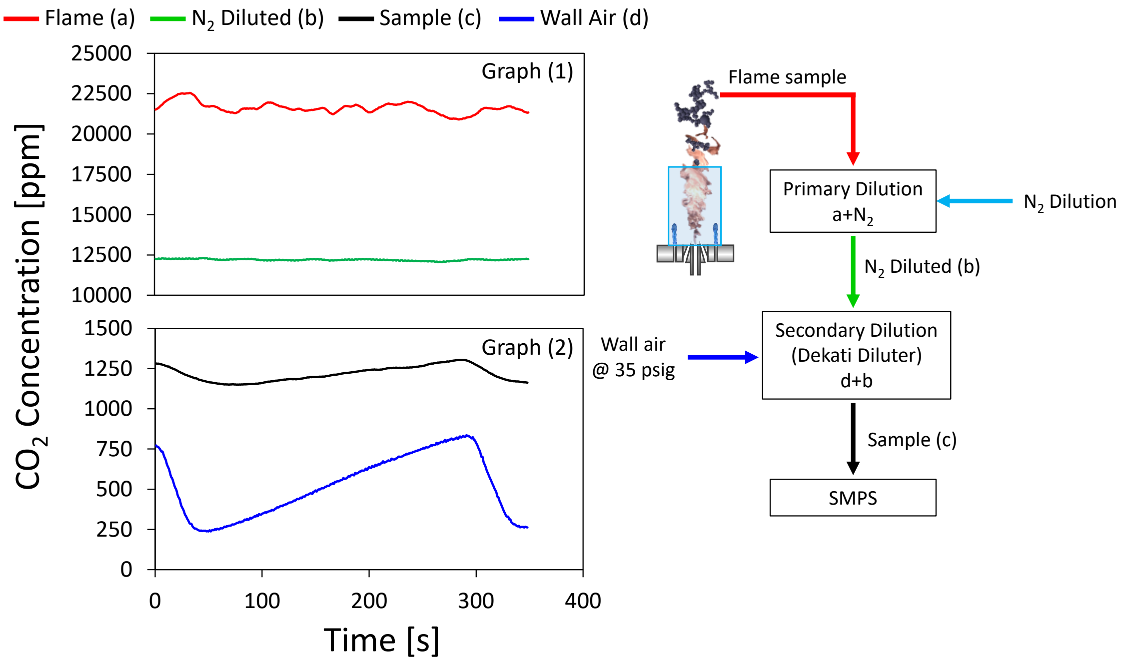

Figure 3.8: Concentrations of CO_2 during a flame test with a 12/2.50 flame condition. CO_2 measurements were taken at the flame (red), after primary dilution from the sampling probe with N_2 (green), after secondary dilution from the Dekati diluter (black), and from the compressed air wall supply (blue). Two CO_2 analyzers were used and data in Graph (1) was taken simultaneously, then the analyzers were re-positioned and the data in Graph (2) was taken simultaneously.

Due to these random uncertainties and unpredictability in our dilution air supply, a meaningful in-depth uncertainty analysis on the previously measured dilution ratios was not done. However, to improve on these day-to-day inconsistencies in dilution ratio measurement for future work, the compressed air supply for the Dekati was switched from the lab wall air to an individual cylinder air mixture with zero CO_2 content (confirmed with one of the calibrated CO_2 analyzers used during this experiment). This adjustment required new measurements and an uncertainty analysis was completed.

Tests were done with a Jet A1 12/2.50 flame condition, where CO_2 measurements were taken at the flame, after 1st stage dilution (Point 1) and after 2nd stage dilution (Point 2). Due to the limitation of having only two CO_2 analyzers available, the analysis was done in two different time stages, however, the flame remained active during the repositioning of the analyzer from the flame to Point (2). The first stage of analysis measured CO_2 concentration from the flame where the probe was sampling (Figure 3.9, “flame”) and after the 1st stage of dilution (Figure 3.9, “Point (1)”). Figure 3.9 shows these values as a function of time along with a 1st stage dilution ratio (solid green line). The average 1st stage dilution ratio calculated here was 1.84±0.08.

Figure 3.9 graph (b) is similar to Figure 3.9 graph (a) but shows the CO_2 concentrations during the 2nd time stage for the 2nd stage dilution ratio analysis. Here, the blue dashed line is still the CO_2 measurement at Point (1) and the dashed-dotted magenta line is the measured CO_2 concentration at Point (2). The green line shows the instantaneous calculated 2nd stage dilution as a function of time. The average 2nd stage dilution ratio was 13.36±0.56.

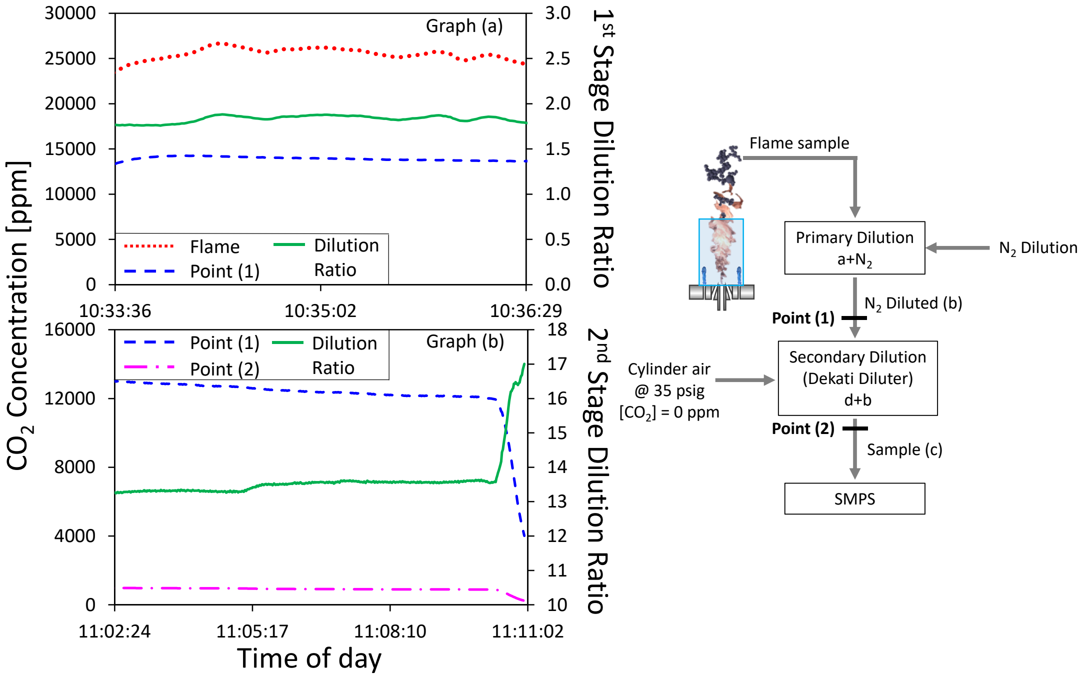

Figure 3.9: Concentrations of CO_2 at the flame (red dotted line), after first stage dilution and before 2nd stage dilution (blue dashed line, Point 1), and after second stage dilution (magenta dash-dot line, Point 2). Instantaneous 1st and 2nd stage dilution ratios (solid green line) as a function of time. Graph (a) and Graph (b) were taken at two different time stages but measured from the same continuous Jet A1 12/2.50 flame.

The overall dilution ratio was calculated by multiplying the 1st stage by the 2nd stage and resulted in a value of 24.5±2.8, accounting for propagation of uncertainties between the two CO_2 analyzers. A summary of the calculated mean dilution ratios and their associated uncertainties are given in Table 3.1. Concentrations of CO_2 were measured every second and the mean values were calculated over the time spread seen in the x-axes of Figure 3.9. Errors were calculated using a 95% confidence interval with the mean CO_2 concentration and its standard deviation in the given time stage. The manufacturer's uncertainty for the Li-Cor 850 CO_2 analyzer is 1.5% of the reading.

Table 3.1: Dilution ratios with uncertainties at a 95% confidence interval.

Time	CO_2 Measurement Point	Mean	Standard Dev.	Error	Dilution Ratio with 95% CI
10:33-10:36 (1st stage dilution)	Flame	25581	557	386	1.84±0.08
	Point (1)	13396	189	210	
11:02-11:11 (2nd stage dilution)	Point (1)	12655	392	191	13.36±0.56
	Point (2)	947	45	14	

3.2.2 Mobility Size Distributions

Figure 3.10 illustrates the soot agglomerate d_m distribution for particles sampled from the three flames for each fuel. Each line in panel (a-i) represents a distribution on a given test day. For example, panel (a) has nine different lines representing nine different days of test results. Panels (a-c), (d-f), and (g-i) are for flame conditions 10/3.00, 12/2.50, and 12/2.00, respectively, while vertical columns separate the three different test fuels. Individual distributions are color coordinated with the respective color bar on the right-hand side of Figure 3.10 to match each distribution with the respective overall dilution ratio measured during that flame test. The flame condition with the most variation in its size distribution is the 10/3.00 flame, for all fuels. Repeatable number concentrations were expected to be difficult due to the wide variations experienced in the measured dilution ratios, which can be seen in all panels, as the peak magnitude in the distribution varies, sometimes as much as 15% (Figure 3.10, panel a).

The measured dilution ratio results for C10 flame conditions (panels b, e, and h) show the most variation, which can be seen by the more obvious color changes when compared to the other fuels. Increased dilution ratio resulted in lower number densities as illustrated for the C10 flames (panels b, e, and h). This is because a larger dilution ratio results in fewer particles/cm^3 to be collected and sent to the SMPS for analysis, resulting in a reduced N_{tot}, which tends to be reflected by a reduced peak magnitude in the distribution curve. Dilution ratio variation for the ATJ flames is less than that of the other two fuels. This is identifiable in panels (c), (f), and (i), as the colors coordinate to a dilution ratio between 12-20, whereas the C10 and Jet A1 flames span dilution ratios from 12-32. The Jet A1 flames specifically (panels a, d, and g) show this wide variation in dilution ratio, but seemingly less of the expected trend and more unpredictable distributions. However, despite the variations in total number concentrations, the distribution for 12/2.50 (panels d, e, and f) and 12/200 (panels g, h, and i) flames show similar lognormal distributions suggesting that particle sizes are more repeatable than number concentrations. Similar work, using the same FSP burner and a similar sampling assembly, by Trivanovic, Kelesidis, and Pratsinis, presented normalized size distributions and found, similarly, that total number concentrations repeatable to within 10% were difficult to attain [34].

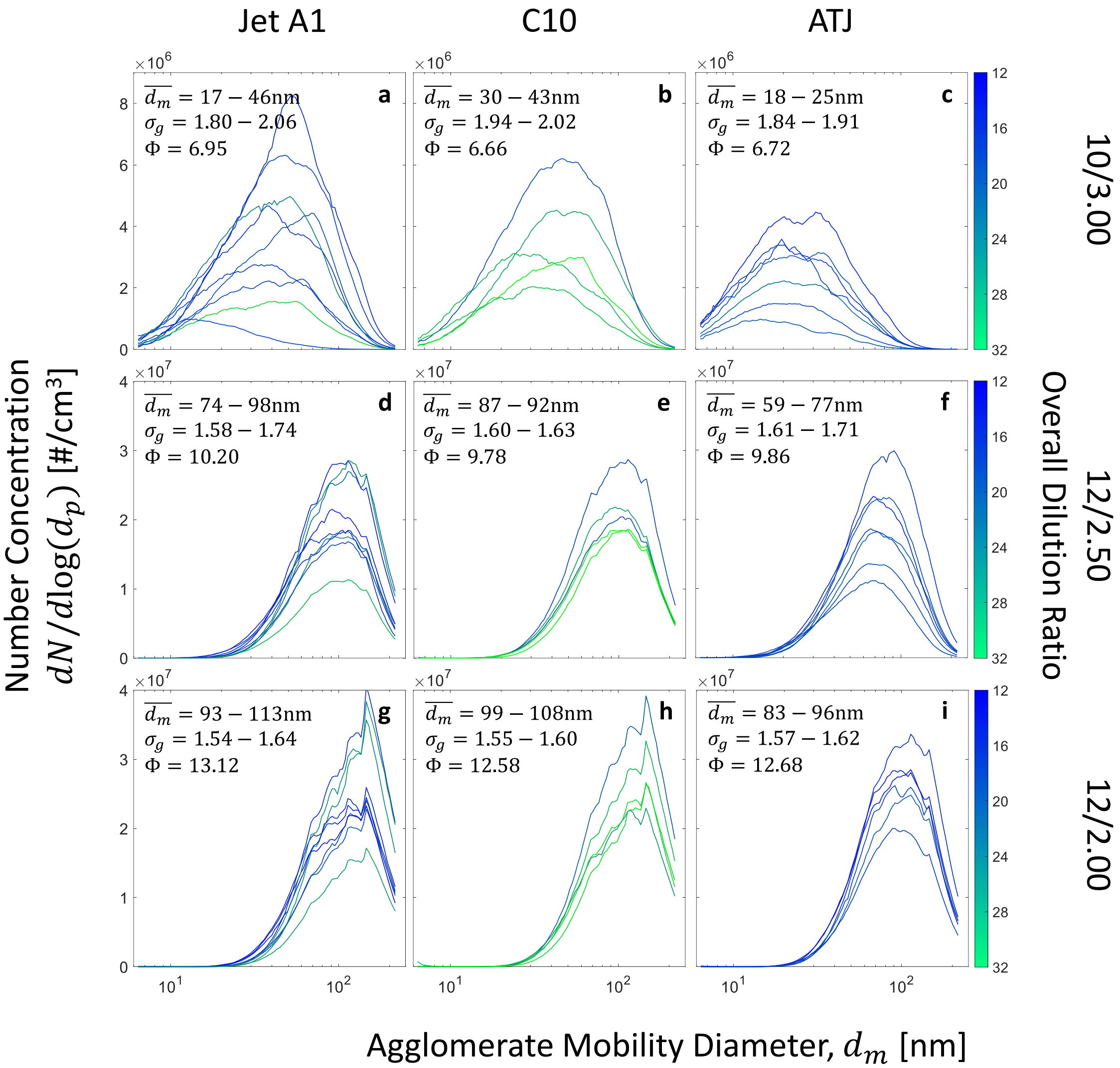

Figure 3.10: Mobility particle size distributions for three different fuels (column 1: Jet A1, column 2: C10, and column 3: ATJ) and three different flame conditions (row 1: 10/3.00, row 2: 12/2.50, and row 3: 12/2.00). Each individual line represents a different test day. The color of the line is associated with the color bar by the dilution ratio that was measured on the day of testing. The range of geometric mean mobility diameters ($\overline{d_m}$), their geometric standard deviations (σ_g), and the burner equivalence ratios (Φ) for these distributions are noted in the top left corner of each panel.

Aerosol particle motion depends on the relative value of gas mean free path to particle diameter. This relationship is defined by the Knudsen number and is given by equation (11):

$$Kn = 2\lambda/d \tag{11}$$

where λ is the gas mean free path and d is the particle diameter. Aerosol particle motion falls into three regimes: free molecular regime when $d \ll \lambda$, continuum regime when $d \gg \lambda$, and a transition regime in between. In the free molecular regime, particle motion can be described by the kinetic theory of gases, while in the continuum regime, particle motion can be described by the Navier-Stokes equations. For the transition regime, interpolations must be devised specific to the diffusion, coagulation, or condensation processes. When the particles sampled in this work reach the analysis instruments, after cooling and dilution, they are travelling in room temperature air. Room temperature air has a mean free path of ~67 nm [66] and particle geometric mean mobility diameters in this work range from 17-113 nm. This means that our samples are in the transition regime as λ_{air} is neither $\ll$ nor $\gg d$.

For aerosols undergoing coagulation with high number concentrations, a self-preserving size distribution is met over time. Geometric standard deviations (σ_g) for these distributions in different regimes have been identified and show that the geometric size distribution plateaus which means that the normalized size distribution becomes invariable with time. Mobility diameters of agglomerates with a self-preserving size distribution have a σ_g of 2.03 [67] and 1.50 [17] in the free molecular and transition regime. Each panel in Figure 3.10 show the range of σ_g for day-to-day tests of all flame conditions, where σ_g stays within 1.54-2.06. These results confirm that all distributions covered in this work met self-preserving size distributions in either the free molecular or transition regime.

3.2.3 Geometric Mean Mobility Diameters

Previous work from jet engine field tests have found that soot agglomerates emitted at high thrust tend to not exceed a geometric mean mobility diameter, $\overline{d_m}$, of 70 nm [41] while maintaining $d_p < 20$ nm [42] and EC/TC > 0.8 [42]. The $\overline{d_m}$ is calculated by taking the n^{th} root of the product of all mobility diameters. In 2021, Kholghy & DeRosa showed that FSP could produce soot agglomerates with $\overline{d_m} < 70$ nm, using Jet A1 fuel and an identical FSP burner and similar sampling probe to those used in this study [35]. Trivanovic, Kelesidis, and Pratsinis confirmed these findings by Kholghy & DeRosa and experimented further with enclosed flames and reduced fuel flow rates [34]. In this work, soot agglomerate d_m were analyzed for comparison between three different fuels at flame conditions of 10/3.00, 12/2.50 and 12/2.00.

Figure 3.11 illustrates $\overline{d_m}$ from the measured particle mobility size distributions at different days as shown in Figure 3.10. Increasing the burner equivalence ratio increased the $\overline{d_m}$, and for some fuels these values were different enough that no overlap was seen in the selected flame conditions of this study. However, similarly to day-to-day differences in measured size distributions for the 10/3.00 flame seen in Figure 3.10, the 10/3.00 $\overline{d_m}$ values demonstrate the largest standard deviation (σ) from the average by percentage: 26% for Jet A1, 9% for ATJ, and 15% for C10. As the burner equivalence ratio increased, the arithmetic mean of $\overline{d_m}$ values across multiple days of testing ($\bar{x}$) increased and σ (by percentage) decreased, showing an improvement in $\overline{d_m}$ repeatability. The most consistent $\overline{d_m}$ for Jet A1 and ATJ was with a 12/2.00 flame condition (the most sooting flame condition), with standard deviation percentages of 3.4% for Jet A1 and 4.7% for ATJ. The C10 fuel shows good consistency for both 12/2.50 and 12/2.00 flames with percentages of 2.7% and 3.4%, respectively. However, it is important to note that the C10 fuel was tested for fewer days and not on the same days as Jet A1 and ATJ. Panels (d), (e), and (f) of Figure 3.11 further identify the spreads and deviation from the average for day-to-day comparison. These panels are box and whisker charts where the “×” symbol denotes $\bar{x}$ from panels (a-c), the boxes represent the 2nd and 3rd quartiles where 50% of the data is located, and the whiskers extend to show the total spread of $\overline{d_m}$.

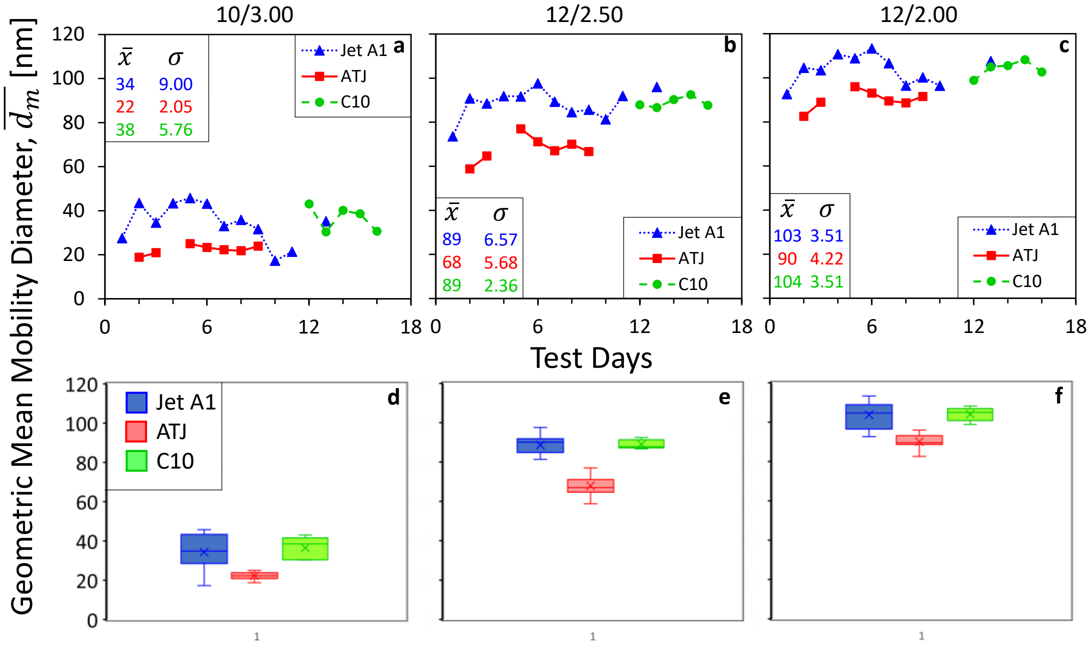

Figure 3.11: Geometric mean mobility diameters, $\overline{d_m}$, for all three fuels at three different flame conditions; (a) 10/3.00, (b) 12/2.50, (c) 12/2.00. Average $\overline{d_m}$ ($\bar{x}$) for all days and standard deviations (σ) from day-to-day are recorded in each panel. Jet A1 and C10 $\overline{d_m}$ values were very similar for all conditions while the ATJ values sampled consistently smaller in size across all conditions and days. Panels d, e, and f show the $\bar{x}$ denoted as an × and the boxes represent the 2nd and 3rd quartiles where 50% of the data resides. The whiskers extend to the total spread of each dataset.

With only 12, 5, and 7 days of testing for the Jet A1, C10, and ATJ fuels, respectively, there is not a sufficient set of data points to complete a statistical significance test. However, as mentioned before, each point in panels (a), (b), and (c) of Figure 3.11 are an average of the three SMPS scans taken on that day. If this is expanded and each individual data set is considered (3 scans multiplied by 12, 5, and 7 days of testing), there is sufficient data to complete a confidence interval test which demonstrates the probability that the average would be within a given range. In this scenario, the confidence interval test used all the individual experimental $\overline{d_m}$ values from each fuel and flame condition and provided a range of sizes for where the $\overline{d_m}$ would be expected to fall. For this data, a 95% confidence interval was used and the ranges for each fuel and flame condition are given in Table 3.2.

Table 3.2: $\overline{d_m}$ intervals with 95% confidence for all flame conditions.

95% CI	Flame Condition					
	10/3.00		12/2.50		12/2.00	
	Low	High	Low	High	Low	High
Jet A1	40.4	46.4	96.7	100.2	111.6	114.8
C10	42.7	48.2	98.2	100.1	112.8	116.1
ATJ	26.5	28.3	74.5	77.2	98.5	100.8

The results from the confidence interval test are promising and show repeatable results within the goals for this project. However, more day-to-day data is required for a proper day-to-day confidence test, using the averages seen in Figure 3.11 as the sample points.

To further analyze these day-to-day variations, the panels in Figure 3.12 isolate the $\overline{d_m}$, N_{tot}, and dilution ratio for a given test day. It also shows how these values changed with the flame condition as the burner equivalence ratio was adjusted. Panels (a)-(c) show the $\overline{d_m}$ as a function of test days and flame condition. Clearly shown here, the flame conditions vary enough that $\overline{d_m}$ values do not overlap on individual days and a day-to-day $\overline{d_m}$ trend for each flame condition of a particular fuel is identified. Similarly, in panels (d)-(f), the N_{tot} are displayed. The 12/2.50 and 12/2.00 conditions are similar here, but still show the 12/2.50 conditions sampling consistently fewer particles than the 12/2.00 condition. The

10/3.00 flame condition consistently samples less N_{tot} (about half an order of magnitude), which was expected as the flame was smaller and further away from the probe, so the particles have more time to oxidize before collection, and the 10/3.00 flame has the smallest burner equivalence ratio.

Panels (g)-(i) show the overall dilution ratio measured for the respective $\overline{d_m}$ and N_{tot} in the earlier panels, as it changes from day-to-day. This helped explain some of the spikes in N_{tot} and the trends expected and explained in Section 3.2.2. In most cases here, dilution ratio and N_{tot} have an inverse relationship, as expected. This can be seen evidently on day 7 for Jet A1 (panel g), day 14 for C10 (panel h), and day 6 for ATJ (panel i), where a spike in dilution ratio causes an inverse spike in N_{tot}. However, this is not true for all cases. No relationship between changing dilution ratio and $\overline{d_m}$ is seen with these datasets. The dilution ratio spikes on days 7 (panel g), 14 (panel h), and 6 (panel i), do not have a resulting effect on $\overline{d_m}$.

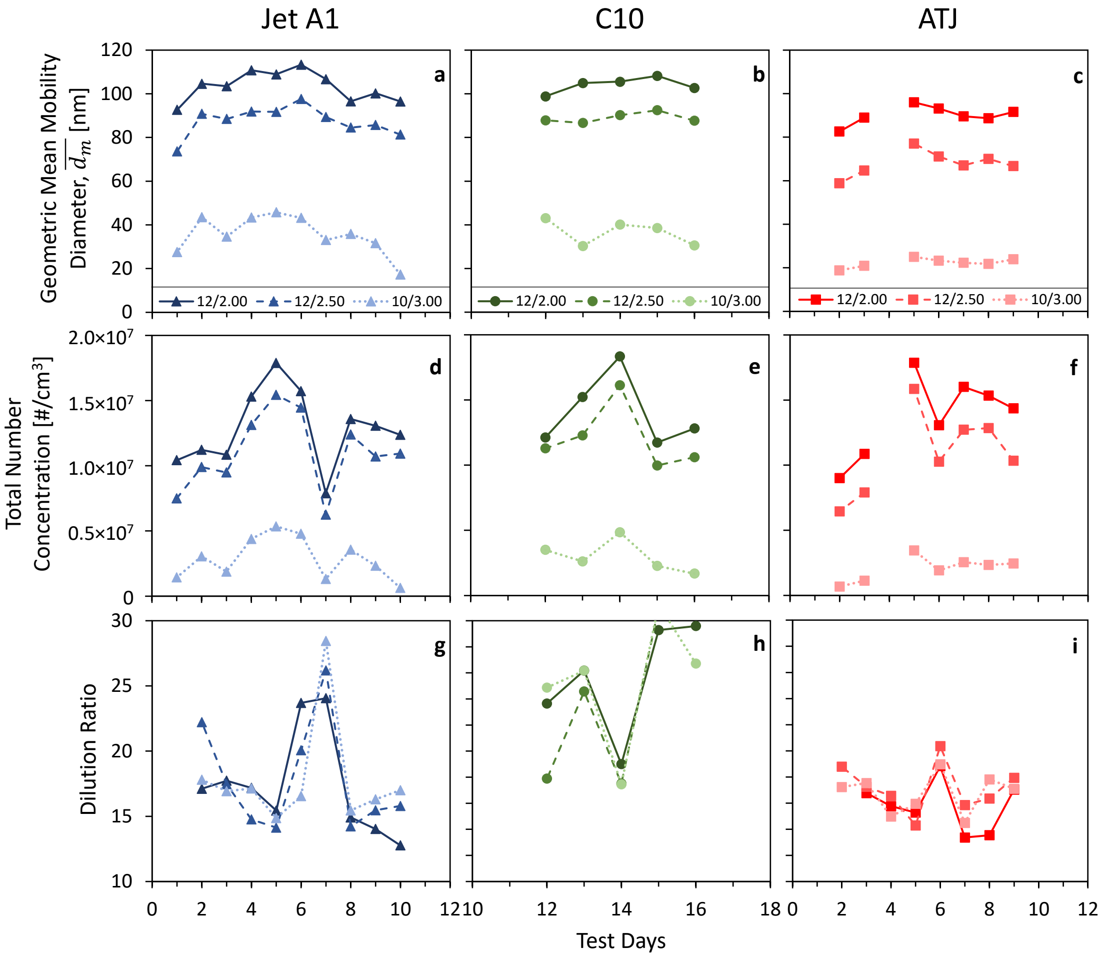

Figure 3.12: Geometric mean mobility diameter ($\overline{d_m}$), total number concentration (N_{tot}), and dilution ratio values for Jet A1 (blue triangles), C10 (green circles), and ATJ (red squares) at 12/2.00 (solid line), 12/2.50 (dashed lined), and 10/3.00 (dotted line) flame conditions across various days of testing. Jet A1 and ATJ were tested on the same days (day 1-10) while C10 was tested on days 12-16.

As discussed in Section 2.2, and referring to Figure 2.5, it was expected that the ATJ SAF (red squares) would produce the smallest number concentration and smallest particles between the three fuels chosen for this experiment. Seen in Figures 3.11 and 3.12, this is confirmed as the mobility particle size distributions are repeatedly smaller than Jet A1 and C10 results. Currently, this is attributed to the fuel's < 1% mass concentration of aromatics and cyclo-paraffins. Alternatively, the Jet A1 and C10 fuels showed similar distributions and mobility size ranges for the changing fuel conditions. This is an interesting comparison because the aromatic contents in these two fuels (19% mass for Jet A1 and 27% mass for C10; see Figure 2.5) are quite different. However, where the C10 increased in aromatic content, it decreased to having little to no cyclo-paraffins present. The cyclo-paraffin mass percentage is the second most property after aromatic mass percent, from the four discussed in Section 2.2, to promote soot production. It seemed that for conditions tested in this experiment, the high aromatic content of C10 (27% mass percent) and little to no cyclo-paraffins created a similar sooting tendency as Jet A1 with 19% aromatics and 32% cyclo-paraffins. While concentrations and $\overline{d_m}$ were similar for Jet A1 and C10, the primary particle analysis differed more and is discussed in the next section.

3.3 Primary Particle Diameters

Typically, the geometric mean d_p ($\overline{d_p}$), calculated by taking the n^{th} root of the product of all diameters, of soot particles emitted from jet engines at high thrust levels is less than 20 nm [18]. The $\overline{d_p}$ is used to represent the size distribution of primary particles because previous work has identified that d_p from turboshaft engines operating on liquid jet fuel show lognormal or nearly lognormal distributions [68]. Therefore, if a $\overline{d_p}$ and σ_g are known for a given condition, a lognormal fit can be produced to identify the full distribution. These lognormal fits can be seen in Figure 3.13 as solid lines for each fuel and flame condition.

Earlier work on FSP made soot from open [35] and enclosed [34] spray flames of Jet A1, for various flame and test conditions, also produced soot agglomerates made of primary particles with $d_p < 20$ nm. This work looks at a comparison of soot d_p distributions for different fuels and flame conditions while maintaining $\overline{d_p} < 20$ nm. A Naneos Partector

TEM sampler pulls soot samples from the sampling flow (seen in Figure 2.8) and deposits them onto circular copper grids. TEM is used to capture nanoscale images of the soot agglomerates from all fuels and flame conditions. Using ImageJ software, identifiable primary particles are enclosed in a circle or an ellipse, and their surface area is used to calculate equivalent spherical diameters. Figure 3.13 demonstrates primary particle size distributions for Jet A1 (blue triangles), C10 (green circles), and ATJ (red squares) at flame conditions of 10/3.00 (top row), 12/2.50 (middle row), and 12/2.00 (bottom row). For all conditions, a lognormal fit (Figure 3.13, solid lines) using the σ_g and the $\overline{d_p}$ was suited to the experimental data (Figure 3.13, symbols) to show that primary particle size distributions can be estimated with a lognormal distribution.

The $\overline{d_p}$ ranged from 15.4-21.0 nm, 10.5-13.7 nm, and 9.7-18.4 nm for Jet A1, C10, and ATJ fuels, respectively. All but one flame (Jet A1, 12/2.00) exceeded the $\overline{d_p} < 20$ nm threshold with $\overline{d_p}$ = 21 nm. The value of σ_g for $\overline{d_p}$ ranges from 1.22-1.38, in good agreement with the value from previous FSP work of $\sigma_g =$ 1.25-1.30 by Trivanovic, Kelesidis, and Pratsinis [34] and σ_g = 1.25 by Kholghy and DeRosa [35] as well as a theoretical value of σ_g = 1.2 obtained from Discrete Element Modeling of soot made by coagulation and surface growth [69].

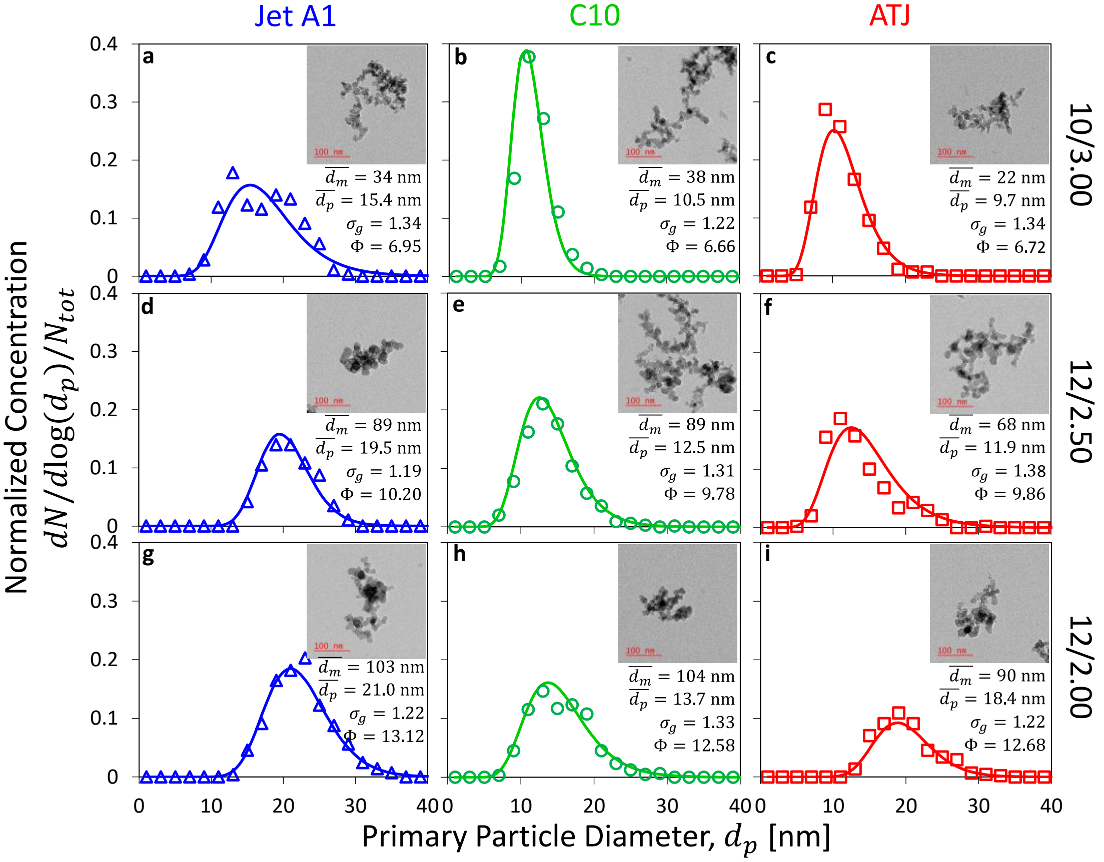

Figure 3.13: Normalized soot primary particle size distributions for Jet A1 (blue triangles), C10 (green circles) and ATJ (red squares) measured with ImageJ from TEM images and compared with a fitted lognormal distribution (solid lines) using measured $\overline{d_p}$ and σ_g. TEM images with 100 nm scale are displayed in the top right corner of each panel (a-i) and the $\overline{d_m}$ for the given flame condition is provided below the image for reference. The burner equivalence ratio for each panel is denoted by Φ.

3.4 Composition

Soot particles generated from jet engines are composed of organic, OC, and elemental, EC, carbon. The EC/TC ratio refers to the elemental carbon divided by the total carbon (TC = EC+OC) measured using TOA which detects the total carbon on the filter punch-out and differentiates the elemental from organic carbon material. Field studies have found that EC/TC ratios of jet engine soot emitted at high thrust levels are > 0.8 [42]. This work measures the EC/TC ratios for three different jet fuels and compares them across various flame conditions and previous FSP work. For this analysis, the NIOSH 930 protocol was used with a Sunset Laboratory OCEC Carbon Aerosol Analyzer (Model 5L – Main Oven Assembly and Model 4L – Methanator/Detector Assembly). This specific protocol was used because it is the typical protocol of choice for aviation-like soot. The EC/TC ratios in this study range from 0.55-0.97 with only the 10/3.00 flame condition samples having EC/TC $>$ 0.8. The 12/2.50 and 12/2.00 flame conditions are in good agreement with previous FSP work, identifying EC/TC ratios in the range of 0.81-0.90 [34] and 0.90-0.94 [35] using Jet A1 fuel. Figure 3.14 shows the EC/TC ratios as a function of $\overline{d_m}$ with black ×'s [35] and pink crosses [34] representing previous work and blue triangles, green circles, and red squares representing Jet A1, C10, and ATJ fuel results, respectively, for this work. There are six data points for each fuel which are associated with the 10/3.00, 12/2.50, and 12/2.00 flame conditions in this work. Two sets of data were taken with identical burner settings where the 1st set of data is shown with empty symbols and the 2nd set of data is shown with filled symbols. For each fuel, the smallest $\overline{d_m}$ is from the 10/3.00 flame condition and $\overline{d_m}$ increases as the condition changes to 12/2.50 and then 12/2.00. The data points extrapolated from previous work use different flame conditions and equivalence ratios; however, the results shown in Figure 3.14 remain comparable for EC/TC of Jet A1 (blue triangles) as a function of $\overline{d_m}$ except for one of the Jet A1 10/3.00 points (EC/TC = 0.54).

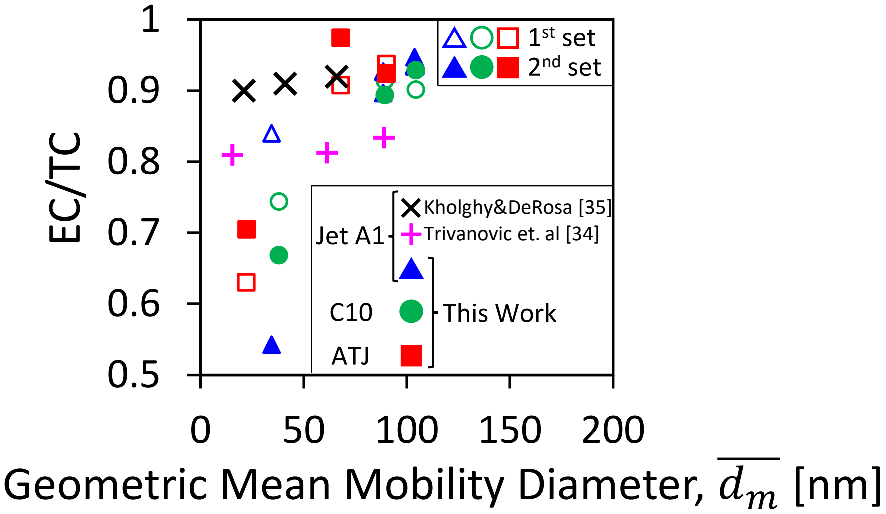

Figure 3.14: Elemental to total carbon ratio (EC/TC) as a function of the $\overline{d_m}$ for all fuels (Jet A1: blue triangles, C10: green circles, ATJ: red squares) and flame conditions in this work compared to those of previous work. The data points from left to right, for this work, correspond to 10/3.00, 12/2.50, and 12/2.00 flame conditions, respectively. Previous work by Kholghy & DeRosa and Trivanovic, Kelesidis, and Pratsinis is shown with black ×'s [35] and pink crosses, respectively [34]. This work shows EC/TC increases with a decrease in Reynolds number and an increase in burner equivalence ratio, for all fuels.

There are multiple data points in Figure 3.14 that have EC/TC < 0.8. Most of these points come from 10/3.00 flame conditions and are produced using the SAFs, C10 and ATJ (green circles and red squares, respectively).

The second filter sample collected from the Jet A1 10/3.00 resulted in an EC/TC = 0.54, about 0.3 lower than the first sample set. This was unexpected and more investigation is needed to explain why this measurement was not repeatable and much lower when compared to previous work with similar $\overline{d_m}$. The 10/3.00 flame was known to be the most inconsistent flame condition across all fuels, and larger differences in EC/TC measurements are also seen in the other fuels with the 10/3.00 flame condition. It is important to note, that for the Jet A1 10/3.00 flame, the particle concentration, in #/cm^3, measured by the SMPS while collecting soot on the TOA filter for the 2nd set was about half of the concentration measured during the 1st set. Filter collection times were identical and so the total mass of soot collected on the filter was about half as much for the 2nd set in this condition. This can be seen when comparing reported total mass concentrations on the thermograms in the supplementary material. A possible answer to the discrepancy here is that the TOA filters were underloaded and the EC/TC measurements have a large relative uncertainty due to a lack of sufficient soot concentration on the filter punch.

The split point is a parameter that can cause uncertainty in EC/TC measurements with the TOA process. The split point defines the time when all carbon measured before the split point is considered as OC, and carbon measured after the split point is considered EC. For this experiment, the split point was automatically calculated by the Sunset Laboratory OCEC Carbon Aerosol Analyzer. Further discussion on how this split point is chosen by the instrument is outlined in the supplementary material, Section A.7. With the understanding that the reported EC/TC ratios by the analyzer are sensitive and dependent to when the split point is taken, a simple sensitivity analysis on the EC/TC ratios was done with respect to the split point.

The vertical error bars in Figure 3.15 show the effect of adjusting the split point by ±10% of the difference between the split point and the time that the oxidizing phase in the analyzer begins. The oxidizing phase began at a time of 420 seconds and the split points ranged from 530 to 590 seconds across all the samples seen in Figure 3.15. For example, when checking the ±10% sensitivity, if a sample had a split point of 550 seconds, the error bars in Figure 3.15 would identify the range of EC/TC for a split point taken at 550±13 seconds. Otherwise, the symbols in Figure 3.15 identify the EC/TC ratio with the instrument calculated split point. For every case but one, the higher split point resulted in a lower EC/TC, and the lower split point resulted in a higher EC/TC. This is simply because the TOA process identifies carbon before the split point as OC and after the split point as EC. The single case where this was not true was the Jet A1 10/3.00 2nd set. This point is a visible outlier and future work will investigate why it has a different trend to all the other points with respect to split point sensitivity, as well as why it is about 0.3 different from the 1st measurement of the same flame condition. Otherwise, the 1st and 2nd sets of data are comparable within split point sensitivity ranges, and the 12/2.50 and 12/2.00 conditions show the best repeatability.

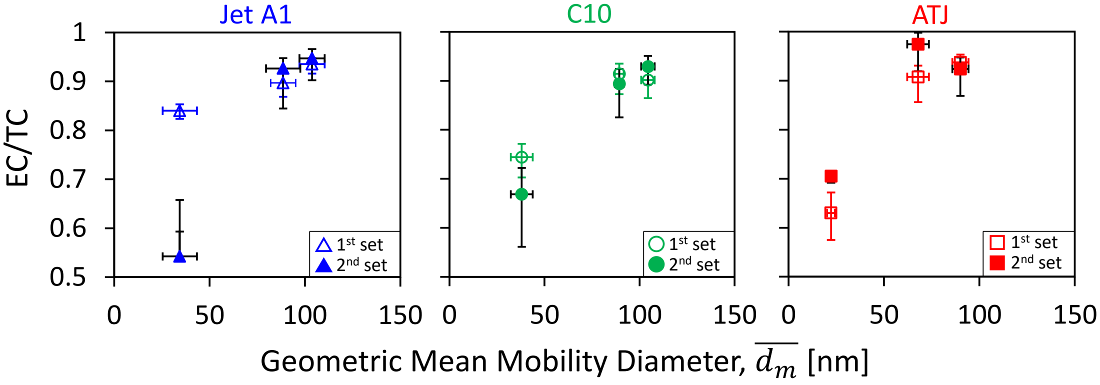

Figure 3.15: EC/TC ratios for three different fuels and three different flame conditions with two sets of measurements on separate days of testing. The average $\overline{d_m}$ for each flame condition remained the same for both sets of EC/TC measurements. Horizontal error bars identify the standard deviation of the $\overline{d_m}$ for each condition. Vertical error bars show the EC/TC sensitivity to split point in the TOA process.

For the C10 (green circles) and ATJ (red squares) flames, the EC/TC dropped non-linearly when $\overline{d_m} < 50$ nm. This was unexpected as the other flame conditions show similar trends to Jet A1 of this work and previous work. This work (excluding the outlier mentioned above) and previous work seem to show linear relations for $\overline{d_m}$ and EC/TC, however, this was not the case for the SAF fuels. This is a unique finding that could impact quantification of soot emissions from these fuels when using optical diagnostic techniques. Typical optical diagnostic techniques for measuring aircraft soot emissions, such as LII, can be sensitive to changes in EC/TC. For example, EC/TC directly affects the refractive index of soot and LII relies on an accurate refractive index user input to measure mass concentrations of soot. If the refractive index input for SAFs, like the ones tested in this experiment, is assumed to be similar to that of the higher EC/TC ratios measured for conventional fuels at $\overline{d_m} <$ 50 nm, the LII could be inadvertently underestimating total mass concentrations due to the discrepancy in soot EC/TC.

Chapter 4: Conclusion and Future Work

4.1 Concluding Remarks

A FSP burner was used to synthesize soot from Jet A1, C10, and ATJ liquid jet fuels at a variety of flame conditions with burner equivalence ratios in the range of 7-13 and Reynolds numbers from 6100-9100. Soot mobility size distributions, N_{tot}, d_m, and d_p were compared for all fuels and flame conditions. Jet A1 and C10 fuels produced similar $\overline{d_m}$ for each flame condition ranging from 34-104 nm, while ATJ produced significantly smaller (22-90 nm) agglomerates for the same flame conditions. Overall dilution ratios ranged from 12-32 across different test conditions and days, and N_{tot} was directly related but inversely proportional to the dilution ratios measured during each SMPS scan. However, the dilution ratios require further fine tuning and improvement in measurement to be reliable and consistent from day-to-day. The d_p for all conditions showed lognormal distributions, and $\overline{d_p}$ ranged from 11-21 nm, in good agreement with previous FSP work and meeting thresholds of jet engine field tests with $\overline{d_p} < 20$ nm. Compositions measured were reflective of jet engine field test results for high thrust loadings with EC/TC > 0.8 for 12/2.50 and 12/2.00 flame conditions with all fuels and showed excellent agreement with previous FSP studies. Day-to-day variations in size distributions and number concentrations still show unpredictability; however, trends for specific fuels and flame conditions were distinguishable. Agglomerate mobility diameters were repeatable within 20%, and d_p fit lognormal distributions.

This work has contributed to the field of in-situ soot sampling and measurement and lab-scale soot generating burners. The burner used to synthesize soot in this experiment was used in previous FSP literature and this work has confirmed similar findings where composition and size properties of FSP-made soot can meet the soot property thresholds of jet engine-like soot from full-scale turbofan engines operating on conventional fuels. However, this work also identifies unique findings in the way that the flame sampled here was left completely open to the ambient room, versus being fully enclosed by quartz tubes or in a fume hood. This work has also gone beyond the testing of conventional Jet A1 fuel and tested two SAFs, with different chemical compositions, to compare with Jet A1 results. The research and results outlined in this thesis will help advance the field of in-situ soot measurements, jet engine-like soot synthesis, and lab-scale soot generators as possible rapid screening devices which will directly improve opportunities for SAF testing and development.

4.2 Outlook

ICAO emissions standards for nvPM involve measurement of visible plumes to identify the smoke number [70]. Visible plumes are often generated when particles exceed d_m = 100 nm [70], but as discussed in this work, current jet engine soot emissions produce $\overline{d_m} <$ 70 nm, making smoke number a less accurate representation for the soot particles produced. Visible plumes continue to be reduced and test standards are evolving where the SAE AIR6241 [71] methodology for measuring black carbon mass emissions [72] could be used, which focuses more on particle morphology and optical properties, rather than analysis of visible plumes. This practice puts focus on electrical mobility diameters of nvPM, including soot. This could make small-scale soot generators, like the one used in this study, in higher demand to characterize emerging SAF nvPM due to the assembly's ability to produce a range of particle sizes within the threshold of measured experimental jet engine particulates.

The most evident uncontrollable with the current setup is the variation in dilution ratio from day-to-day and between tests. It was shown that dilution ratio directly affects N_{tot}, which indirectly affects d_m in some cases. The indirect effects are introduced by higher N_{tot} causing increased collision frequency and coagulation rates. The first step to improving the inconsistencies in the dilution ratio was identifying the unreliability in using compressed air from the central lab supply for second stage dilution, as discussed in Section 3.2.1. This has since been replaced with certified cylinder air with a CO_2 concentration of 0 ppm. Future testing and analysis on the dilution ratio with this change should be completed and comparisons with the results presented in this work should be done. After the dilution ratio is controllable and repeatable, mass and optical property measurements will be done to compare with previous FSP work and benchmark against jet engine field tests.

Recent work by Trivanovic, Kelesidis, and Pratsinis [34] has tested the results of enclosed flames with nitrogen dilution gas supplied to the flame enclosure column. Their work has produced similar soot size and composition compared to this work, but with much lower fuel flowrates (4.5 L/min of Jet A1). The setup for this work has since been modified to incorporate enclosed flame tests and initial tests have been successful. When the assembly is finalized, identical tests to the recent work will be performed and directly compared. If size distributions remain distinguishable and consistency improves, this will be desirable as less fuel is required for accurate characterizations.

List of References

[1] N. Takegawa, Y. Murashima, A. Fushimi, K. Misawa, Y. Fujitani, K. Saitoh, H. Sakurai, Characteristics of sub 10 nm particle emissions from in-use commercial aircraft observed at Narita International Airport, Atmos. Chem. Phys., 21 (2021) 1085-1104.

[2] Climate and Clean Air Coalition, Short-lived Climate Pollutants – Black Carbon, https://www.ccacoalition.org/en/slcps/black-carbon, Accessed: 2023-01-04.

[3] V. S. Narik, S. Szopa, B. Adhikary, P. Artaxo, T. Bernsten, W. D. Collins, S. Fuzzi, L. Gallardo, A. Kiendler Scharr, Z. Klimont, H. Liao, N. Unger, P. Zanis, Short-Lived Climate Forcers. In Climate Change 2021: The Physical Science Basis. Contribution of Working Group I to the Sixth Assessment Report of the Intergovernmental Panel on Climate Change; Cambridge University Press: New York, (2021)

[4] M. Kousoulidou, L. Lonza, European Aviation Environmental Report (2016).

[5] U. Schumann, On the Effect of Emissions from Aircraft Engines on the State of the Atmosphere, Annales Geophysicae 12 (1994) 365–384

[6] G. A. Kelesidis, D. Neubauer, L. Fan, U. Lohmann, S. E. Pratsinis, Enhanced Light Absorption and Radiative Forcing by Black Carbon Agglomerates, Env. Sci. Tech. 56 (2022) 12 8610-8618

[7] A. Baroutaji, et al., Aviation and Environment Report, Published by ICAO (2019).

[8] L. Zhang, T. Butler, B. Yang, Chapter 5: Recent Trends, Opportunities and Challenges of Sustainable Aviation Fuel, edited by A. A. Vertès, N. Qureshi, H. P. Blaschek, H. Yukawa, Published by Wiley (2020).

[9] C. Voigt, et al., Cleaner burning aviation fuels can reduce contrail cloudiness, Comm. Earth & Environ. 2 (2021) 114.

[10] J. Heyne, B. Rauch, P. Le Clercq, M. Colket, Sustainable aviation fuel prescreening tools and procedures, Fuel 290 (2021) 120004

[11] P. Oßwald, S. Richter, Report about the high temperature regime regarding auto- ignition, combustion and soot, JETSCREEN, (2019).

[12] Rauch B., JETSCREEN: JET fuel SCREENing and optimization 2020, https://cordis.europa.eu/project/id/723525, Accessed: 2023-01-04.

[13] Smoke, Dust and Haze, S.K. Friedlander, Oxford, 2nd edition (1977)

[14] G. A. Kelesidis, S. E. Pratsinis, Soot light absorption and refractive index during agglomeration and surface growth, P. Combust. Inst. 37 (2019) 1177-1184.

[15] P. Lobo, D. E. Hagen, P. D. Whitefield, Comparison of PM emissions from a commercial jet engine burning conventional, biomass, and Fischer-Tropsch Fuels, Env. Sci. Tech. 45 (2011) 10744-10749

[16] T. Schripp, F. Herrmann, P. Oßwald, M. Köhler, A. Zschocke, D. Weigelt, M. Mroch, C. Werner-Spatz, Particle emissions of two unblended alternative jet fuels in a full-scale jet engine, Fuel 256 (2019) 115903.

[17] L. Durdina, B. T. Brem, M. Elser, D. Schönenberger, F. Siegerist, J. G. Anet, Reduction of nonvolatile particulate matter emissions of a commercial turbofan engine at the ground level from the use of a sustainable aviation fuel blend, Env. Sci. Tech. 55 (2021) 21 14576-14585.

[18] M. Saffaripour, K. A. Thomson, G. J Smallwood, P. Lobo, A review on the morphological properties of non-volatile particulate matter emissions from aircraft turbine engines, J. Aerosol Sci. 139 (2020) 105467.

[19] C. C. Wey, B. E. Anderson, C. Wey, R. C. Miake-Lye, P. Whitefield, R. Howard, Overview on the Aircraft Particle Emissions Experiment, J. Propuls. Power, 23 (2007) 898-904.

[20] P. Lobo, D. Hagen, P. D. Whitefield, Comparison of PM emissions from a commercial jet engine burning conventional, biomass, and Fischer Tropsch fuels, Env. Sci. Tech. 45 (2011) 10744-10749.

[21] P. Lobo, J. Condevaux, Z. Yu, J. Kuhlmann, D. E. Hagen, R. C. Miake-Lye, P. D. Whitefield, D. W. Raper, Demonstration of a regulatory method for aircraft engine nonvolatile PM emissions measurements with conventional and isoparaffinic kerosene fuels, Energy Fuels, 30 (2016) 7770-7777.

[22] S. Christie, P. Lobo, D. Lee, D. Raper, Gas turbine engine nonvolatile particulate matter mass emissions: correlation with smoke number for conventional and alternative fuel blends, Env. Sci Tech. 51 (2017) 988-996.

[23] J.S. Kinsey et al., Assessment of a regulatory measurement system for the determination of the non-volatile particulate matter emissions from commercial aircraft engines, J. Aerosol Sci. 154 (2021) 105734.

[24] P. Lobo et al., Comparison of standardized sampling and measurement reference systems for aircraft engine non-volatile particulate matter emissions, J. Aerosol Sci. 145 (2020) 105557.

[25] M. M. Maricq, Coagulation dynamics of fractal-like soot aggregates, J. Aerosol Sci., 38 (2007) 141-156.

[26] B. Zhao, Z. Yang, J. Wang, M. V. Johnston, and H. Wang. Analysis of Soot Nanoparticles in a Laminar Premixed Ethylene Flame by Scanning Mobility Particle Sizer. Aerosol Sci. Tech. 37 (2003) 611-620

[27] M. Commodo, G. De Falco, A. Bruno, C. Borriello, P. Minutolo, and A. D’Anna. Physicochemical evolution of nascent soot particles in a laminar premixed flame: from nucleation to early growth. Combust. Flame, 162 (2015) 3854–3863.

[28] M. Kazemimanesh, A. Moallemi, J. S. Olfert, and L. W. Kostiuk. Probe sampling to map and characterize nanoparticles along the axis of a laminar methane jet diffusion flame. P. Combust. Inst. 36 (2017) 881-888.

[29] M. Kasper, K. Siegmann, K. Sattler, Evaluation of an in-situ Sampling Probe for its Accuracy in Determining Particle Size Distributions from Flames, J. Aerosol Sci. 28 (1997) 1569–1578.

[30] J. Dreyer, M. Poli, N. A. Eaves, M. L. Botero, J. Akroyd, S. Mosbach, M. Kraft, Evolution of the soot particle size distribution along the centreline of an n-heptane/toluene co-flow diffusion flame. Combust. Flame 209 (2019) 256-266.

[31] C. M. Heath, Design and Analysis of an Isokinetic Sampling Probe for Submicron Particle Measurements at High Altitude. NASA STI Program (2012).

[32] Y.R. Tan, M. Salamanca, L. Pascazio, J. Akroyd, M. Kraft, The effect of poly(oxymethylene) dimethyl ethers (PODE3) on soot formation in ethylene/PODE3 laminar coflow diffusion flames, Fuel 283 (2021) 118769.

[33] E. Goudeli, A. Gröhn, S. Pratsinis, Sampling and dilution of nanoparticles at high temperature, Aerosol Sci. Tech. 50 (2016) 591-604.

[34] U. Trivanovic, G. A. Kelesidis, S. E. Pratsinis, High Throughput Generation of Aircraft-like Soot, Aerosol Sci. Tech., (2022).

[35] M. Kholghy, V. DeRosa, Morphology, composition and optical properties of jet engine-like soot made by a spray flame, Combust. Flame 231 (2021) 111480.

[36] M. Saffaripour, K. A. Thomson, G. J. Smallwood, P. Lobo, A review on the morphological properties of non-volatile particulate matter emissions from aircraft turbine engines, J. Aerosol Sci. 139 (2020) 105467.

[37] L. Durdina, P. Lobo, M. B. Trueblood, E. A. Black, S. Achterberg, D. E. Hagen, B. T. Brem, J. Wang, Response of real-time black carbon mass instruments to mini-CAST soot, Aerosol Sci. Tech. 50 (2016) 906-918.

[38] M. Kazemimanesh, A. Moallemi, K. Thomson, G. Smallwood, P. Lobo, J. S. Olfert, A novel miniature inverted-flame burner for the generation of soot nanoparticles. Aerosol Sci. Tech. 53 (2019) 184–195.

[39] A. Moallemi, M. Kazemimanesh, J. C. Corbin, K. Thomson, G. Smallwood, J. S. Olfert, P. Lobo, Characterization of black carbon particles generated by a propane-fueled miniature inverted soot generator, J. Aerosol Sci. 135 (2019) 46-57.

[40] R. Ghazi, H. Tjong, A. Soewono, S. N. Rogak, J.S. Olfert, Mass, mobility, volatility, and morphology of soot particles generated by a mckenna and inverted burner. Aerosol Sci. Tech. 47 (2013) 395–405.

[41] J.S. Kinsey, R. Giannelli, R. Howard, B. Hoffman, R. Frazee, M. Aldridge, C. Leggett, K. Stevens, D. Kittelson, W. Silvis, Assessment of a regulatory measurement system for the determination of the non-volatile particulate matter emissions from commercial aircraft engines, J. Aerosol Sci. 154 (2021) 105734.

[42] M. Abegglen, L. Durdina, B. Brem, J. Wang, T. Rindlisbacher, J. Corbin, U. Lohmann, B. Sierau, Effective density and mass–mobility exponents of particulate matter in aircraft turbine exhaust: dependence on engine thrust and particle size, J. Aerosol Sci. 88 (2015) 135–147.

[43] M. Elser, B.T. Brem, L. Durdina, D. Schönenberger, F. Siegerist, A. Fischer, J. Wang, Chemical composition and radiative properties of nascent particulate matter emitted by an aircraft turbofan burning conventional and alternative fuels, Atmospheric Chem. Phys. 19 (2019) 6809–6820.

[44] L. Durdina, P. Lobo, M. B. Trueblood, E. A. Black, S. Achterberg, D. E. Hagen, B. T. Brem, J. Wang, Response of real-time black carbon mass instruments to mini-CAST soot, Aerosol Sci. Tech. 50 (2016) 906.

[45] M. Kazemimanesh, A. Moallemi, K. Thomson, G. Smallwood, P. Lobo, J. S. Olfert, A novel miniature inverted-flame burner for the generation of soot nanoparticles, Aerosol Sci. Tech. 53 (2019) 184-195.

[46] R. Ghazi, H. Tjong, A. Soewono, S.N. Rogak, J.S. Olfert, Mass-Mobility measurements using a centrifugal particle mass analyzer and differential mobility spectrometer, Aerosol Sci. Tech. 47 (2013) 395.

[47] B. Tian, A. Liu, C. T. Chong, L. Fan, S.Ni, A. Hull, And. Hull, Ang. Hull, S. Rigopoulos, K. H. Luo, S. Hochgreb, Measurement and simulation of sooting characteristics by an ATJ-SKA biojet fuel and blends with Jet A-1 fuel in laminar non-premixed flames, Combust. Flame 233 (2021) 111582.

[48] L. Mädler, H. K. Kammler, R. Mueller, S. E. Pratsinis, Controlled Synthesis of nanostructured particles by flame spray pyrolysis, J. Aerosol Sci. 33 (2002) 369-389.

[49] R. Strobel, S.E. Pratsinis, Flame aerosol synthesis of smart nanostructured materials, J. Material Chem. 17 (2007) 4743-4756.

[50] F. O. Ernest, R. Bütchel, R. Strobel, S. E. Pratsinis, One-Step Flame-Synthesis of Carbon-embedded and -Supported Platinum Clusters, Chem. Materials 20 (2008) 2117-2123.

[51] T. J. Patey, R. Büchel, S. H. ng, F. Krumeich, S. E. Pratsinis, P. Novàk, Flame co-synthesis of $LiMn_2O_4$ and carbon nanocomposites for high power batteries, J. Power Sources 189 (2009) 149-154.

[52] M. C. Heine, L. Mädler, R. Jossen, S.E. Pratsinis, Direct measurement of entrainment during nanoparticle synthesis in spray flames, Combust. Flame 144 (2006) 809-820.

[53] K. Wegner, Original Operating Instructions Lab-scale Flame Spray Reactor Version 2.20, (2020).

[54] T. Chan, P. Canteenwalla, W. Chishty, Characterization of fuel composition and altitude impact on gaseous and particle emissions from a turbojet engine. Proc. ASME Turbo Expo, (2017).

[55] R. Xu, H. Wang, M. Colket, T. Edwards, Thermochemical Properties of Jet Fuels, National Jet Fuels Combustion Program, (2015).

[56] T. Edwards, Reference Jet Fuels for Combustion Testing, AIAA SciTech Forum, (2017).

[57] J. Lasheras, E. Villermaux, E. Hopfinger, Break-up and atomization of a round water jet by a high-speed annular air jet, J. of Fluid Mech. 357 (1998) 351-379

[58] J. C. Lasheras, E. Villermaux, E. J. Hopfinger, Break-up and atomization of a round water jet by a high-speed annular air jet, J. Fluid Mech. 357 (1998) 351-379.

[59] Gilibrator-2 Calibrator: Sensidyne, Sensidyne Industrial Health and Safety, 2022, https://www.sensidyne.com/air-sampling-equipment/calibration-equipment/gilibrator-2/.

[60] General Scanning Mobility Particle Sizer (SMPS) 3938. TSI, https://tsi.com/products/particle-sizers/scanning-mobility-particle-sizer-spectrometers/general-scanning-mobility-particle-sizer-(smps)-3938/.

[61] R. L. Vander Wal, K. J. Weiland, Laser-induced incandescence: Development and characterization towards a measurement of soot-volume fraction, App. Phys. B 59 (1994) 445-452.

[62] D. R. Chen, D. Y. H. Pui, D. Hummes, H. Fissan, F. R. Quant, G. J. Sem, Design and evaluation of a nanometer aerosol differential mobility analyzer (Nano-DMA), J. Aerosol Sci. 29 (1998) 497–509.

[63] R. C. Flagan, Electrical Techniques, in Aerosol Measurement: Principles, Techniques, and Applications, edited by P. A. Baron and K. Willeke, Published by Wiley (2001) 537–568.

[64] P. F. DeCarlo, J. G. Slowik, D. R. Worsnop, P. Davidotis, J. L. JimenezParticle morphology and density characterization by combined mobility and aerodynamic diameter measurements. Part 1: Theory, Aer. Sci. Tech. 38 (2004) 1185-1205.

[65] B. R. Stanmore, J. F. Brilhac, P. Gilot, The oxidation of soot: A review of experiments, mechanisms and models, Carbon 39 (2001) 2247-2268.

[66] S. G. Jennings, The mean free path of air, J. Aerosol Sci. 19 (1986) 159-166.

[67] E. Goudeli, M. L. Eggersdorfer, S. E. Pratsinis, Coagulation-agglomeration of fractal-like particles: Structure and self-preserving size distribution. Langmuir 31 (2015) 1320.

[68] M. Saffaripour, K. A. Thomson, G. J. Smallwood, P. Lobo, A review on the morphological properties of non-volatile particulate matter emissions from aircraft turbine engines, J. Aerosol Sci. 139 (2020) 105467.

[69] G. A. Kelesidis, E. Goudeli, S. A. Pratsinis, Morphology and mobility diameter of carbonaceous aerosols during agglomeration and surface growth, Carbon 121 (2017) 527-535.

[70] International Civil Aviation Organization (ICAO), Annex 16 Environmental Protection – Volume II Aircraft Engine Emissions 3rd Ed., (2008).

[71] Society of Automotive Engineers (SAE) Procedure for the continuous sampling and measurement of non- volatile particle emissions from aircraft turbine engines AIR6241, Published by SAE International (2013).

[72] International Civil Aviation Organization – Committee on Aviation Environmental Protection (CAEP), https://www.icao.int/environmental-protection/pages/caep.aspx, Accessed: 2023-01-04.

Appendices

Appendix A - Supplementary Materials

A.1 Sampling Probe Engineering Drawing

The sampling probe was designed and manufactured in collaboration with Swagelock and the Carleton University machine shop. The engineering drawing in Figure A1 is the final design, manufactured and delivered from Swagelock. Minor modifications were done on the inlet tip (located at bubble 7), to ensure proper sealing around the fittings and positioning of the inner tube. These modifications were completed with the help of the Carleton machine shop and their technicians.

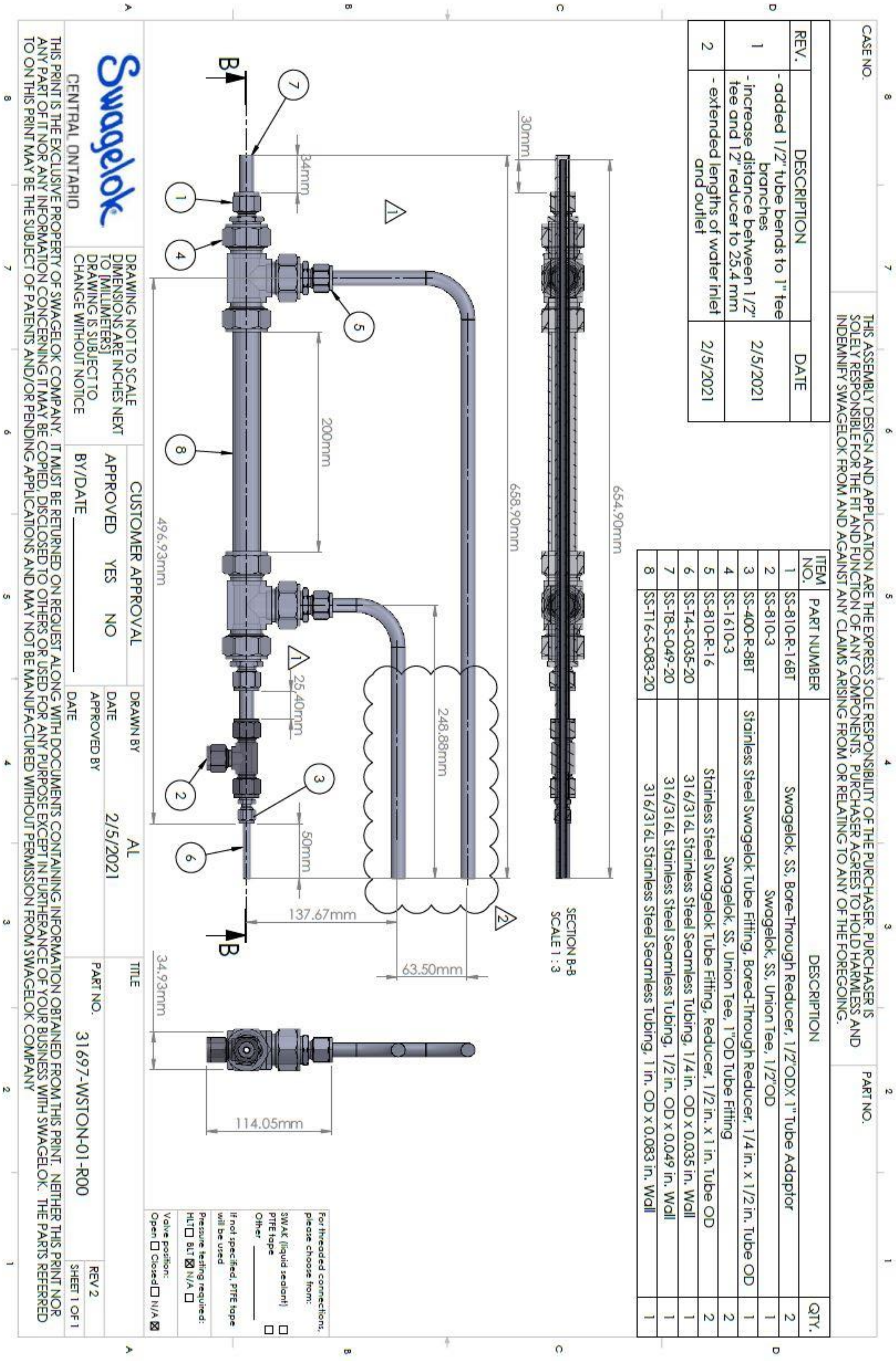

THIS ASSEMBLY DESIGN AND APPLICATION ARE THE EXPRESS SOLE RESPONSIBILITY OF THE PURCHASER. PURCHASER IS SOLELY RESPONSIBLE FOR THE FIT AND FUNCTION OF ANY COMPONENTS. PURCHASER AGREES TO HOLD HARMLESS AND INDEMNIFY SWAGELOK FROM AND AGAINST ANY CLAIMS ARISING FROM OR RELATING TO ANY OF THE FOREGOING.

REV.	DESCRIPTION	DATE
1	- added 1/2" tube bends to 1" tee branches - increase distance between 1/2" tee and 12" reducer to 25.4 mm	2/5/2021
2	- extended lengths of water inlet and outlet	2/5/2021

ITEM NO.	PART NUMBER	DESCRIPTION	QTY.
1	SS-810-R-16BT	Swagelok, SS, Bore-Through Reducer, 1/2"ODX 1" Tube Adaptor	2
2	SS-810-3	Swagelok, SS, Union Tee, 1/2"OD	1
3	SS-400-R-8BT	Stainless Steel Swagelok Tube Fitting, Bored-Through Reducer, 1/4 in. x 1/2 in. Tube OD	1
4	SS-1610-3	Swagelok, SS, Union Tee, 1"OD Tube Fitting	2
5	SS-810-R-16	Stainless Steel Swagelok Tube Fitting, Reducer, 1/2 in. x 1 in. Tube OD	2
6	SS-T4-S-035-20	316/316L Stainless Steel Seamless Tubing, 1/4 in. OD x 0.035 in. Wall	1
7	SS-T8-S-049-20	316/316L Stainless Steel Seamless Tubing, 1/2 in. OD x 0.049 in. Wall	1
8	SS-T16-S-083-20	316/316L Stainless Steel Seamless Tubing, 1 in. OD x 0.083 in. Wall	1

For threaded connections, please choose from:
SWAK (liquid sealant) ☐
PTFE tape ☐
Other ____
If not specified, PTFE tape will be used

Pressure testing required:
HLT ☐ BLT ☒ N/A ☐

Valve position:
Open ☐ Closed ☐ N/A ☒

DRAWING NOT TO SCALE
DIMENSIONS ARE INCHES NEXT TO [MILLIMETERS]
DRAWING IS SUBJECT TO CHANGE WITHOUT NOTICE

CUSTOMER APPROVAL
APPROVED YES NO
BY/DATE ____

DRAWN BY AL
DATE 2/5/2021
APPROVED BY
DATE

TITLE
PART NO. 31697-WSTON-01-R00
REV 2
SHEET 1 OF 1

THIS PRINT IS THE EXCLUSIVE PROPERTY OF SWAGELOK COMPANY. IT MUST BE RETURNED ON REQUEST ALONG WITH DOCUMENTS CONTAINING INFORMATION OBTAINED FROM THIS PRINT. NEITHER THIS PRINT NOR ANY PART OF IT NOR ANY INFORMATION CONCERNING IT MAY BE COPIED, DISCLOSED TO OTHERS OR USED FOR ANY PURPOSE EXCEPT IN FURTHERANCE OF YOUR BUSINESS WITH SWAGELOK. THE PARTS REFERRED TO ON THIS PRINT MAY BE THE SUBJECT OF PATENTS AND/OR PENDING APPLICATIONS AND MAY NOT BE MANUFACTURED WITHOUT PERMISSION FROM SWAGELOK COMPANY

Figure A1: Finalized Swagelock engineering drawing of the sampling probe design with water-cooling and N_2 dilution. This drawing includes all part numbers, dimensions, and revisions made.

A.2 CO_2 Concentration at Various Burner Stages

Figure A2 illustrates a profile of the CO_2 concentrations measured after both stages of dilution throughout a start-up to shutdown process. With the pilot flame running, Figure A2 shows how the CO_2 content changes as a Jet A1 flame is initiated and operates for a short period of time, before shutting off Jet A1 flow, and then shutting off the premixed methane-oxygen pilot fuel. The CO_2 concentration eventually returns to an ambient condition, around 450 ppm.

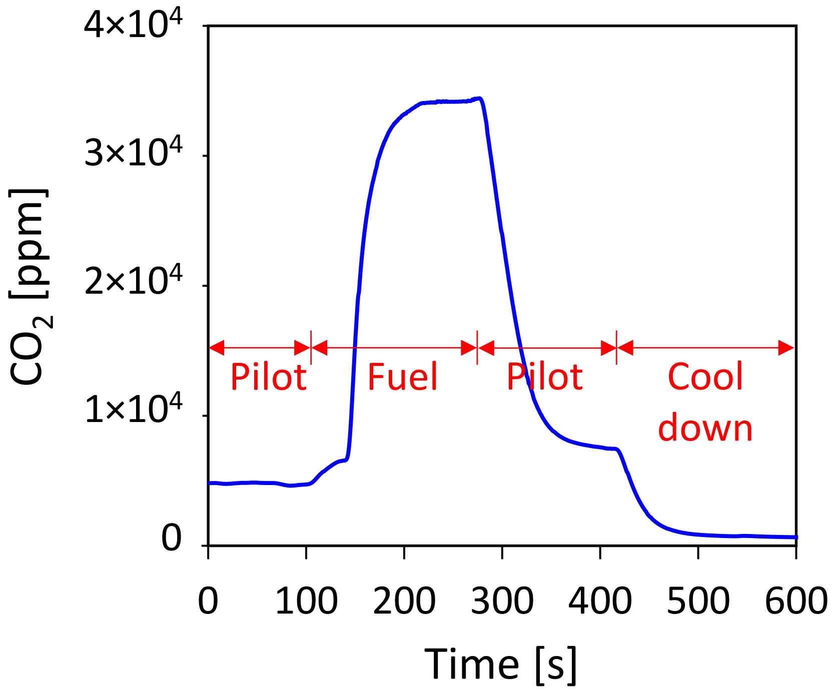

Figure A2: CO_2 concentrations after two stage dilution by the sampling probe and Dekati diluter at various burner operation stages. The stages from left to right are the premixed methane-oxygen pilot flame, followed by a Jet A1 flame, then back to the pilot flame, and ending with the burner shut off and cooling down where the CO_2 concentration tapers down to ambient room conditions.

A.3 Fuel Composition Breakdown [54]

Table A.1: Chemical Composition for Jet A1 (POSF 10325)

Hydrogen content (weight %)	14.0	
Average Molecular Wt (g/mole)	159	
Average Molecular Formula	$C_{11.4}H_{22.1}$	
	Weight %	**Volume %**
Aromatics		
Alkylbenzenes		
benzene (C06)	0.01	0.01
toluene (C07)	0.16	0.14
C2-benzene (C08)	1.10	1.00
C3-benzene (C09)	2.97	2.73
C4-benzene (C10)	3.32	3.05
C5-benzene (C11)	2.22	2.03
C6-benzene (C12)	1.45	1.33
C7-benzene (C13)	0.73	0.67
C8-benzene (C14)	0.52	0.48
C9-benzene (C15)	0.28	0.25
C10+-benzene (C16+)	0.15	0.14
Total Alkylbenzenes	**12.90**	11.84
Diaromatics (Naphthalenes, Biphenyls, etc.)		
diaromatic-C10	0.22	0.17
diaromatic-C11	0.66	0.51
diaromatic-C12	0.86	0.68
diaromatic-C13	0.43	0.34
diaromatic-C14+	0.17	0.14
Total Alkylnaphthalenes	**2.34**	1.84
Cycloaromatics (Indans, Tetralins,etc.)		
cycloaromatic-C09	0.02	0.02
cycloaromatic-C10	0.26	0.21
cycloaromatic-C11	0.66	0.56
cycloaromatic-C12	0.89	0.76
cycloaromatic-C13	0.85	0.73
cycloaromatic-C14	0.44	0.38
cycloaromatics-C15+	0.17	0.15
Total Cycloaromatics	**3.29**	2.81

Total Aromatics	**18.53**	**16.49**
Paraffins		
iso-Paraffins		
C07 & lower -isoparaffins	0.15	0.18
C08-isoparaffins	0.44	0.50
C09-isoparaffins	1.05	1.17
C10-isoparaffins	4.20	4.57
C11-isoparaffins	5.70	6.08
C12-isoparaffins	5.63	6.02
C13-isoparaffins	4.22	4.41
C14-isoparaffins	4.20	4.35
C15-isoparaffins	2.51	2.59
C16-isoparaffins	1.00	1.03
C17-isoparaffins	0.39	0.40
C18-isoparaffins	0.11	0.11
C19-isoparaffins	0.03	0.03
C20-isoparaffins	0.03	0.03
C21-isoparaffins	<0.01	<0.01
C22-isoparaffins	<0.01	<0.01
C23-isoparaffins	<0.01	<0.01
C24-isoparaffins	<0.01	<0.01
Total iso-Paraffins	**29.69**	31.46
n-Paraffins		
n-C07 & lower	0.17	0.20
n-C08	0.54	0.61
n-C09	1.42	1.57
n-C10	3.26	3.53
n-C11	4.29	4.58
n-C12	3.74	3.94
n-C13	2.80	2.93
n-C14	2.02	2.09
n-C15	1.03	1.06
n-C16	0.43	0.44
n-C17	0.21	0.22
n-C18	0.05	0.05
n-C19	0.01	0.01
n-C20	<0.01	<0.01
n-C21	<0.01	<0.01
n-C22	<0.01	<0.01

n-C23	<0.01	<0.01
Total n-Paraffins	**19.98**	21.23
Cycloparaffins		
Monocycloparaffins		
C07 & lower monocycloparaffins	0.36	0.37
C08-monocyclocycloparaffins	0.78	0.78
C09-monocyclocycloparaffins	2.30	2.29
C10-monocyclocycloparaffins	4.11	3.97
C11-monocyclocycloparaffins	5.43	5.38
C12-monocyclocycloparaffins	3.73	3.68
C13-monocyclocycloparaffins	4.19	4.09
C14-monocyclocycloparaffins	2.19	2.14
C15-monocyclocycloparaffins	1.33	1.29
C16-monocyclocycloparaffins	0.42	0.41
C17-monocyclocycloparaffins	0.18	0.18
C18-monocyclocycloparaffins	0.04	0.04
C19+-monocyclocycloparaffins	0.02	0.02
Total Monocycloparaffins	**25.08**	24.64
Dicycloparaffins		
C08-dicycloparaffins	0.03	0.03
C09-dicycloparaffins	0.43	0.39
C10-dicycloparaffins	0.72	0.63
C11-dicycloparaffins	1.52	1.41
C12-dicycloparaffins	1.57	1.47
C13-dicycloparaffins	1.21	1.12
C14-dicycloparaffins	0.81	0.76
C15-dicycloparaffins	0.20	0.19
C16-dicycloparaffins	0.04	0.04
C17+-dicycloparaffins	0.02	0.02
Total Dicycloparaffins	**6.56**	6.06
Tricycloparaffins		
C10-tricycloparaffins	<0.01	<0.01
C11-tricycloparaffins	0.16	0.13
C12-tricycloparaffins	<0.01	<0.01
Total Tricycloparaffins	**0.16**	0.13
Total Cycloparaffins	**31.79**	30.83

Table A.2: Chemical Composition for C10 (POSF 12345)

Hydrogen content (weight %)	13.9	
Average Molecular Wt (g/mole)	135	
Average Molecular Formula	$C_{9.7}H_{18.7}$	
	Weight %	**Volume %**
Aromatics		
Alkylbenzenes		
benzene (C06)	<0.01	<0.01
toluene (C07)	<0.01	<0.01
C2-benzene (C08)	0.02	0.01
C3-benzene (C09)	30.66	27.21
C4-benzene (C10)	<0.01	<0.01
C5-benzene (C11)	<0.01	<0.01
C6-benzene (C12)	<0.01	<0.01
C7-benzene (C13)	<0.01	<0.01
C8-benzene (C14)	<0.01	<0.01
C9-benzene (C15)	<0.01	<0.01
C10+-benzene (C16+)	<0.01	<0.01
Total Alkylbenzenes	**30.68**	27.22
Diaromatics (Naphthalenes, Biphenyls, etc.)		
diaromatic-C10	<0.01	<0.01
diaromatic-C11	<0.01	<0.01
diaromatic-C12	<0.01	<0.01
diaromatic-C13	<0.01	<0.01
diaromatic-C14+	<0.01	<0.01
Total Alkylnaphthalenes	**<0.01**	<0.01
Cycloaromatics (Indans, Tetralins,etc.)		
cycloaromatic-C09	<0.01	<0.01
cycloaromatic-C10	<0.01	<0.01
cycloaromatic-C11	<0.01	<0.01
cycloaromatic-C12	<0.01	<0.01
cycloaromatic-C13	<0.01	<0.01
cycloaromatic-C14	<0.01	<0.01
cycloaromatics-C15+	<0.01	<0.01
Total Cycloaromatics	**<0.01**	<0.01
Total Aromatics	**30.68**	**27.23**

Paraffins		
iso-Paraffins		
C07 & lower -isoparaffins	0.14	0.16
C08-isoparaffins	0.16	0.18
C09-isoparaffins	0.23	0.25
C10-isoparaffins	42.44	44.72
C11-isoparaffins	8.52	8.78
C12-isoparaffins	0.07	0.08
C13-isoparaffins	<0.01	<0.01
C14-isoparaffins	<0.01	<0.01
C15-isoparaffins	<0.01	<0.01
C16-isoparaffins	<0.01	<0.01
C17-isoparaffins	<0.01	<0.01
C18-isoparaffins	<0.01	<0.01
C19-isoparaffins	<0.01	<0.01
C20-isoparaffins	<0.01	<0.01
C21-isoparaffins	<0.01	<0.01
C22-isoparaffins	<0.01	<0.01
C23-isoparaffins	<0.01	<0.01
C24-isoparaffins	<0.01	<0.01
Total iso-Paraffins	**51.58**	54.18
n-Paraffins		
n-C07 & lower	0.04	<0.01
n-C08	0.20	0.22
n-C09	0.06	0.06
n-C10	17.33	18.16
n-C11	<0.01	<0.01
n-C12	0.03	0.03
n-C13	<0.01	<0.01
n-C14	<0.01	<0.01
n-C15	<0.01	<0.01
n-C16	<0.01	<0.01
n-C17	<0.01	<0.01
n-C18	<0.01	<0.01
n-C19	<0.01	<0.01
n-C20	<0.01	<0.01
n-C21	<0.01	<0.01
n-C22	<0.01	<0.01
n-C23	<0.01	<0.01

Total n-Paraffins	**17.66**	18.52
Cycloparaffins		
Monocycloparaffins		
C07 & lower monocycloparaffins	<0.01	<0.01
C08-monocyclocycloparaffins	<0.01	<0.01
C09-monocyclocycloparaffins	<0.01	<0.01
C10-monocyclocycloparaffins	0.03	0.03
C11-monocyclocycloparaffins	<0.01	<0.01
C12-monocyclocycloparaffins	<0.01	<0.01
C13-monocyclocycloparaffins	<0.01	<0.01
C14-monocyclocycloparaffins	<0.01	<0.01
C15-monocyclocycloparaffins	<0.01	<0.01
C16-monocyclocycloparaffins	<0.01	<0.01
C17-monocyclocycloparaffins	<0.01	<0.01
C18-monocyclocycloparaffins	<0.01	<0.01
C19+-monocyclocycloparaffins	<0.01	<0.01
Total Monocycloparaffins	**0.04**	0.04
Dicycloparaffins		
C08-dicycloparaffins	<0.01	<0.01
C09-dicycloparaffins	<0.01	<0.01
C10-dicycloparaffins	0.03	0.02
C11-dicycloparaffins	<0.01	<0.01
C12-dicycloparaffins	<0.01	<0.01
C13-dicycloparaffins	<0.01	<0.01
C14-dicycloparaffins	<0.01	<0.01
C15-dicycloparaffins	<0.01	<0.01
C16-dicycloparaffins	<0.01	<0.01
C17+-dicycloparaffins	<0.01	<0.01
Total Dicycloparaffins	**0.03**	0.03
Tricycloparaffins		
C10-tricycloparaffins	<0.01	<0.01
C11-tricycloparaffins	<0.01	<0.01
C12-tricycloparaffins	<0.01	<0.01
Total Tricycloparaffins	**<0.01**	<0.01
Total Cycloparaffins	**0.07**	0.07

Table A.3: Chemical Composition for ATJ (POSF 11498)

Hydrogen content (weight %)	15.3
Average Molecular Wt (g/mole)	178
Average Molecular Formula	$C_{12.6}H_{27.2}$
Aromatics	**Weight %**
Alkylbenzenes	
benzene (C06)	<0.01
toluene (C07)	<0.01
C2-benzene (C08)	<0.01
C3-benzene (C09)	<0.01
C4-benzene (C10)	<0.01
C5-benzene (C11)	<0.01
C6-benzene (C12)	<0.01
C7-benzene (C13)	<0.01
C8-benzene (C14)	<0.01
C9-benzene (C15)	<0.01
C10+-benzene (C16+)	<0.01
Total Alkylbenzenes	**<0.01**
Diaromatics (Naphthalenes, Biphenyls, etc.)	
diaromatic-C10	<0.01
diaromatic-C11	<0.01
diaromatic-C12	<0.01
diaromatic-C13	<0.01
diaromatic-C14+	<0.01
Total Alkylnaphthalenes	**<0.01**
Cycloaromatics (Indans, Tetralins,etc.)	
cycloaromatic-C09	<0.01
cycloaromatic-C10	<0.01
cycloaromatic-C11	<0.01
cycloaromatic-C12	<0.01
cycloaromatic-C13	<0.01
cycloaromatic-C14	<0.01
cycloaromatics-C15+	<0.01
Total Cycloaromatics	**<0.01**

Total Aromatics	**<0.01**
Paraffins	
iso-Paraffins	
C07 and lower-iso	0.02
C08-isoparaffins	0.61
C09-isoparaffins	0.17
C10-isoparaffins	0.22
C11-isoparaffins	0.52
C12-isoparaffins	78.26
C13-isoparaffins	1.23
C14-isoparaffins	0.53
C15-isoparaffins	<0.01
C16-isoparaffins	16.25
C17-isoparaffins	<0.01
C18-isoparaffins	<0.01
C19-isoparaffins	<0.01
C20-isoparaffins	1.69
C24-isoparaffins	0.12
Total iso-Paraffins	**99.62**
n-Paraffins	
n-C07	<0.01
n-C08	<0.01
n-C09	<0.01
n-C10	<0.01
n-C11	<0.01
n-C12	<0.01
n-C13	<0.01
n-C14	<0.01
n-C15	<0.01
n-C16	<0.01
n-C17	<0.01
n-C18	<0.01
n-C19	<0.01
n-C20	<0.01
Total n-Paraffins	**<0.01**
Cycloparaffins	
Monocycloparaffins	

C07-monocyclocycloparaffins	<0.01
C08-monocyclocycloparaffins	<0.01
C09-monocyclocycloparaffins	<0.01
C10-monocyclocycloparaffins	0.01
C11-monocyclocycloparaffins	<0.01
C12-monocyclocycloparaffins	<0.01
C13-monocyclocycloparaffins	<0.01
C14-monocyclocycloparaffins	<0.01
C15-monocyclocycloparaffins	<0.01
C16-monocyclocycloparaffins	<0.01
C17-monocyclocycloparaffins	<0.01
C18-monocyclocycloparaffins	<0.01
C19+-monocyclocycloparaffins	<0.01
Total Monocycloparaffins	**0.04**
Dicycloparaffins	
C08-dicycloparaffins	<0.01
C09-dicycloparaffins	<0.01
C10-dicycloparaffins	<0.01
C11-dicycloparaffins	<0.01
C12-dicycloparaffins	<0.01
C13-dicycloparaffins	<0.01
C14-dicycloparaffins	<0.01
C15-dicycloparaffins	<0.01
C16-dicycloparaffins	<0.01
C17+-dicycloparaffins	<0.01
Total Dicycloparaffins	**0.01**
Tricycloparaffins	
C10-tricycloparaffins	<0.01
C11-tricycloparaffins	<0.01
C12-tricycloparaffins	<0.01
Total Tricycloparaffins	**<0.01**
Total Cycloparaffins	**0.05**
Alkenes	
C12-alkene	0.08
C16-alkene	0.24
Total Alkenes	**0.32**

A.4 Open vs. Closed Flame

Figure A3 shows the FSP operating with no quartz tube around the base of the flame. The flame shown here is a Jet A1 12/2.00 flame and the camera settings are noted in the figure caption.

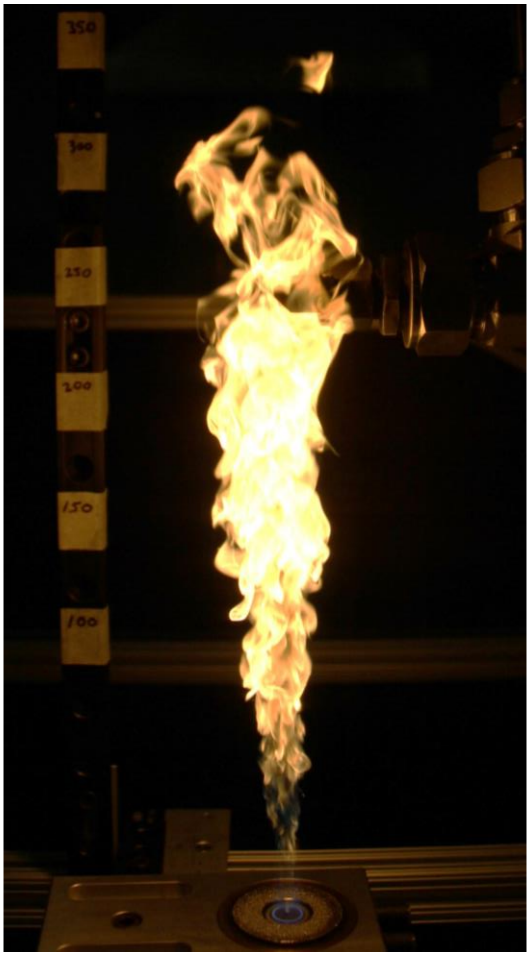

Figure A3: Flame spray pyrolysis with 12 mL/min of jet A1 fuel and 2.00 L/min of dispersion oxygen. Camera settings are as follows, exposure time: 1/8000 sec., ISO: 500, and aperture: *f*/3.6.

During the early tests of the FSP assembly, the flame remained completely open with no quartz tube placed around the base of the flame, on the burner surface. Initial tests results were producing size distributions with little to no order, and expected lognormal distributions were indistinguishable, especially for flame conditions with leaner mixtures (e.g., 10/3.00 condition). A quartz tube surrounding the base of the flame (100 mm in height) was proposed to limit the amount of entrained air caused by the highly turbulent flames, and in turn, reduce oxidation rates, to produce soot with larger size and concentrations. Figure S4 identifies an example of this with a 10/3.00 flame condition. The dark blue solid line is a 10/3.00 Jet A1 size distribution whilst having the 100 mm quartz tube around the base of the flame, while the light blue dashed line has identical flame and sampling conditions, but the quartz tube was removed from the surface of the burner.

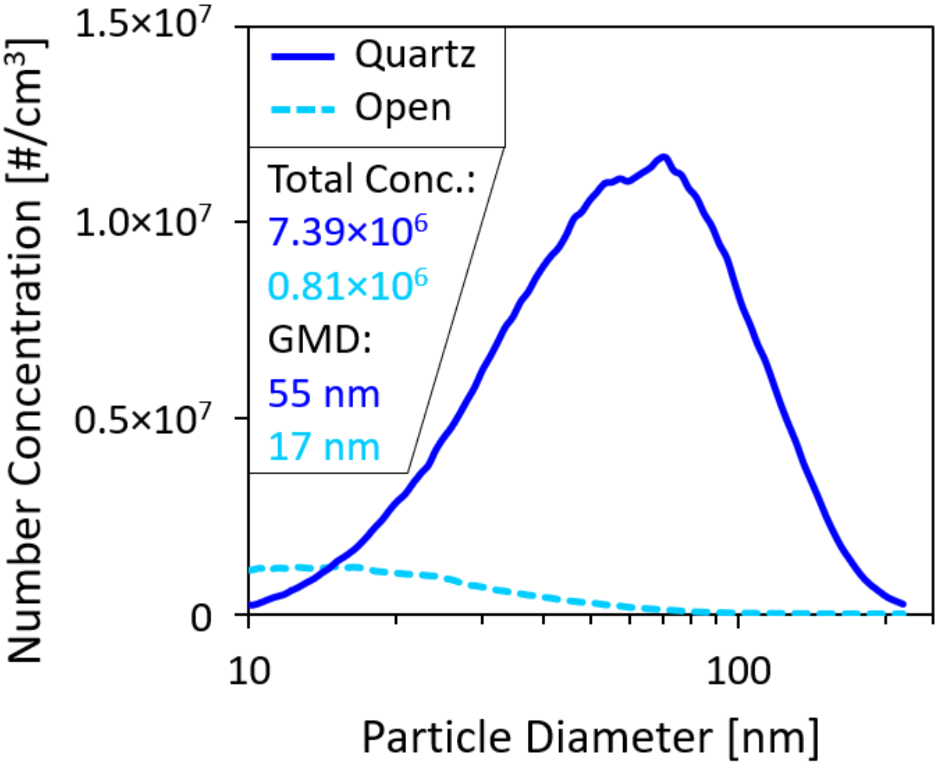

Figure A4: Particle size distributions for a Jet A1, 10/3.00 flame. The dark blue solid line shows the distribution collected when a quartz glass tube was placed on the surface of the burner with a height of 100 mm, inner diameter of 42 mm, and outer diameter of 46 mm. The light blue dashed line shows the distribution collected with the same 10/3.00 conditions and dilution ratio in the sampling line, but with the quartz tube removed from the burner.

Figure S4 plots are directly from the Aerosol Instrument Manager (AIM) software, which was used to operate the SMPS. These are small bin bar graphs and show the difference in smoothness of sample collection with or without the quartz tube. Notice the change in magnitude for the y-axis, and the increase in N_{tot} and $\overline{d_m}$ when the quartz tube is added.

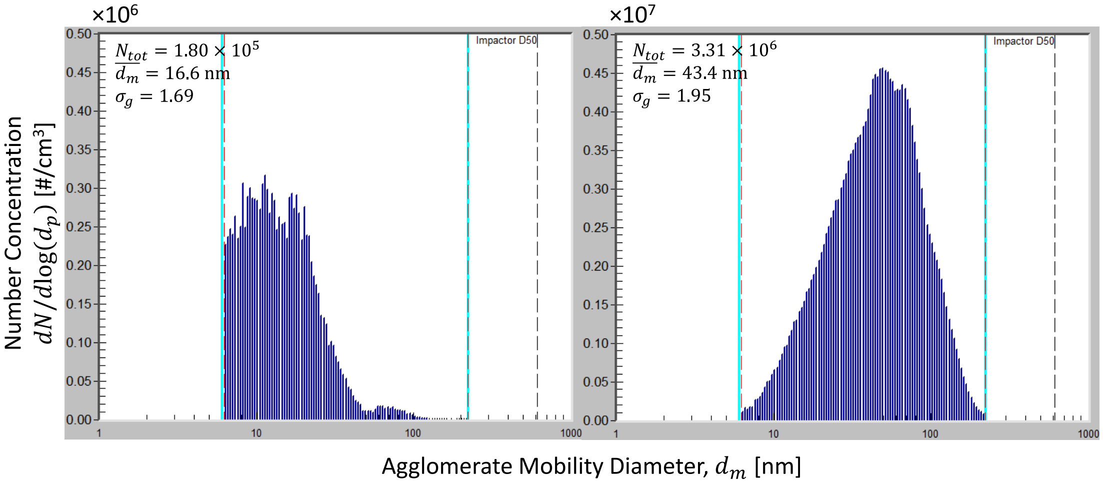

Figure A5: Mobility size distributions from AIM software for a Jet A1 10/3.00 flame condition with (left) and without (right) the 100 mm tall quartz tube placed around the base of the flame. All flame and sampling conditions for these distributions were identical, apart from removing the quartz tube.

A.5 Flame Imaging Procedure

How to Measure Flame Height Using Imaging Software:

1. Take at least 10 images of each flame condition
2. Upload image to image J (or imaging software)
3. Locate the peak of the flame, and draw a line across to the scale
    a. The peak should be part of the continuous flame, not a portion that is completely detached
    b. The line angle can be adjusted so it is 180°, thus making it perfectly horizontal

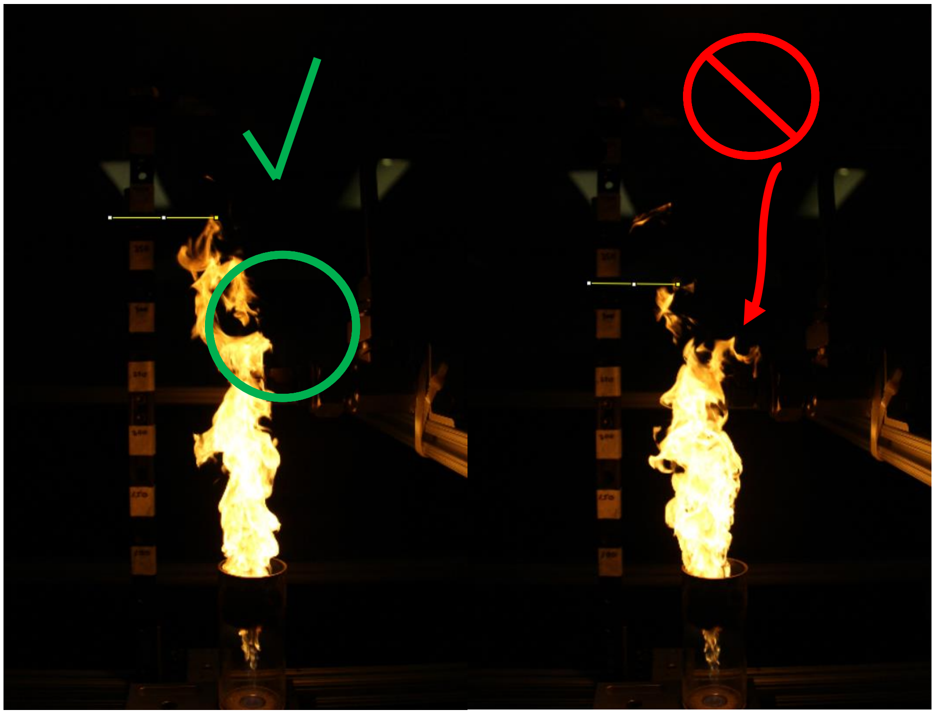

4. Once line has been drawing, use marker tool to mark off the point on the scale where the line intersects

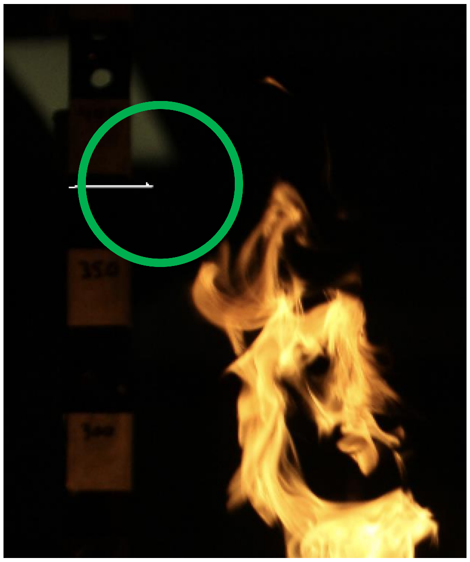

5. Draw a line between the bottom of the two scale points surrounding the marker, and set the scale to 50 mm

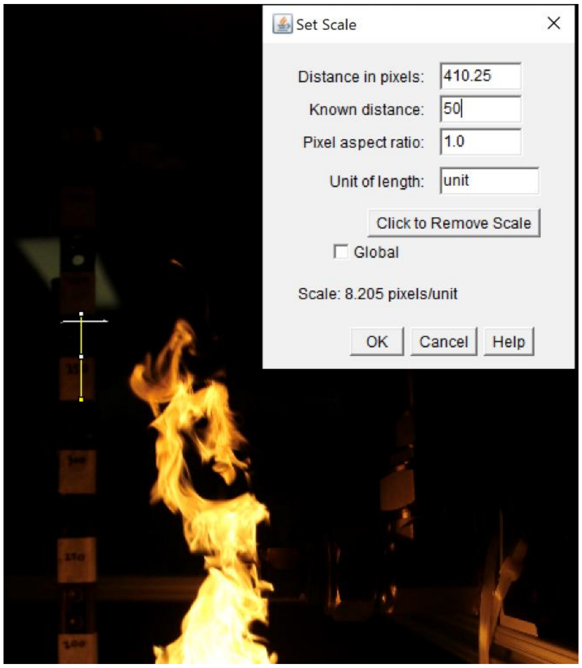

Set Scale

Distance in pixels: 410.25

Known distance: 50

Pixel aspect ratio: 1.0

Unit of length: unit

☐ Global

Scale: 8.205 pixels/unit

6. Draw another straight line from bottom of scale below the horizontal line, to the horizontal line, and take the measurement

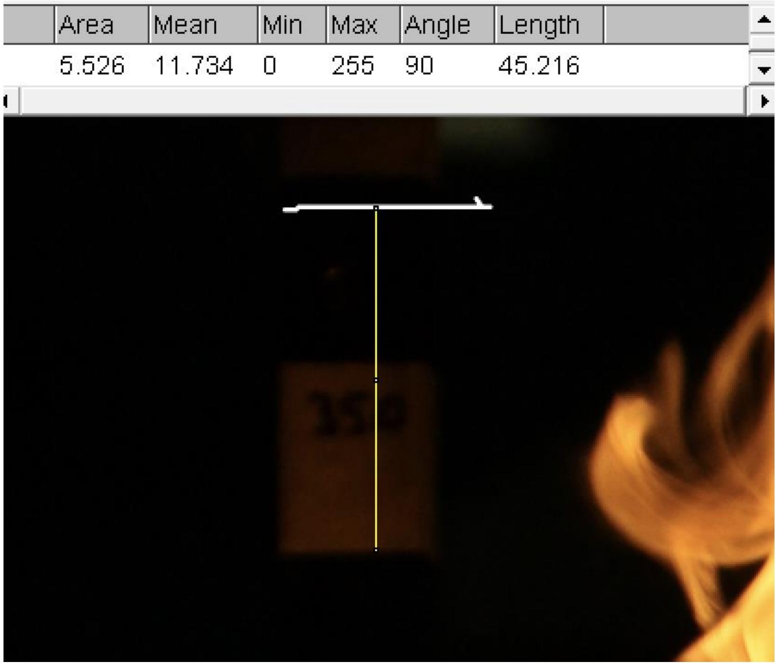

Area	Mean	Min	Max	Angle	Length
5.526	11.734	0	255	90	45.216

7. Add the measurement to the value of the scale below it

$$Scale\ Height = 45 + 350 = 395.216$$

8. Subtract 37mm from the total height (difference from bottom of scale to the burner

$$Flame\ Height = 395 - 37 = 358$$

9. Average the values of the 10 images to receive an approximate flame height

A.6 Pressurised Air CO_2 Consistency

The Dekati dilution was isolated and further investigated. The Dekati is provided with compressed air from a central lab compressor with connection to the wall. Upon recording CO_2 concentrations from the wall air, it was found that the CO_2 concentration varied in waves. Figure S6 shows the varying concentrations for three different days and the average CO_2 content after second stage dilution during hot tests. With the amplitude of the wave variation being from ≈0.1-0.15 ppm/1000 (seen in Figure A6), this leads to variation of up to 15%, which makes a significant impact on the calculated dilution ratio. The reason for wave-like variation from the wall supplied air is currently unknown, and it is likely not the only reason for dilution ratio variation, but it is a reasonable factor to be addressed.

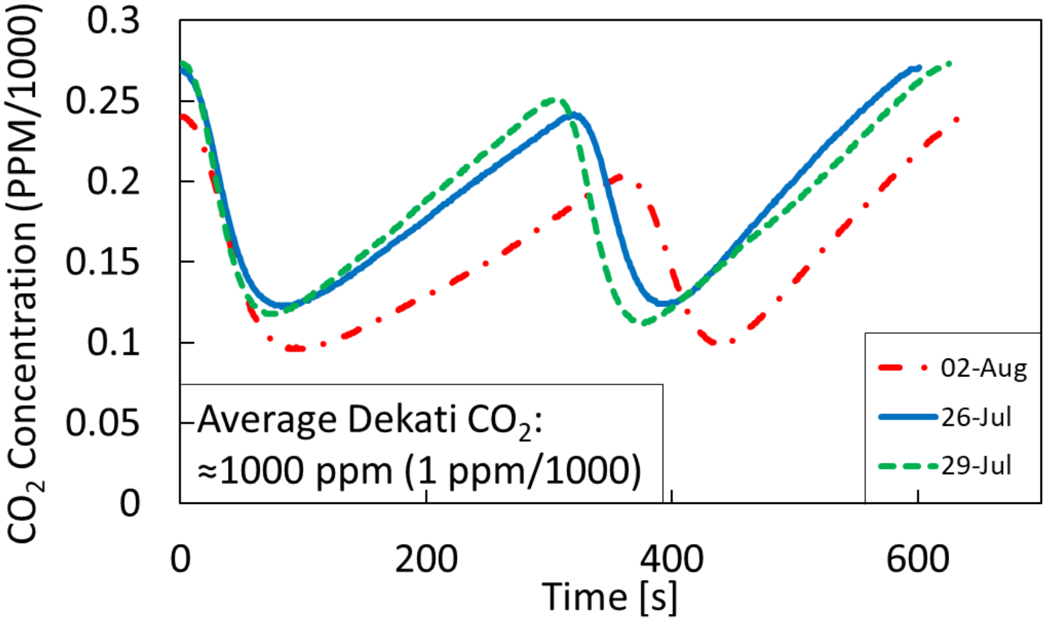

Figure A6: Variations in CO_2 concentration from compressed air supply to the Dekati diluter as a function of time for three different test days. The average CO_2 concentration in the sample after second stage dilution during hot tests was ≈1000 ppm.

Tests have been done to check for an ideal air pressure to operate at, while maintaining enough negative pressure by the operating Dekati to pull sufficient sample from the vacuum exhaust line. Figure A7 identifies the variability in CO_2 from the wall at different operating pressures. Previously, for the results discussed in this work, the Dekati operated with an air pressure of 35 psig. The tests done for Figure A7 show that operating at a pressure of 40 psig could minimize the variation in CO_2.

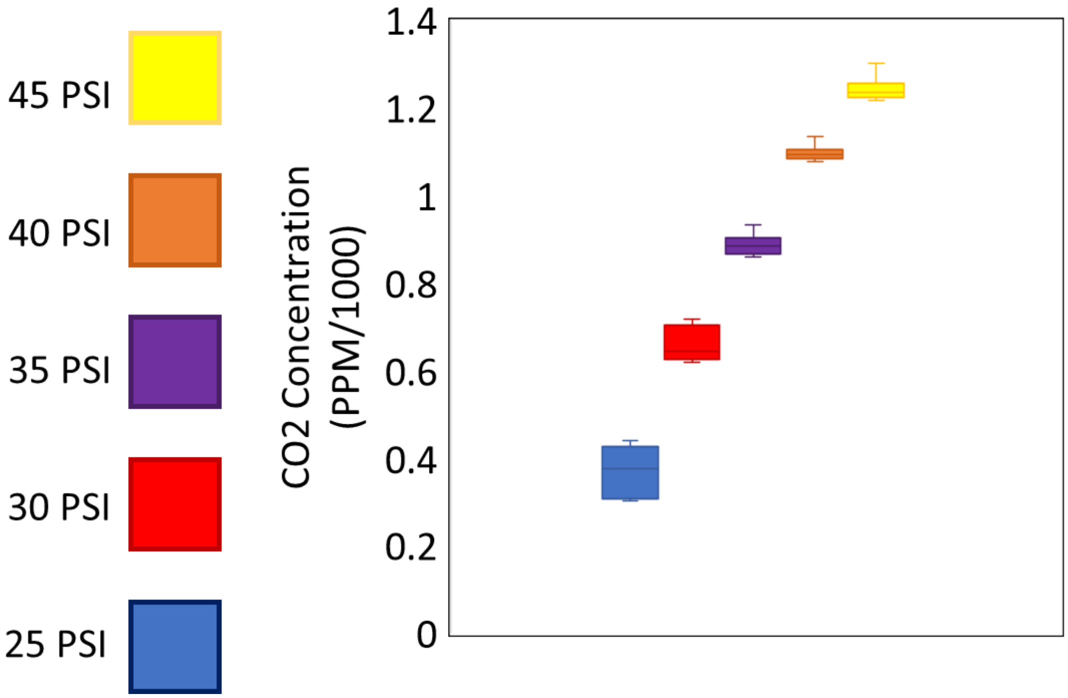

Figure A7: Variability in CO_2 concentration at different compressed air pressures measured after the Dekati diluter second stage dilution. The whiskers represent maximum and minimum values, and the boxes identify 2nd and 3rd quartiles, showing where 50% of the data is located. Pressure set at 40 psig results in the least amount of variation and spread, while setting the pressure to 25 psig would have the largest variation and spread. Results discussed in this work were collected with 35 psig.

A.7 Detailed TOA Results

A Sunset Laboratory OCEC Carbon Aerosol Analyzer was used here to identify OC and EC contents of sample quartz filters using the TOA process and thermograms were produced to show the process of measurement. TOA uses a heating process to detect organic and elemental carbon from a punch-out of a quartz filter. The carbon is removed from the filter in gaseous form and mixed with a manganese oxide where the carbon is oxidized and becomes CO_2. The CO_2 then goes through a methanator and is converted to CH_4, where it is subsequently burned and quantified by the flame ionization detector (FID). Continuous optical measurements with a laser confirm the original organic carbon and compare it to the burned off elemental carbon as the filter is heated in stages.

Individual thermograms for all fuels and flame conditions were produced to get the EC/TC ratios presented in Figures 3.14 and 3.15 of the main body of this thesis. These thermograms are provided in this section where the thermogram for the 1st set of EC/TC measurements are provided followed by the 2nd set for each fuel and flame condition. It is important to note that the thermograms shown here are only of the front filters, and the recorded values in Figures 3.14 and 3.15 are considering the backer filter subtraction, so there are small discrepancies in the EC/TC values stated on the thermograms compared to Figures 3.14 and 3.15.

Mass contents of OC and EC are given at the top in bold, followed by instrument calibration settings and split point times. The thermogram has a green (FID1) and pink (FID2) line that identify the FID signal that measures CH_4 content. The laser transmission is given as a red line, and the ramping temperature steps are shown by a blue line. A single vertical black line shows the split point where carbon contents measured before this point are considered OC, and carbon measured after is considered EC. The split point is calculated using the thermal/optical-transmittance method. This method uses laser transmission and a photodetector to measure attenuation of the laser as some of the OC is pyrolyzed, remaining on the filter, and starts to absorb light. The second stage of the analysis starts when oxygen is introduced and the temperature ramps back up to oxidize EC and any pyrolyzed OC off the filter. This reduces the light-absorbing carbon which increases measured laser transmission. The split point is estimated when the power reaches its original value from the start of the procedure, typically after the oxidizing phase has started. For the following datasets, the oxygen is introduced at t = 420 seconds and recorded split points range from 537-569 seconds.

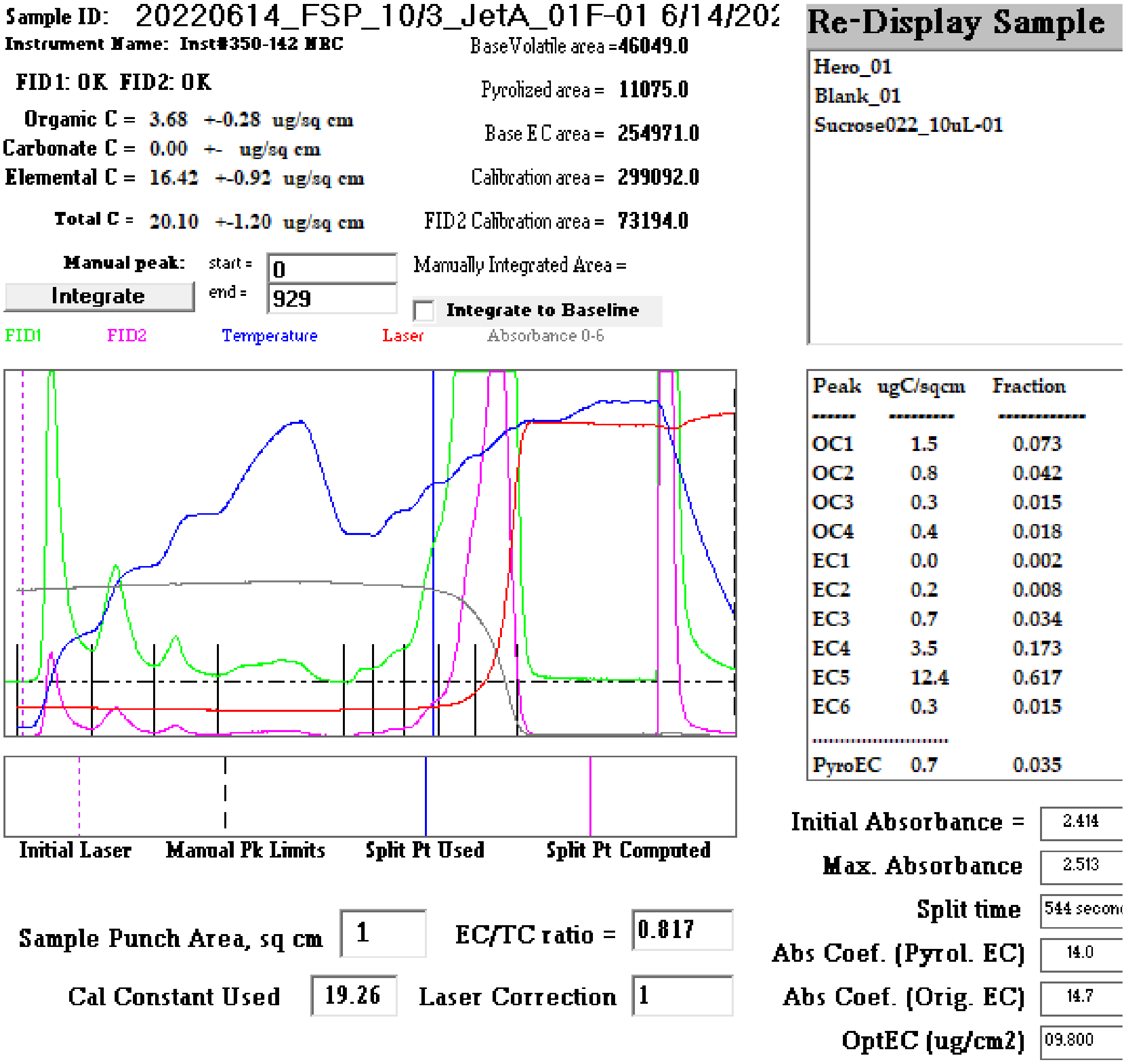

Sample ID: 20220614_FSP_10/3_JetA_01F-01 6/14/202

Instrument Name: Inst#350-142 NRC

Base Volatile area = 46049.0

FID1: OK FID2: OK

Pyrolized area = 11075.0

Organic C = 3.68 +-0.28 ug/sq cm

Carbonate C = 0.00 +- ug/sq cm

Elemental C = 16.42 +-0.92 ug/sq cm

Base E C area = 254971.0

Calibration area = 299092.0

Total C = 20.10 +-1.20 ug/sq cm

FID2 Calibration area = 73194.0

Manual peak: start = 0 end = 929

Manually Integrated Area =

☐ Integrate to Baseline

Sample Punch Area, sq cm 1

EC/TC ratio = 0.817

Cal Constant Used 19.26

Laser Correction 1

Hero_01
Blank_01
Sucrose022_10uL-01

Peak	ugC/sqcm	Fraction
OC1	1.5	0.073
OC2	0.8	0.042
OC3	0.3	0.015
OC4	0.4	0.018
EC1	0.0	0.002
EC2	0.2	0.008
EC3	0.7	0.034
EC4	3.5	0.173
EC5	12.4	0.617
EC6	0.3	0.015
PyroEC	0.7	0.035

Initial Absorbance = 2.414

Max. Absorbance 2.513

Split time 544 second

Abs Coef. (Pyrol. EC) 14.0

Abs Coef. (Orig. EC) 14.7

OptEC (ug/cm2) 09.800

Figure A8: Detailed TOA elemental, organic, and total carbon results for the 1st set of a Jet A1 10/3.00 flame condition.

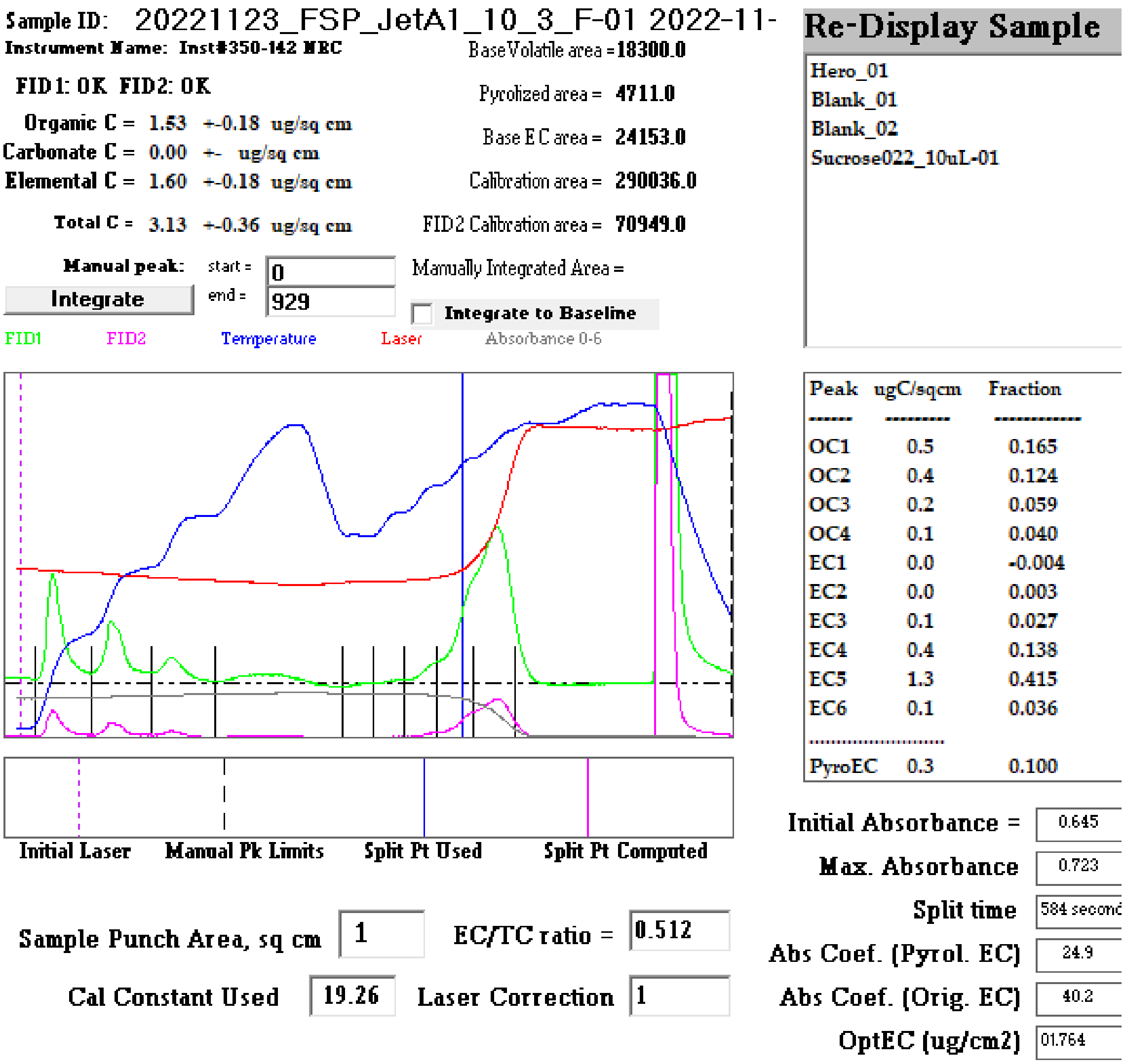

Sample ID: 20221123_FSP_JetA1_10_3_F-01 2022-11-

Instrument Name: Inst#350-142 NRC

FID1: OK FID2: OK

Organic C = 1.53 +-0.18 ug/sq cm
Carbonate C = 0.00 +- ug/sq cm
Elemental C = 1.60 +-0.18 ug/sq cm

Total C = 3.13 +-0.36 ug/sq cm

Base Volatile area = 18300.0
Pyrolized area = 4711.0
Base E C area = 24153.0
Calibration area = 290036.0
FID2 Calibration area = 70949.0

Manual peak: start = 0 end = 929

Manually Integrated Area =

☐ Integrate to Baseline

Hero_01
Blank_01
Blank_02
Sucrose022_10uL-01

Peak	ugC/sqcm	Fraction
OC1	0.5	0.165
OC2	0.4	0.124
OC3	0.2	0.059
OC4	0.1	0.040
EC1	0.0	-0.004
EC2	0.0	0.003
EC3	0.1	0.027
EC4	0.4	0.138
EC5	1.3	0.415
EC6	0.1	0.036
PyroEC	0.3	0.100

Initial Absorbance = 0.645
Max. Absorbance 0.723
Split time 584 second
Abs Coef. (Pyrol. EC) 24.9
Abs Coef. (Orig. EC) 40.2
OptEC (ug/cm2) 01.764

Sample Punch Area, sq cm 1
EC/TC ratio = 0.512
Cal Constant Used 19.26
Laser Correction 1

Figure A9: Detailed TOA elemental, organic, and total carbon results for the 2nd set of a Jet A1 10/3.00 flame condition.

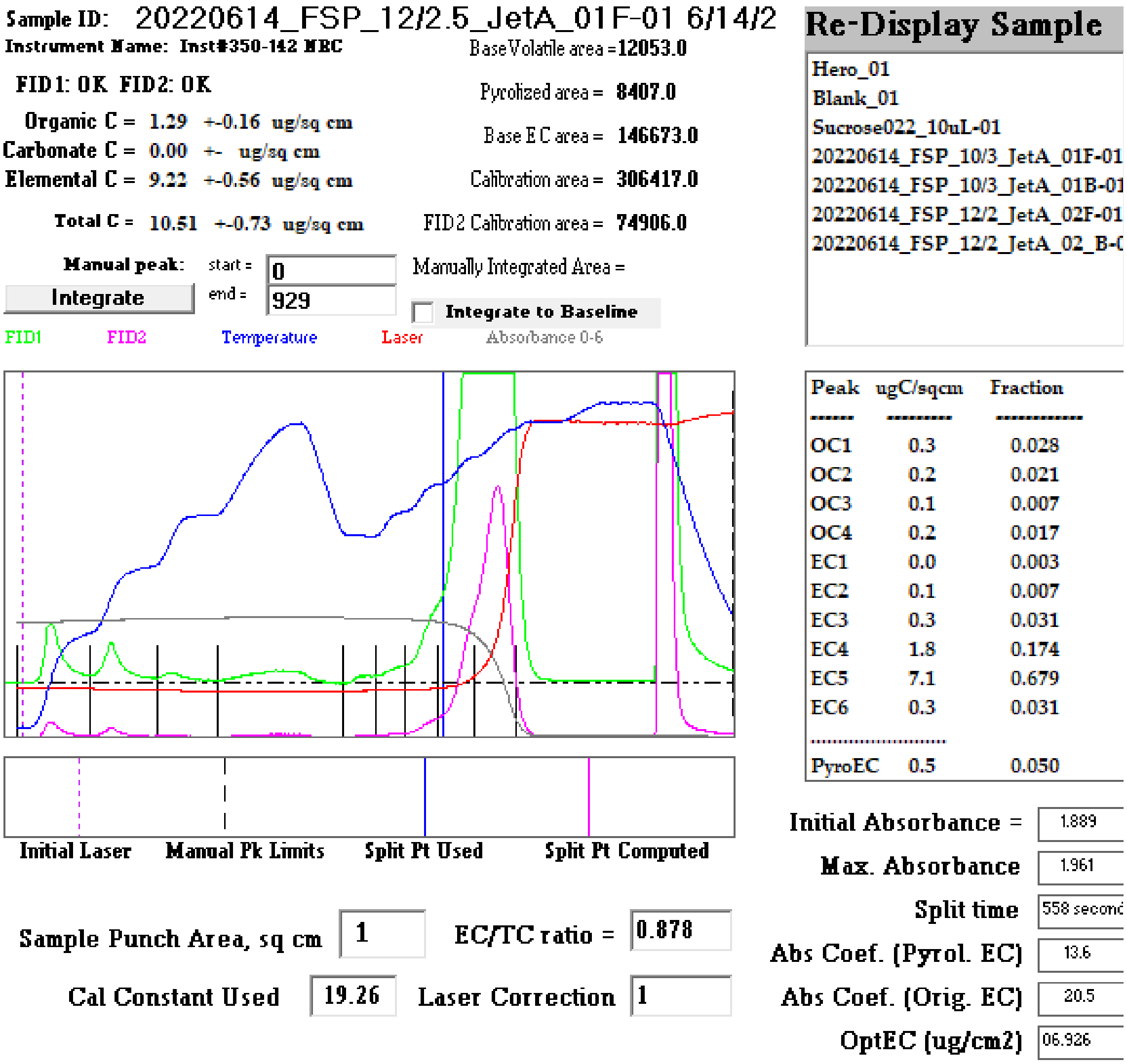

Sample ID: 20220614_FSP_12/2.5_JetA_01F-01 6/14/2

Instrument Name: Inst#350-142 NRC

Base Volatile area = 12053.0

FID1: OK FID2: OK

Organic C = 1.29 +-0.16 ug/sq cm

Carbonate C = 0.00 +- ug/sq cm

Elemental C = 9.22 +-0.56 ug/sq cm

Total C = 10.51 +-0.73 ug/sq cm

Pyrolized area = 8407.0

Base EC area = 146673.0

Calibration area = 306417.0

FID2 Calibration area = 74906.0

Manual peak: start = 0 end = 929

Manually Integrated Area =

☐ Integrate to Baseline

Hero_01
Blank_01
Sucrose022_10uL-01
20220614_FSP_10/3_JetA_01F-01
20220614_FSP_10/3_JetA_01B-01
20220614_FSP_12/2_JetA_02F-01
20220614_FSP_12/2_JetA_02_B-(

Peak	ugC/sqcm	Fraction
OC1	0.3	0.028
OC2	0.2	0.021
OC3	0.1	0.007
OC4	0.2	0.017
EC1	0.0	0.003
EC2	0.1	0.007
EC3	0.3	0.031
EC4	1.8	0.174
EC5	7.1	0.679
EC6	0.3	0.031
PyroEC	0.5	0.050

Initial Absorbance = 1.889

Max. Absorbance 1.961

Split time 558 second

Abs Coef. (Pyrol. EC) 13.6

Abs Coef. (Orig. EC) 20.5

OptEC (ug/cm2) 06.926

Sample Punch Area, sq cm 1

EC/TC ratio = 0.878

Cal Constant Used 19.26

Laser Correction 1

Figure A10: Detailed TOA elemental, organic, and total carbon results for the 1st set of a Jet A1 12/2.50 flame condition.

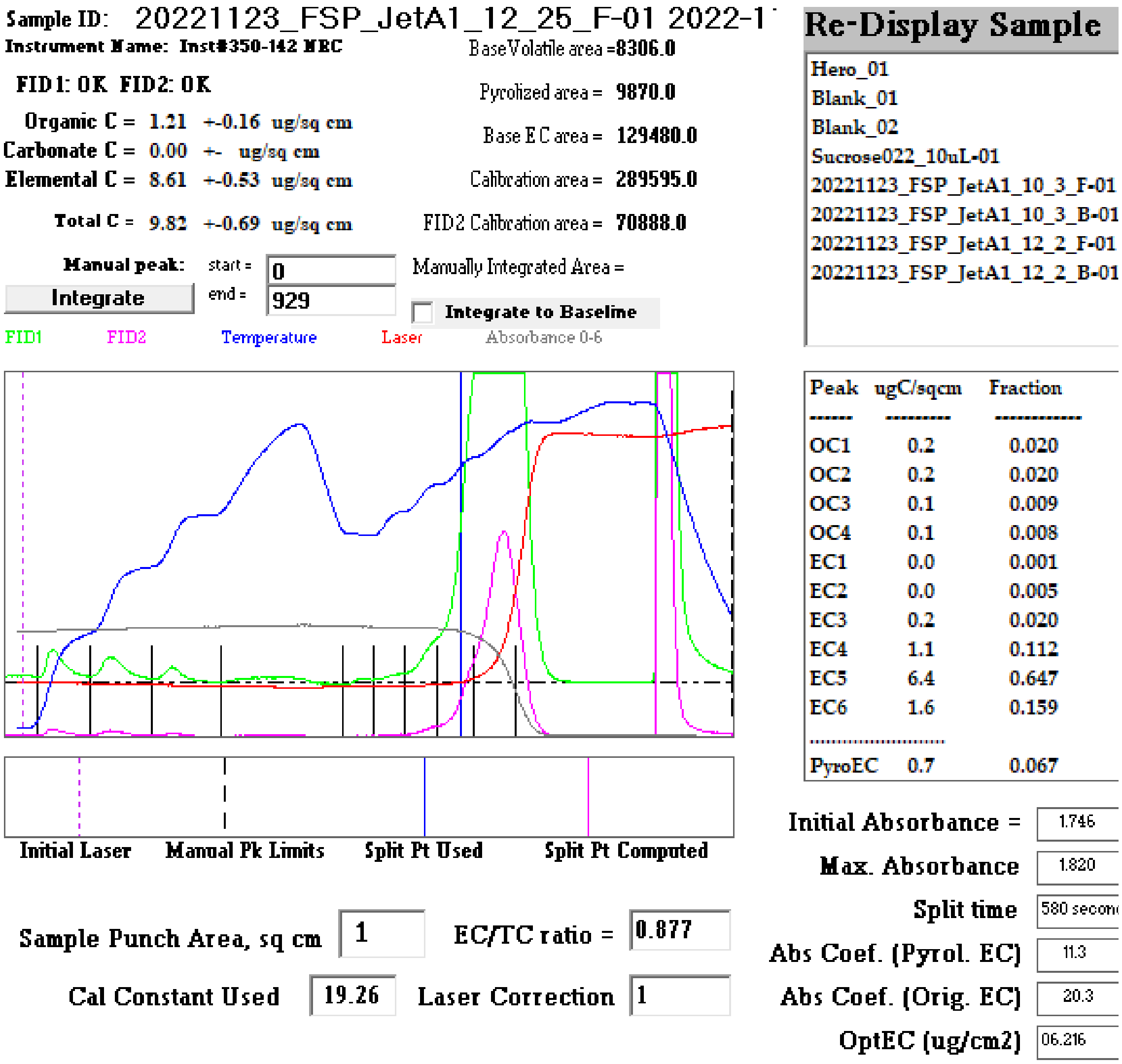

Sample ID: 20221123_FSP_JetA1_12_25_F-01 2022-1

Instrument Name: Inst#350-142 NRC

FID1: OK FID2: OK

Organic C = 1.21 +-0.16 ug/sq cm

Carbonate C = 0.00 +- ug/sq cm

Elemental C = 8.61 +-0.53 ug/sq cm

Total C = 9.82 +-0.69 ug/sq cm

Base Volatile area = 8306.0

Pyrolized area = 9870.0

Base E C area = 129480.0

Calibration area = 289595.0

FID2 Calibration area = 70888.0

Manual peak: start = 0 end = 929

Manually Integrated Area =

☐ Integrate to Baseline

Hero_01
Blank_01
Blank_02
Sucrose022_10uL-01
20221123_FSP_JetA1_10_3_F-01
20221123_FSP_JetA1_10_3_B-01
20221123_FSP_JetA1_12_2_F-01
20221123_FSP_JetA1_12_2_B-01

Peak	ugC/sqcm	Fraction
OC1	0.2	0.020
OC2	0.2	0.020
OC3	0.1	0.009
OC4	0.1	0.008
EC1	0.0	0.001
EC2	0.0	0.005
EC3	0.2	0.020
EC4	1.1	0.112
EC5	6.4	0.647
EC6	1.6	0.159
PyroEC	0.7	0.067

Sample Punch Area, sq cm 1

EC/TC ratio = 0.877

Cal Constant Used 19.26

Laser Correction 1

Initial Absorbance = 1.746

Max. Absorbance 1.820

Split time 580 secon

Abs Coef. (Pyrol. EC) 11.3

Abs Coef. (Orig. EC) 20.3

OptEC (ug/cm2) 06.216

Figure A11: Detailed TOA elemental, organic, and total carbon results for the 2nd set of a Jet A1 12/2.50 flame condition.

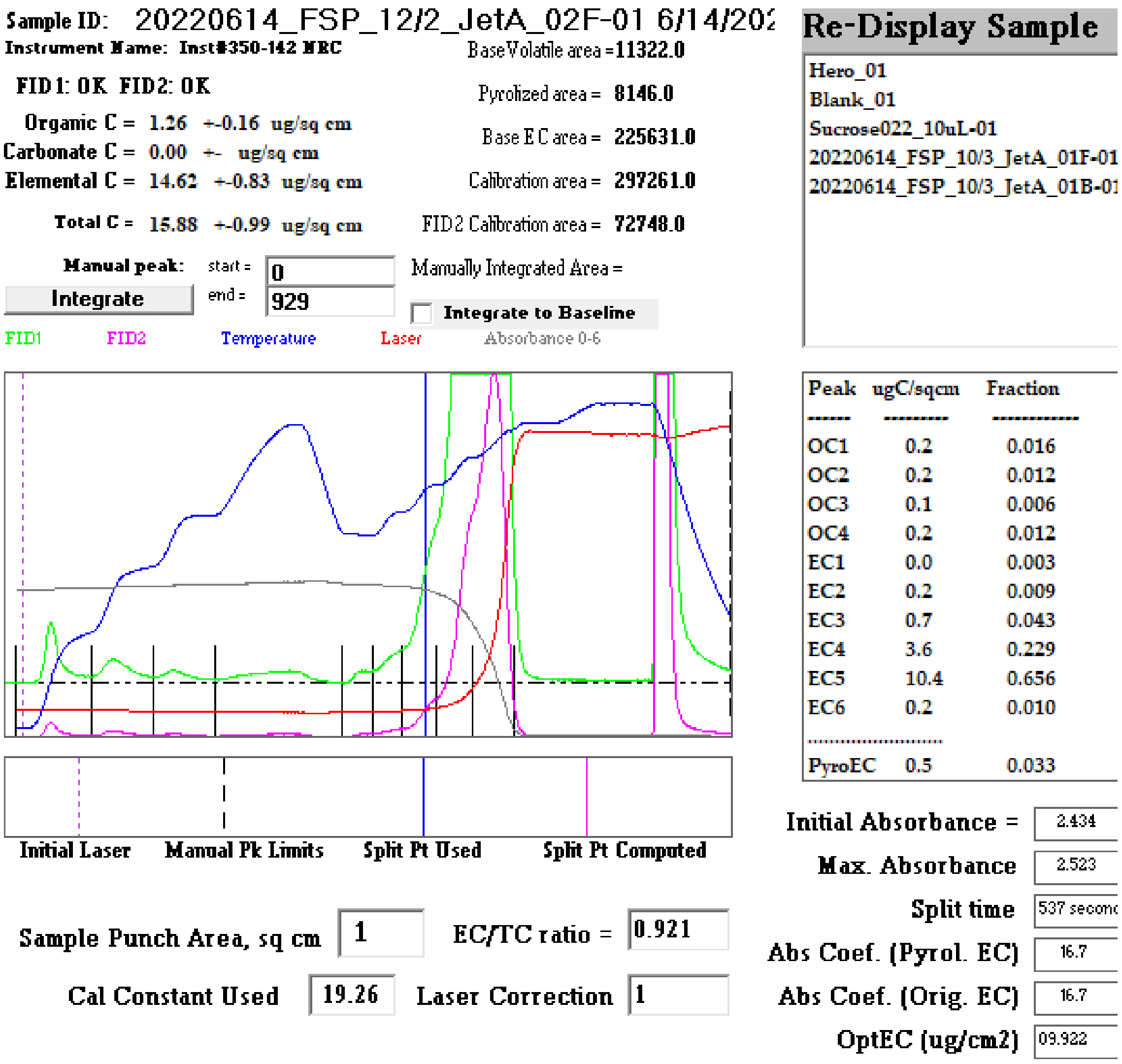

Sample ID: 20220614_FSP_12/2_JetA_02F-01 6/14/202

Instrument Name: Inst#350-142 NRC

Base Volatile area = 11322.0

FID1: OK FID2: OK

Pyrolized area = 8146.0

Organic C = 1.26 +-0.16 ug/sq cm

Carbonate C = 0.00 +- ug/sq cm

Base EC area = 225631.0

Elemental C = 14.62 +-0.83 ug/sq cm

Calibration area = 297261.0

Total C = 15.88 +-0.99 ug/sq cm

FID2 Calibration area = 72748.0

Manual peak: start = 0

end = 929

Manually Integrated Area =

☐ Integrate to Baseline

Re-Display Sample

Hero_01
Blank_01
Sucrose022_10uL-01
20220614_FSP_10/3_JetA_01F-01
20220614_FSP_10/3_JetA_01B-01

Peak	ugC/sqcm	Fraction
------	---------	------------
OC1	0.2	0.016
OC2	0.2	0.012
OC3	0.1	0.006
OC4	0.2	0.012
EC1	0.0	0.003
EC2	0.2	0.009
EC3	0.7	0.043
EC4	3.6	0.229
EC5	10.4	0.656
EC6	0.2	0.010
PyroEC	0.5	0.033

Initial Absorbance = 2.434

Max. Absorbance 2.523

Split time 537 secon

Abs Coef. (Pyrol. EC) 16.7

Abs Coef. (Orig. EC) 16.7

OptEC (ug/cm2) 09.922

Sample Punch Area, sq cm 1

EC/TC ratio = 0.921

Cal Constant Used 19.26

Laser Correction 1

Figure A12: Detailed TOA elemental, organic, and total carbon results for the 1st set of a Jet A1 12/2.00 flame condition.

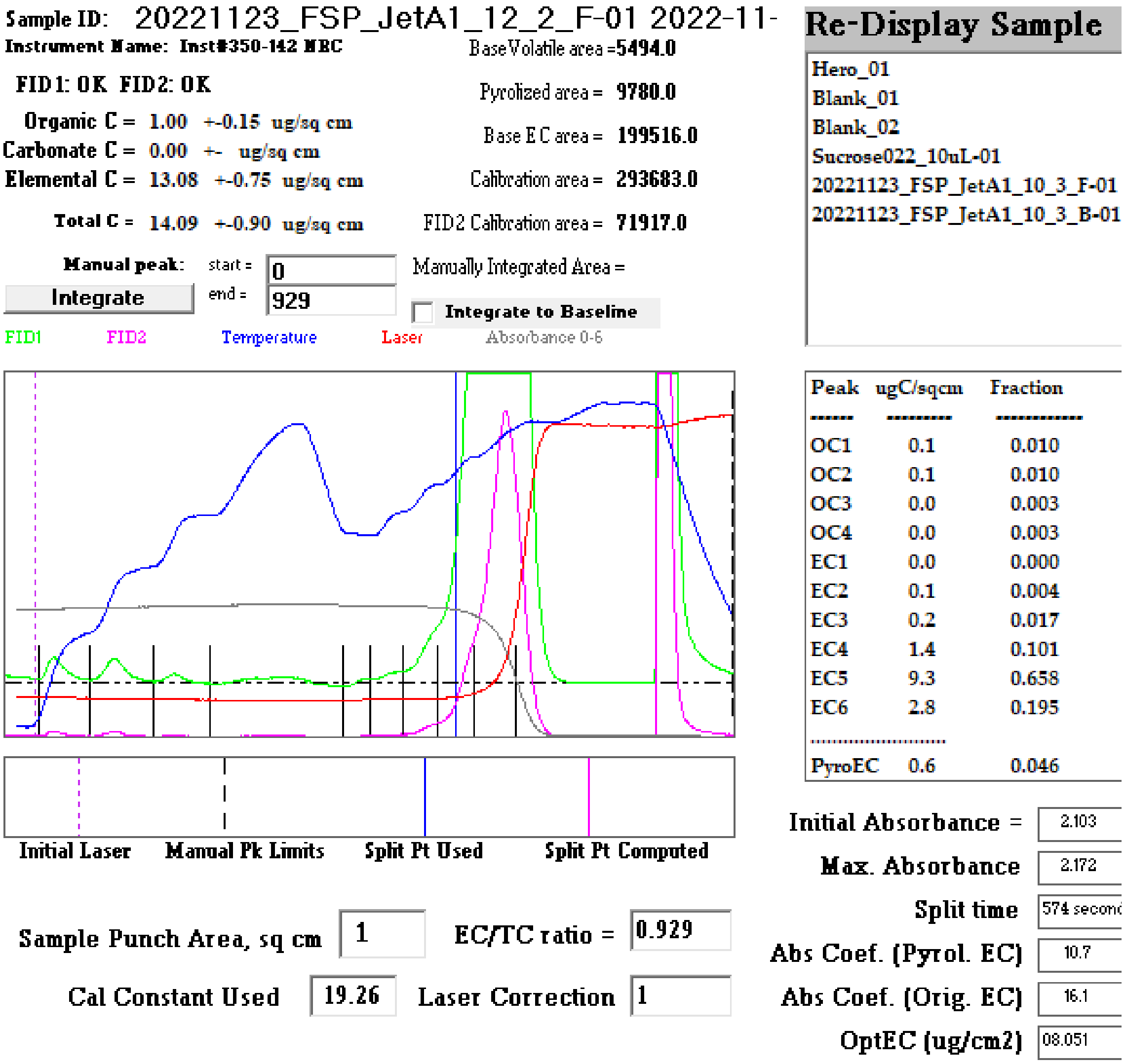

Sample ID: 20221123_FSP_JetA1_12_2_F-01 2022-11-
Instrument Name: Inst#350-142 NBC

FID1: OK FID2: OK

Organic C = 1.00 +-0.15 ug/sq cm
Carbonate C = 0.00 +- ug/sq cm
Elemental C = 13.08 +-0.75 ug/sq cm
Total C = 14.09 +-0.90 ug/sq cm

Base Volatile area = 5494.0
Pyrolized area = 9780.0
Base EC area = 199516.0
Calibration area = 293683.0
FID2 Calibration area = 71917.0

Manual peak: start = 0 end = 929
Manually Integrated Area =
☐ Integrate to Baseline

Hero_01
Blank_01
Blank_02
Sucrose022_10uL-01
20221123_FSP_JetA1_10_3_F-01
20221123_FSP_JetA1_10_3_B-01

Peak	ugC/sqcm	Fraction
OC1	0.1	0.010
OC2	0.1	0.010
OC3	0.0	0.003
OC4	0.0	0.003
EC1	0.0	0.000
EC2	0.1	0.004
EC3	0.2	0.017
EC4	1.4	0.101
EC5	9.3	0.658
EC6	2.8	0.195
PyroEC	0.6	0.046

Sample Punch Area, sq cm 1
EC/TC ratio = 0.929
Cal Constant Used 19.26
Laser Correction 1

Initial Absorbance = 2.103
Max. Absorbance 2.172
Split time 574 second
Abs Coef. (Pyrol. EC) 10.7
Abs Coef. (Orig. EC) 16.1
OptEC (ug/cm2) 08.051

Figure A13: Detailed TOA elemental, organic, and total carbon results for the 2nd set of a Jet A1 12/2.00 flame condition.

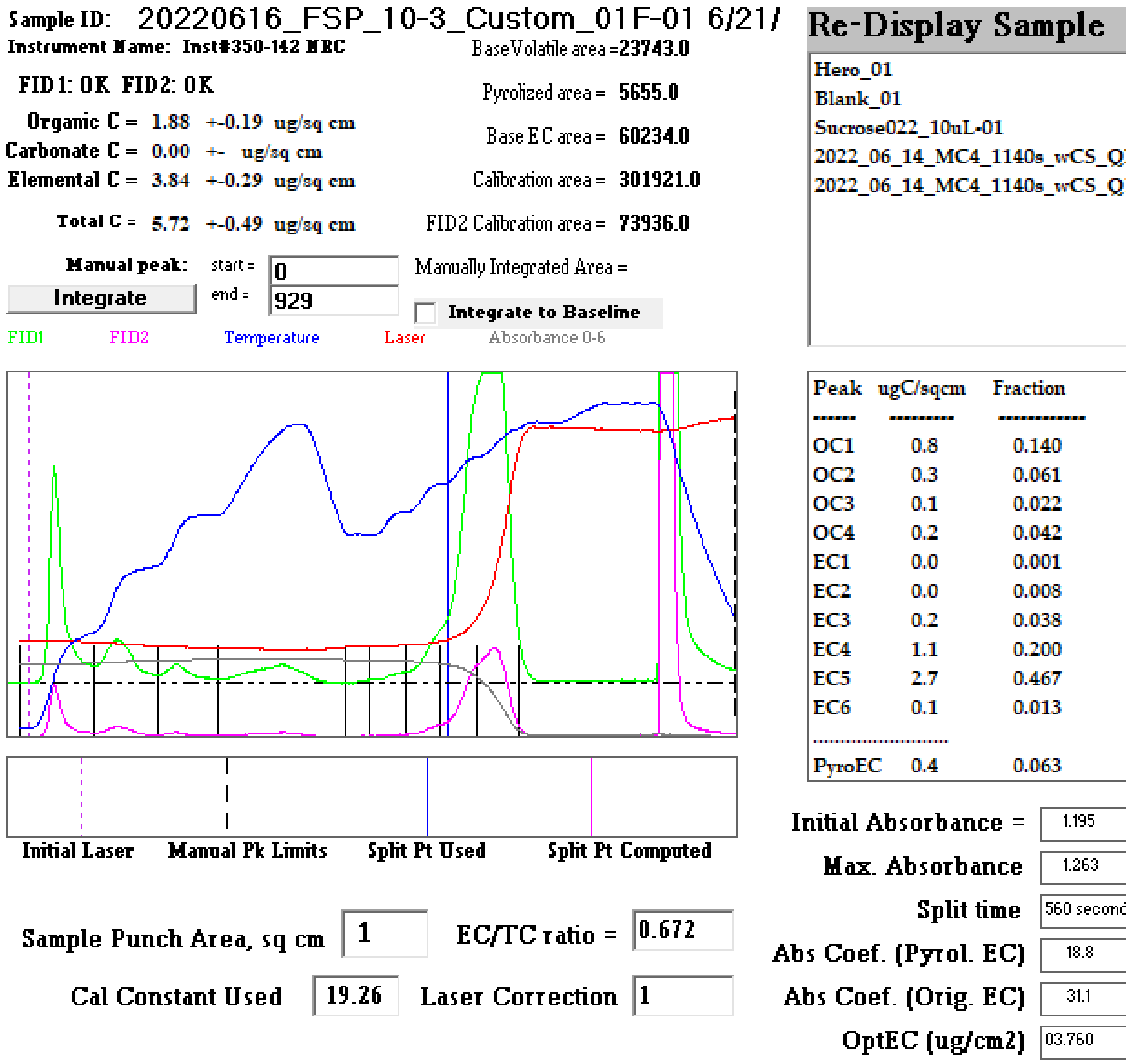

Sample ID: 20220616_FSP_10-3_Custom_01F-01 6/21/

Instrument Name: Inst#350-142 MRC

BaseVolatile area = 23743.0

FID1: OK FID2: OK

Pyrolized area = 5655.0

Organic C = 1.88 +-0.19 ug/sq cm

Carbonate C = 0.00 +- ug/sq cm

Base EC area = 60234.0

Elemental C = 3.84 +-0.29 ug/sq cm

Calibration area = 301921.0

Total C = 5.72 +-0.49 ug/sq cm

FID2 Calibration area = 73936.0

Manual peak: start = 0 end = 929

Manually Integrated Area =

☐ **Integrate to Baseline**

Hero_01
Blank_01
Sucrose022_10uL-01
2022_06_14_MC4_1140s_wCS_Q
2022_06_14_MC4_1140s_wCS_Q

Peak	ugC/sqcm	Fraction
------	---------	------------
OC1	0.8	0.140
OC2	0.3	0.061
OC3	0.1	0.022
OC4	0.2	0.042
EC1	0.0	0.001
EC2	0.0	0.008
EC3	0.2	0.038
EC4	1.1	0.200
EC5	2.7	0.467
EC6	0.1	0.013
....		
PyroEC	0.4	0.063

Initial Absorbance = 1.195

Max. Absorbance 1.263

Split time 560 second

Abs Coef. (Pyrol. EC) 18.8

Abs Coef. (Orig. EC) 31.1

OptEC (ug/cm2) 03.760

Sample Punch Area, sq cm 1

EC/TC ratio = 0.672

Cal Constant Used 19.26

Laser Correction 1

Figure A14: Detailed TOA elemental, organic, and total carbon results for the 1st set of a C10 10/3.00 flame condition.

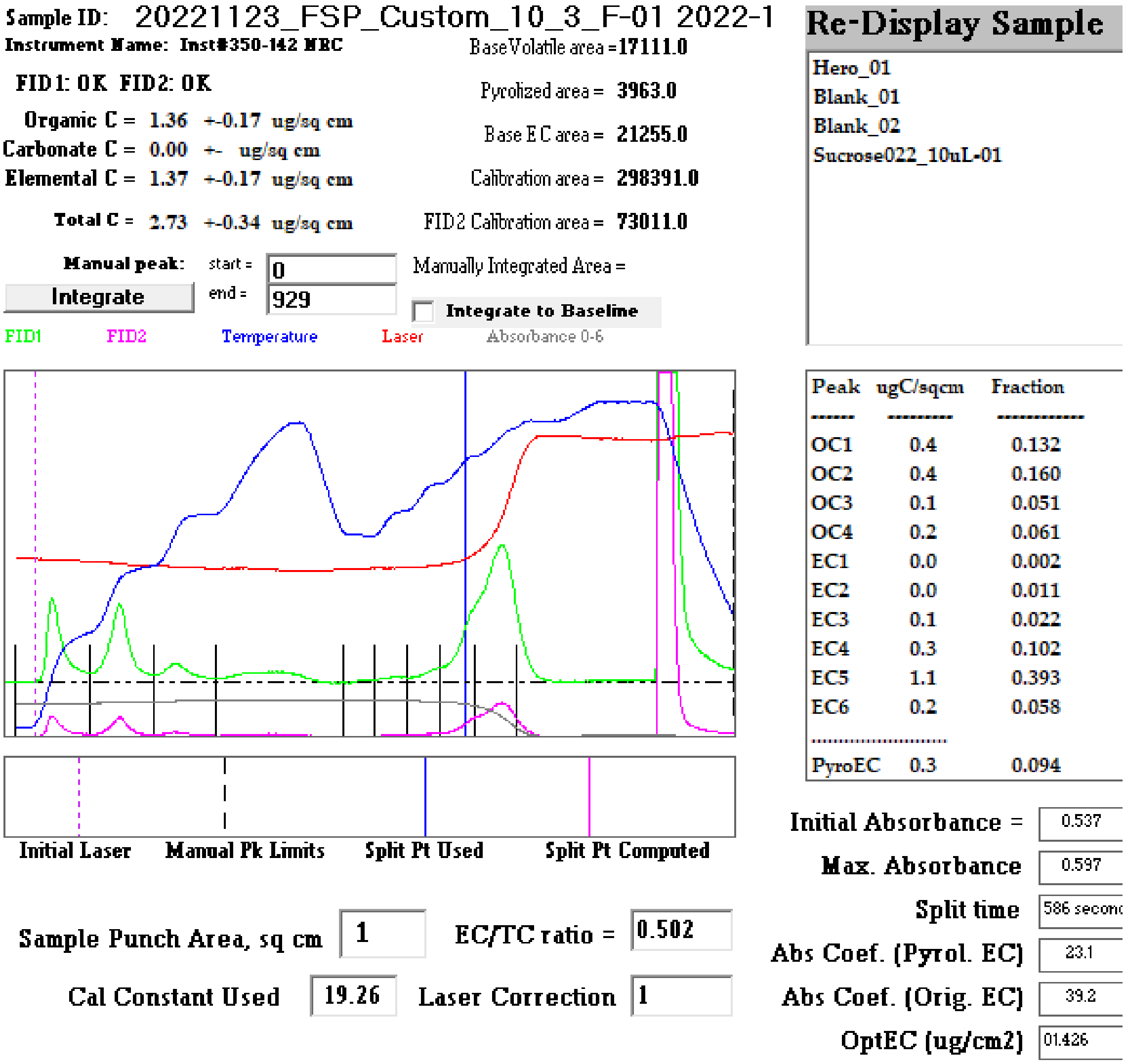

Sample ID: 20221123_FSP_Custom_10_3_F-01 2022-1

Instrument Name: Inst#350-142 NRC

FID1: OK FID2: OK

Organic C = 1.36 +-0.17 ug/sq cm

Carbonate C = 0.00 +- ug/sq cm

Elemental C = 1.37 +-0.17 ug/sq cm

Total C = 2.73 +-0.34 ug/sq cm

Base Volatile area = 17111.0

Pyrolized area = 3963.0

Base E C area = 21255.0

Calibration area = 298391.0

FID2 Calibration area = 73011.0

Manual peak: start = 0 end = 929

Manually Integrated Area =

☐ Integrate to Baseline

Hero_01
Blank_01
Blank_02
Sucrose022_10uL-01

Peak	ugC/sqcm	Fraction
OC1	0.4	0.132
OC2	0.4	0.160
OC3	0.1	0.051
OC4	0.2	0.061
EC1	0.0	0.002
EC2	0.0	0.011
EC3	0.1	0.022
EC4	0.3	0.102
EC5	1.1	0.393
EC6	0.2	0.058
PyroEC	0.3	0.094

Sample Punch Area, sq cm 1

EC/TC ratio = 0.502

Cal Constant Used 19.26

Laser Correction 1

Initial Absorbance = 0.537

Max. Absorbance 0.597

Split time 586 secon

Abs Coef. (Pyrol. EC) 23.1

Abs Coef. (Orig. EC) 39.2

OptEC (ug/cm2) 01.426

Figure A15: Detailed TOA elemental, organic, and total carbon results for the 2nd set of a C10 10/3.00 flame condition.

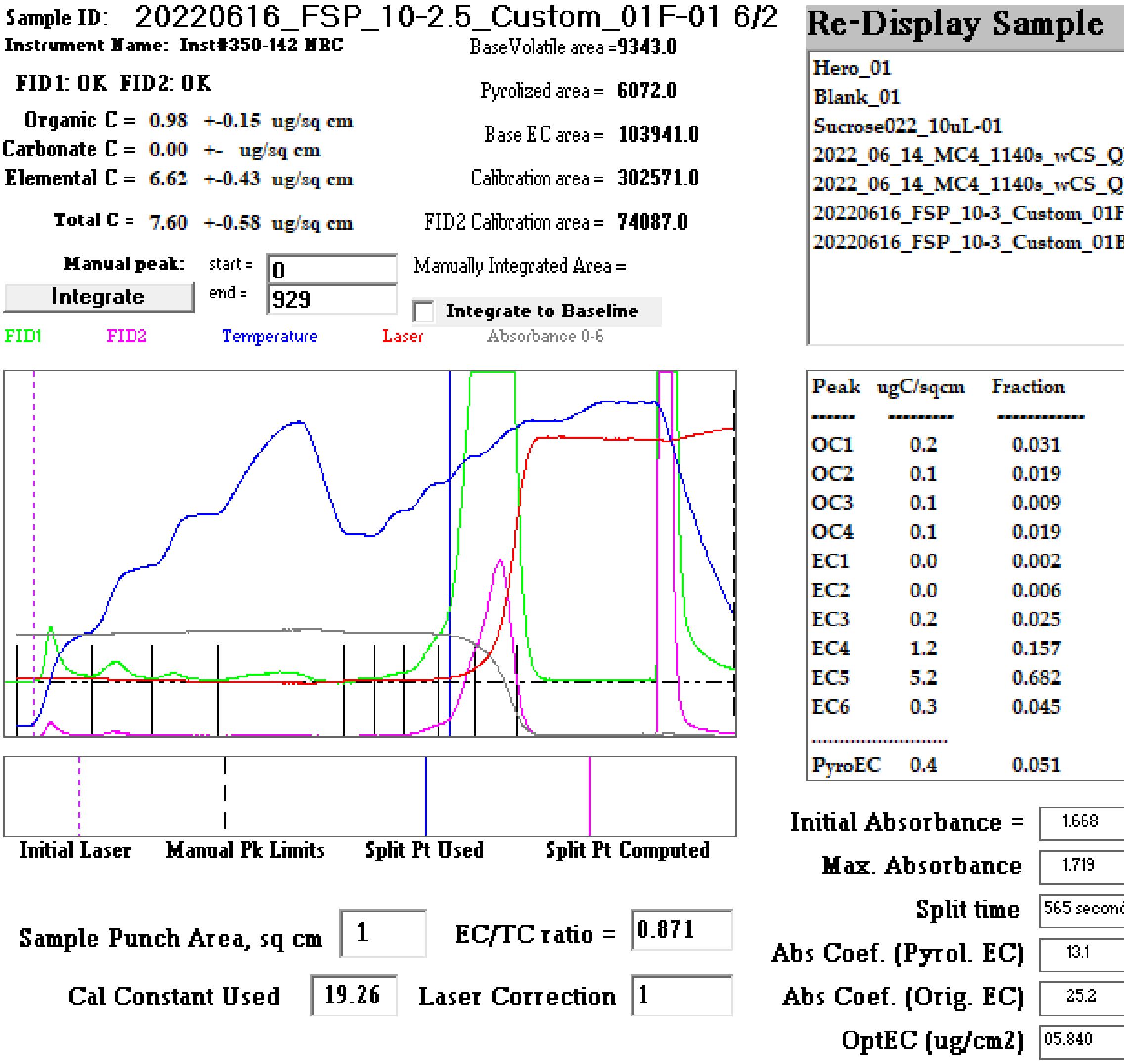

Sample ID: 20220616_FSP_10-2.5_Custom_01F-01 6/2
Instrument Name: Inst#350-142 NBC

FID1: OK FID2: OK

Organic C = 0.98 +-0.15 ug/sq cm
Carbonate C = 0.00 +- ug/sq cm
Elemental C = 6.62 +-0.43 ug/sq cm

Total C = 7.60 +-0.58 ug/sq cm

Base Volatile area = 9343.0
Pyrolized area = 6072.0
Base E C area = 103941.0
Calibration area = 302571.0
FID2 Calibration area = 74087.0

Manual peak: start = 0
end = 929
Manually Integrated Area =
☐ Integrate to Baseline

Hero_01
Blank_01
Sucrose022_10uL-01
2022_06_14_MC4_1140s_wCS_Q
2022_06_14_MC4_1140s_wCS_Q
20220616_FSP_10-3_Custom_01F
20220616_FSP_10-3_Custom_01E

Peak	ugC/sqcm	Fraction
OC1	0.2	0.031
OC2	0.1	0.019
OC3	0.1	0.009
OC4	0.1	0.019
EC1	0.0	0.002
EC2	0.0	0.006
EC3	0.2	0.025
EC4	1.2	0.157
EC5	5.2	0.682
EC6	0.3	0.045
PyroEC	0.4	0.051

Sample Punch Area, sq cm 1
EC/TC ratio = 0.871
Cal Constant Used 19.26
Laser Correction 1

Initial Absorbance = 1.668
Max. Absorbance 1.719
Split time 565 second
Abs Coef. (Pyrol. EC) 13.1
Abs Coef. (Orig. EC) 25.2
OptEC (ug/cm2) 05.840

Figure A16: Detailed TOA elemental, organic, and total carbon results for the 1st set of a C10 12/2.50 flame condition.

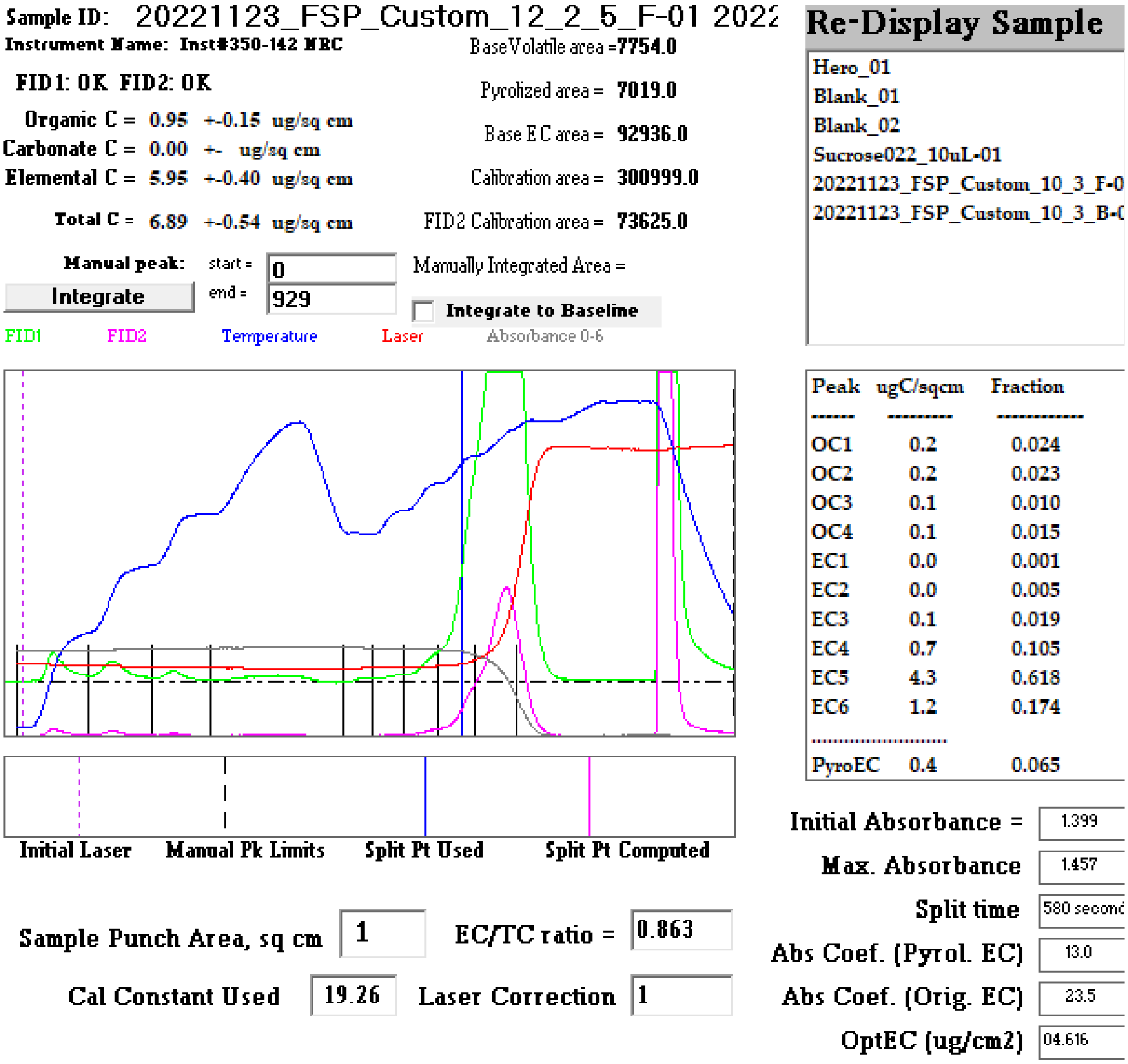

Sample ID: 20221123_FSP_Custom_12_2_5_F-01 2022

Instrument Name: Inst#350-142 NRC

Base Volatile area =7754.0

FID1: OK FID2: OK

Organic C = 0.95 +-0.15 ug/sq cm

Carbonate C = 0.00 +- ug/sq cm

Elemental C = 5.95 +-0.40 ug/sq cm

Total C = 6.89 +-0.54 ug/sq cm

Pyrolized area = 7019.0

Base EC area = 92936.0

Calibration area = 300999.0

FID2 Calibration area = 73625.0

Manual peak: start = 0 end = 929

Manually Integrated Area =

☐ Integrate to Baseline

Re-Display Sample

Hero_01
Blank_01
Blank_02
Sucrose022_10uL-01
20221123_FSP_Custom_10_3_F-0
20221123_FSP_Custom_10_3_B-(

Peak	ugC/sqcm	Fraction
OC1	0.2	0.024
OC2	0.2	0.023
OC3	0.1	0.010
OC4	0.1	0.015
EC1	0.0	0.001
EC2	0.0	0.005
EC3	0.1	0.019
EC4	0.7	0.105
EC5	4.3	0.618
EC6	1.2	0.174
PyroEC	0.4	0.065

Sample Punch Area, sq cm 1

EC/TC ratio = 0.863

Cal Constant Used 19.26

Laser Correction 1

Initial Absorbance = 1.399

Max. Absorbance 1.457

Split time 580 second

Abs Coef. (Pyrol. EC) 13.0

Abs Coef. (Orig. EC) 23.5

OptEC (ug/cm2) 04.616

Figure A17: Detailed TOA elemental, organic, and total carbon results for the 2nd set of a C10 12/2.50 flame condition.

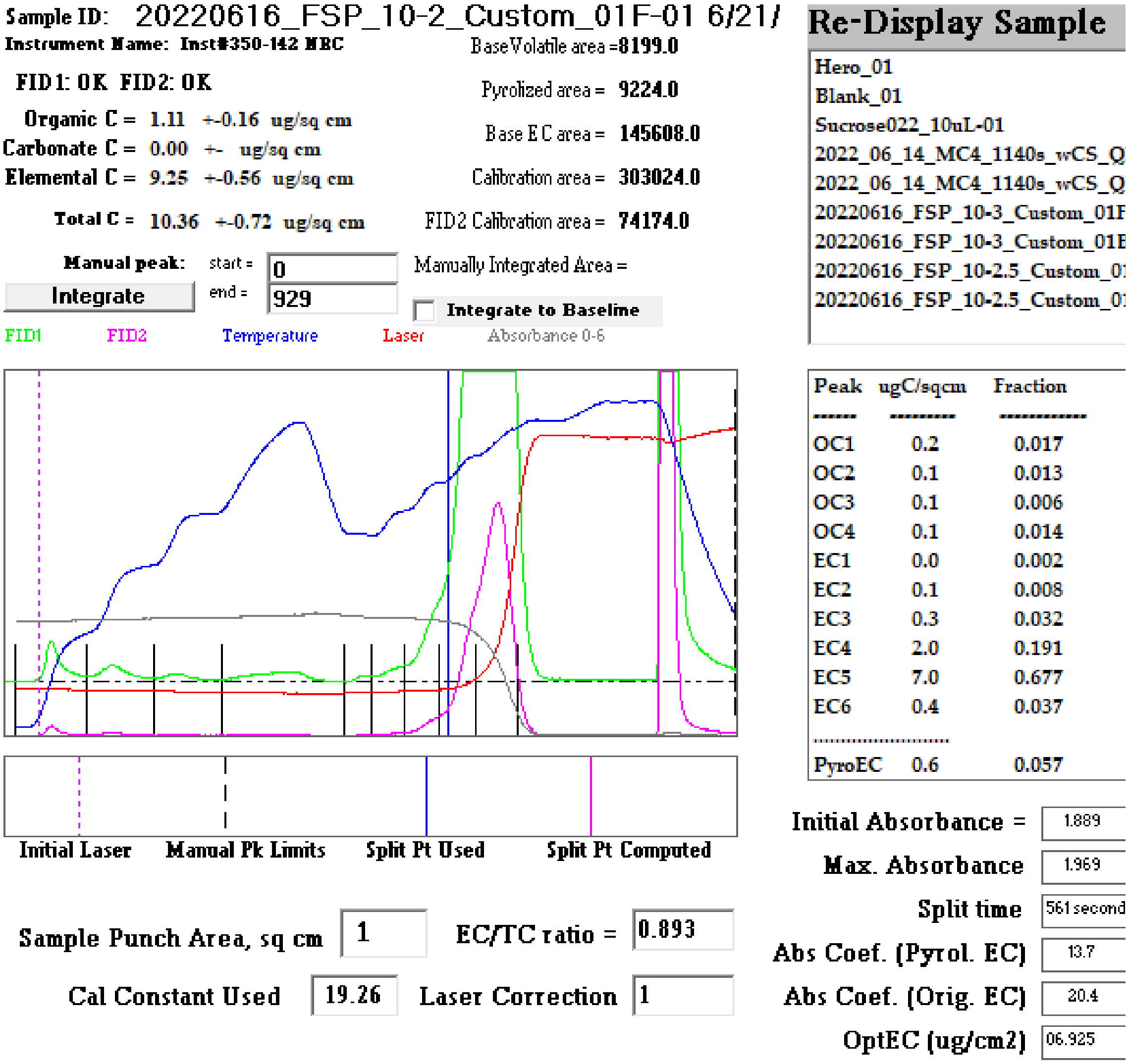

Sample ID: 20220616_FSP_10-2_Custom_01F-01 6/21/

Instrument Name: Inst#350-142 NBC

Base Volatile area = 8199.0

FID1: OK FID2: OK

Pyrolized area = 9224.0

Organic C = 1.11 +-0.16 ug/sq cm

Carbonate C = 0.00 +- ug/sq cm

Elemental C = 9.25 +-0.56 ug/sq cm

Base E C area = 145608.0

Calibration area = 303024.0

Total C = 10.36 +-0.72 ug/sq cm

FID2 Calibration area = 74174.0

Manual peak: start = 0

end = 929

Manually Integrated Area =

☐ Integrate to Baseline

Hero_01
Blank_01
Sucrose022_10uL-01
2022_06_14_MC4_1140s_wCS_Q
2022_06_14_MC4_1140s_wCS_Q
20220616_FSP_10-3_Custom_01F
20220616_FSP_10-3_Custom_01E
20220616_FSP_10-2.5_Custom_0
20220616_FSP_10-2.5_Custom_0

Peak	ugC/sqcm	Fraction
OC1	0.2	0.017
OC2	0.1	0.013
OC3	0.1	0.006
OC4	0.1	0.014
EC1	0.0	0.002
EC2	0.1	0.008
EC3	0.3	0.032
EC4	2.0	0.191
EC5	7.0	0.677
EC6	0.4	0.037
PyroEC	0.6	0.057

Initial Absorbance = 1.889

Max. Absorbance 1.969

Split time 561 second

Abs Coef. (Pyrol. EC) 13.7

Abs Coef. (Orig. EC) 20.4

OptEC (ug/cm2) 06.925

Sample Punch Area, sq cm 1

EC/TC ratio = 0.893

Cal Constant Used 19.26

Laser Correction 1

Figure A18: Detailed TOA elemental, organic, and total carbon results for the 1st set of a C10 12/2.00 flame condition.

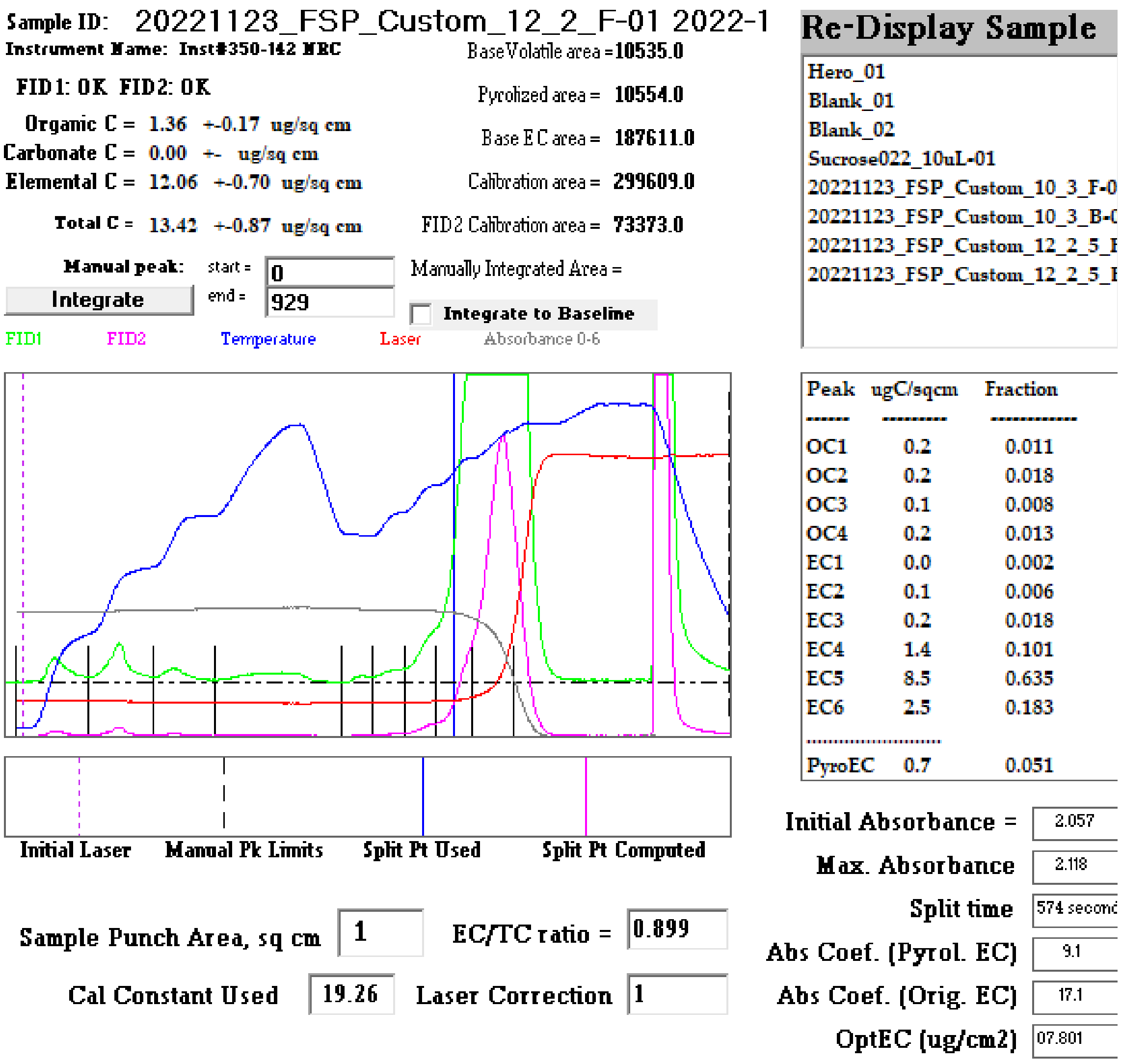

Sample ID: 20221123_FSP_Custom_12_2_F-01 2022-1

Instrument Name: Inst#350-142 NRC

FID1: OK FID2: OK

Organic C = 1.36 +-0.17 ug/sq cm
Carbonate C = 0.00 +- ug/sq cm
Elemental C = 12.06 +-0.70 ug/sq cm

Total C = 13.42 +-0.87 ug/sq cm

Base Volatile area = 10535.0
Pyrolized area = 10554.0
Base EC area = 187611.0
Calibration area = 299609.0
FID2 Calibration area = 73373.0

Manual peak: start = 0 end = 929

Manually Integrated Area =

☐ Integrate to Baseline

Hero_01
Blank_01
Blank_02
Sucrose022_10uL-01
20221123_FSP_Custom_10_3_F-0
20221123_FSP_Custom_10_3_B-(
20221123_FSP_Custom_12_2_5_I
20221123_FSP_Custom_12_2_5_I

Peak	ugC/sqcm	Fraction
------	---------	------------
OC1	0.2	0.011
OC2	0.2	0.018
OC3	0.1	0.008
OC4	0.2	0.013
EC1	0.0	0.002
EC2	0.1	0.006
EC3	0.2	0.018
EC4	1.4	0.101
EC5	8.5	0.635
EC6	2.5	0.183
....		
PyroEC	0.7	0.051

Initial Absorbance = 2.057
Max. Absorbance 2.118
Split time 574 second
Abs Coef. (Pyrol. EC) 9.1
Abs Coef. (Orig. EC) 17.1
OptEC (ug/cm2) 07.801

Sample Punch Area, sq cm 1
EC/TC ratio = 0.899
Cal Constant Used 19.26
Laser Correction 1

Figure A19: Detailed TOA elemental, organic, and total carbon results for the 2nd set of a C10 12/2.00 flame condition.

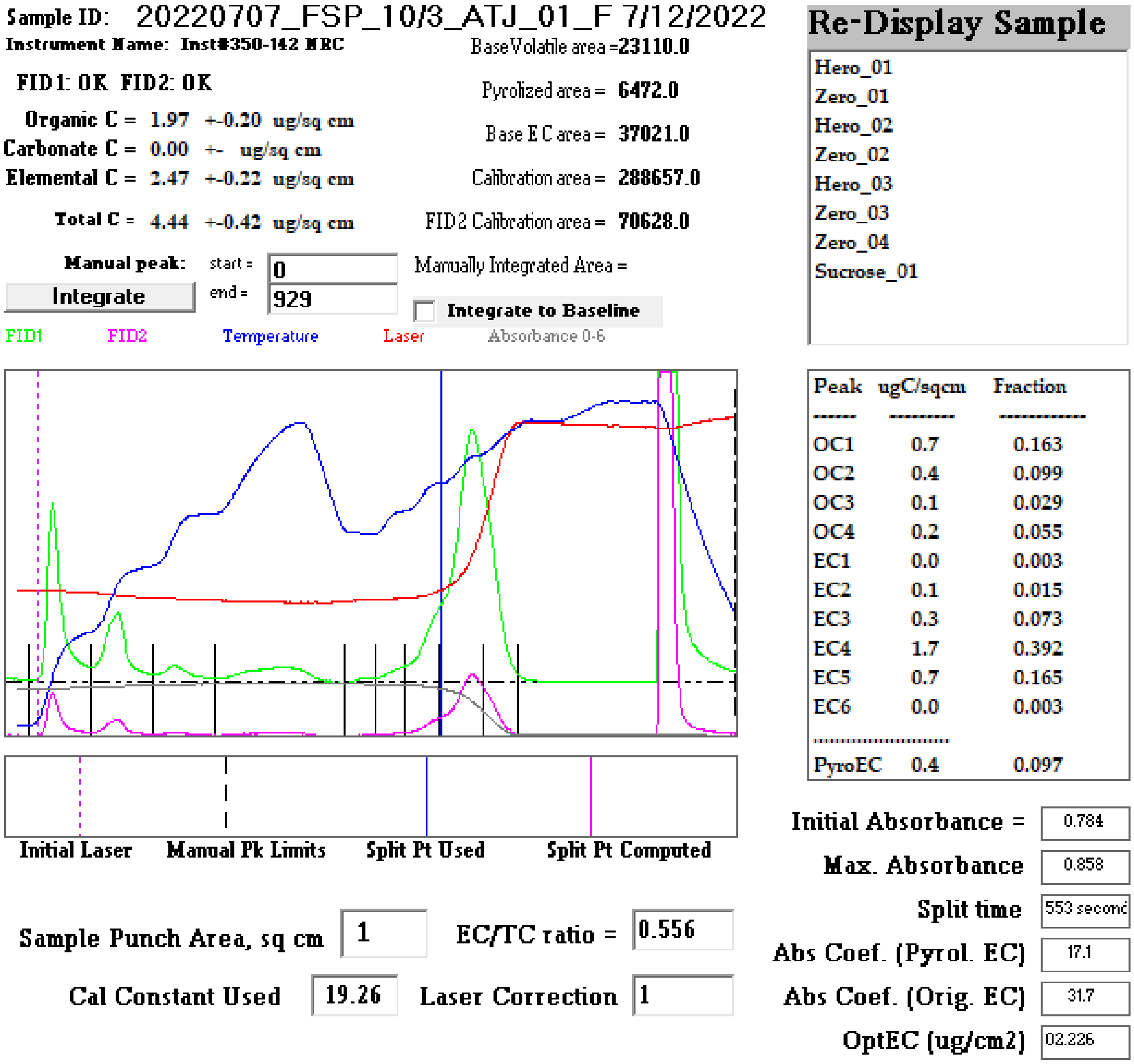

Sample ID: 20220707_FSP_10/3_ATJ_01_F 7/12/2022

Instrument Name: Inst#350-142 NBC

FID1: OK FID2: OK

Organic C = 1.97 +-0.20 ug/sq cm

Carbonate C = 0.00 +- ug/sq cm

Elemental C = 2.47 +-0.22 ug/sq cm

Total C = 4.44 +-0.42 ug/sq cm

Base Volatile area = 23110.0

Pyrolized area = 6472.0

Base E C area = 37021.0

Calibration area = 288657.0

FID2 Calibration area = 70628.0

Manual peak: start = 0 end = 929

Manually Integrated Area =

☐ Integrate to Baseline

Hero_01
Zero_01
Hero_02
Zero_02
Hero_03
Zero_03
Zero_04
Sucrose_01

Peak	ugC/sqcm	Fraction
OC1	0.7	0.163
OC2	0.4	0.099
OC3	0.1	0.029
OC4	0.2	0.055
EC1	0.0	0.003
EC2	0.1	0.015
EC3	0.3	0.073
EC4	1.7	0.392
EC5	0.7	0.165
EC6	0.0	0.003
PyroEC	0.4	0.097

Sample Punch Area, sq cm 1

EC/TC ratio = 0.556

Cal Constant Used 19.26

Laser Correction 1

Initial Absorbance = 0.784

Max. Absorbance 0.858

Split time 553 second

Abs Coef. (Pyrol. EC) 17.1

Abs Coef. (Orig. EC) 31.7

OptEC (ug/cm2) 02.226

Figure A20: Detailed TOA elemental, organic, and total carbon results for the 1st set of a ATJ 10/3.00 flame condition.

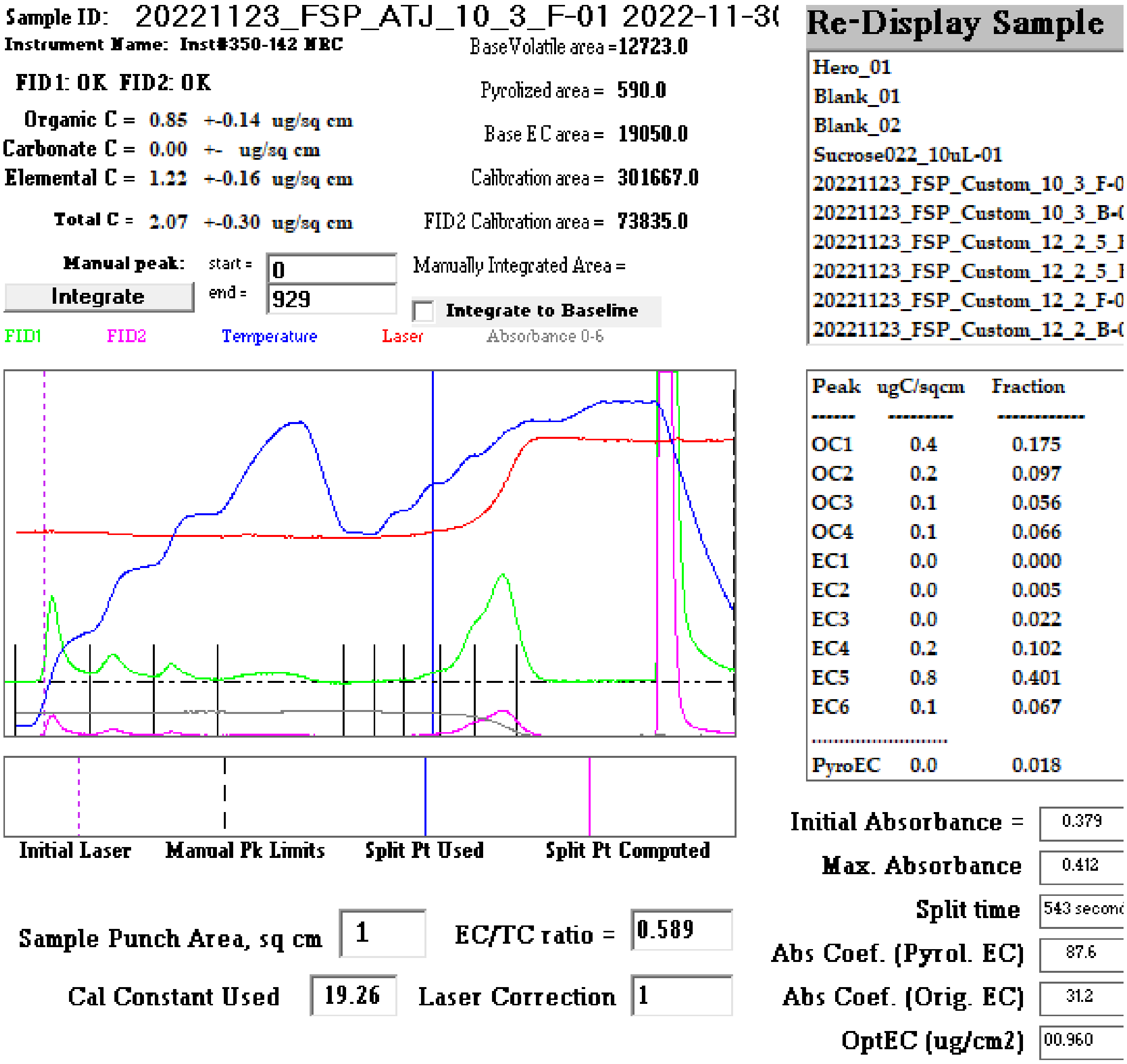

Sample ID: 20221123_FSP_ATJ_10_3_F-01 2022-11-3(

Instrument Name: Inst#350-142 NRC

FID1: OK FID2: OK

Organic C = 0.85 +-0.14 ug/sq cm

Carbonate C = 0.00 +- ug/sq cm

Elemental C = 1.22 +-0.16 ug/sq cm

Total C = 2.07 +-0.30 ug/sq cm

Base Volatile area = 12723.0

Pyrolized area = 590.0

Base EC area = 19050.0

Calibration area = 301667.0

FID2 Calibration area = 73835.0

Manual peak: start = 0

end = 929

Manually Integrated Area =

☐ Integrate to Baseline

Re-Display Sample

Hero_01
Blank_01
Blank_02
Sucrose022_10uL-01
20221123_FSP_Custom_10_3_F-0
20221123_FSP_Custom_10_3_B-(
20221123_FSP_Custom_12_2_5_I
20221123_FSP_Custom_12_2_5_I
20221123_FSP_Custom_12_2_F-0
20221123_FSP_Custom_12_2_B-(

Peak	ugC/sqcm	Fraction
OC1	0.4	0.175
OC2	0.2	0.097
OC3	0.1	0.056
OC4	0.1	0.066
EC1	0.0	0.000
EC2	0.0	0.005
EC3	0.0	0.022
EC4	0.2	0.102
EC5	0.8	0.401
EC6	0.1	0.067
PyroEC	0.0	0.018

Sample Punch Area, sq cm 1

EC/TC ratio = 0.589

Cal Constant Used 19.26

Laser Correction 1

Initial Absorbance = 0.379

Max. Absorbance 0.412

Split time 543 second

Abs Coef. (Pyrol. EC) 87.6

Abs Coef. (Orig. EC) 31.2

OptEC (ug/cm2) 00.960

Figure A21: Detailed TOA elemental, organic, and total carbon results for the 2nd set of a ATJ 10/3.00 flame condition.

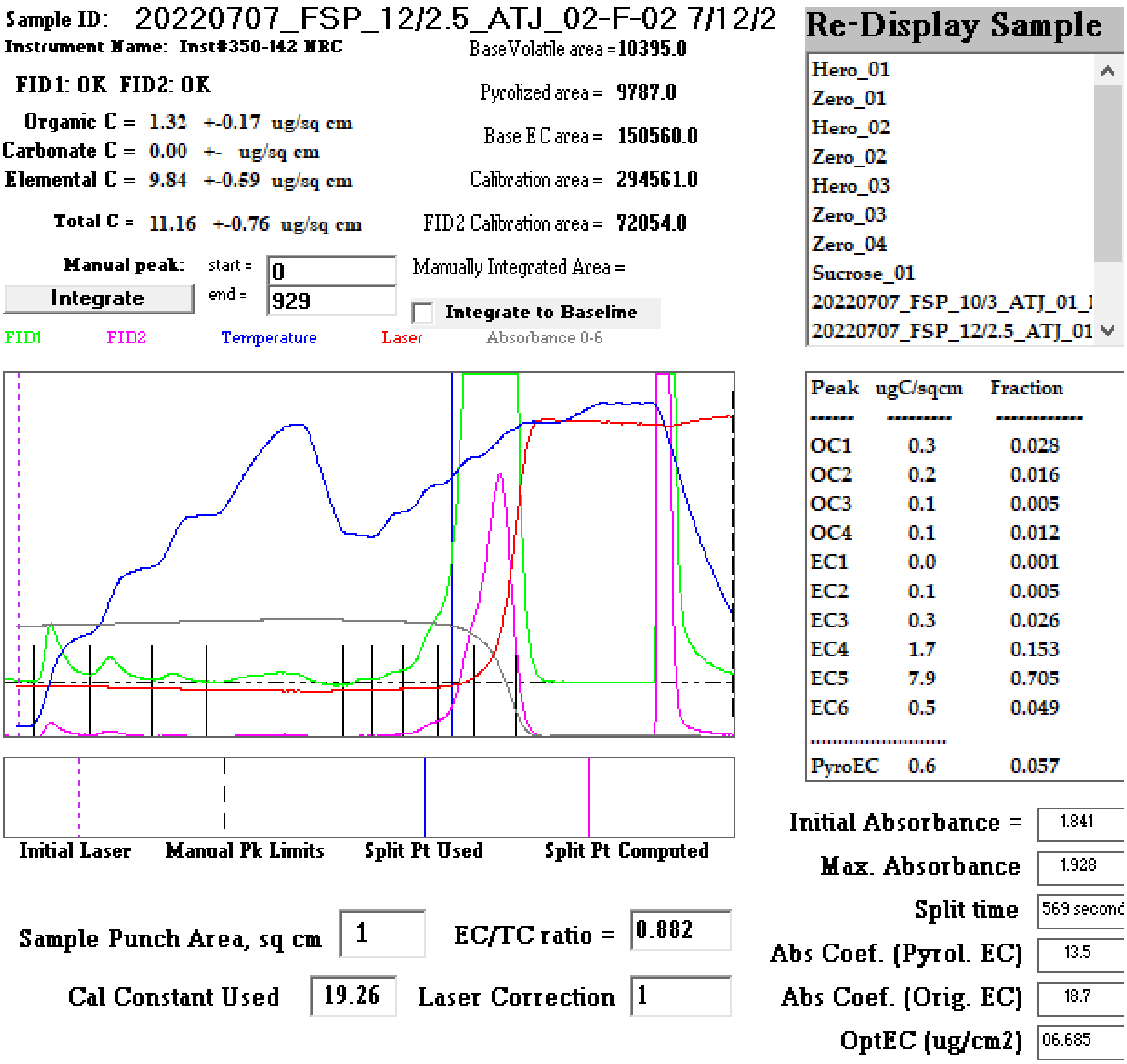

Sample ID: 20220707_FSP_12/2.5_ATJ_02-F-02 7/12/2
Instrument Name: Inst#350-142 NRC
FID1: OK FID2: OK
Organic C = 1.32 +-0.17 ug/sq cm
Carbonate C = 0.00 +- ug/sq cm
Elemental C = 9.84 +-0.59 ug/sq cm
Total C = 11.16 +-0.76 ug/sq cm
Manual peak: start = 0 end = 929
Base Volatile area = 10395.0
Pyrolized area = 9787.0
Base EC area = 150560.0
Calibration area = 294561.0
FID2 Calibration area = 72054.0
Manually Integrated Area =

Hero_01
Zero_01
Hero_02
Zero_02
Hero_03
Zero_03
Zero_04
Sucrose_01
20220707_FSP_10/3_ATJ_01_
20220707_FSP_12/2.5_ATJ_01

Peak	ugC/sqcm	Fraction
OC1	0.3	0.028
OC2	0.2	0.016
OC3	0.1	0.005
OC4	0.1	0.012
EC1	0.0	0.001
EC2	0.1	0.005
EC3	0.3	0.026
EC4	1.7	0.153
EC5	7.9	0.705
EC6	0.5	0.049
PyroEC	0.6	0.057

Sample Punch Area, sq cm 1
EC/TC ratio = 0.882
Cal Constant Used 19.26
Laser Correction 1
Initial Absorbance = 1.841
Max. Absorbance 1.928
Split time 569 second
Abs Coef. (Pyrol. EC) 13.5
Abs Coef. (Orig. EC) 18.7
OptEC (ug/cm2) 06.685

Figure A22: Detailed TOA elemental, organic, and total carbon results for the 1st set of a ATJ 12/2.50 flame condition.

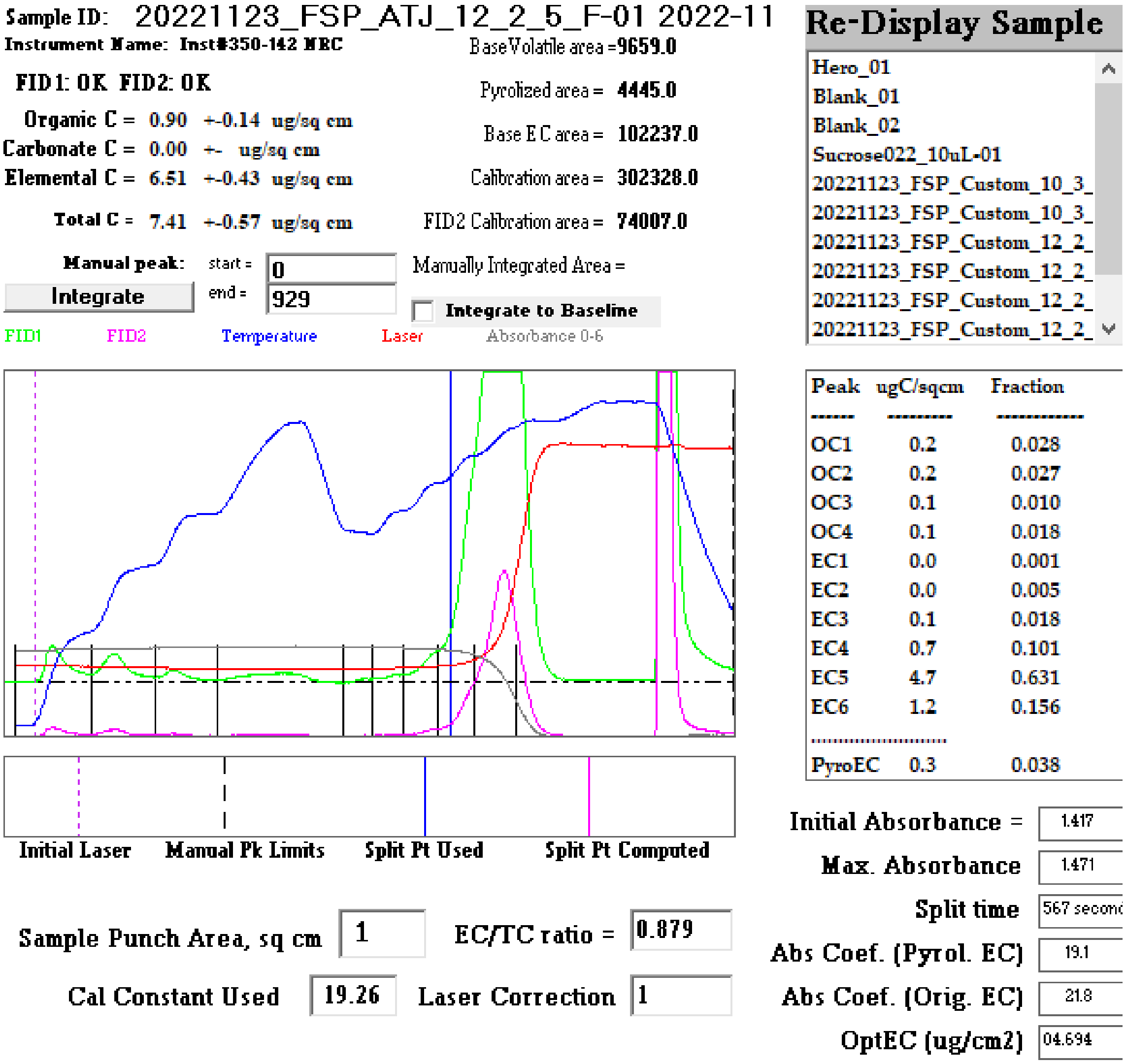

Sample ID: 20221123_FSP_ATJ_12_2_5_F-01 2022-11

Instrument Name: Inst#350-142 NRC

FID1: OK FID2: OK

Organic C = 0.90 +-0.14 ug/sq cm

Carbonate C = 0.00 +- ug/sq cm

Elemental C = 6.51 +-0.43 ug/sq cm

Total C = 7.41 +-0.57 ug/sq cm

Base Volatile area = 9659.0

Pyrolized area = 4445.0

Base E C area = 102237.0

Calibration area = 302328.0

FID2 Calibration area = 74007.0

Manual peak: start = 0 end = 929

Manually Integrated Area =

☐ Integrate to Baseline

Peak	ugC/sqcm	Fraction
OC1	0.2	0.028
OC2	0.2	0.027
OC3	0.1	0.010
OC4	0.1	0.018
EC1	0.0	0.001
EC2	0.0	0.005
EC3	0.1	0.018
EC4	0.7	0.101
EC5	4.7	0.631
EC6	1.2	0.156
PyroEC	0.3	0.038

Initial Absorbance = 1.417

Max. Absorbance 1.471

Split time 567 second

Abs Coef. (Pyrol. EC) 19.1

Abs Coef. (Orig. EC) 21.8

OptEC (ug/cm2) 04.694

Sample Punch Area, sq cm 1

EC/TC ratio = 0.879

Cal Constant Used 19.26

Laser Correction 1

Figure A23: Detailed TOA elemental, organic, and total carbon results for the 2nd set of a ATJ 12/2.50 flame condition.

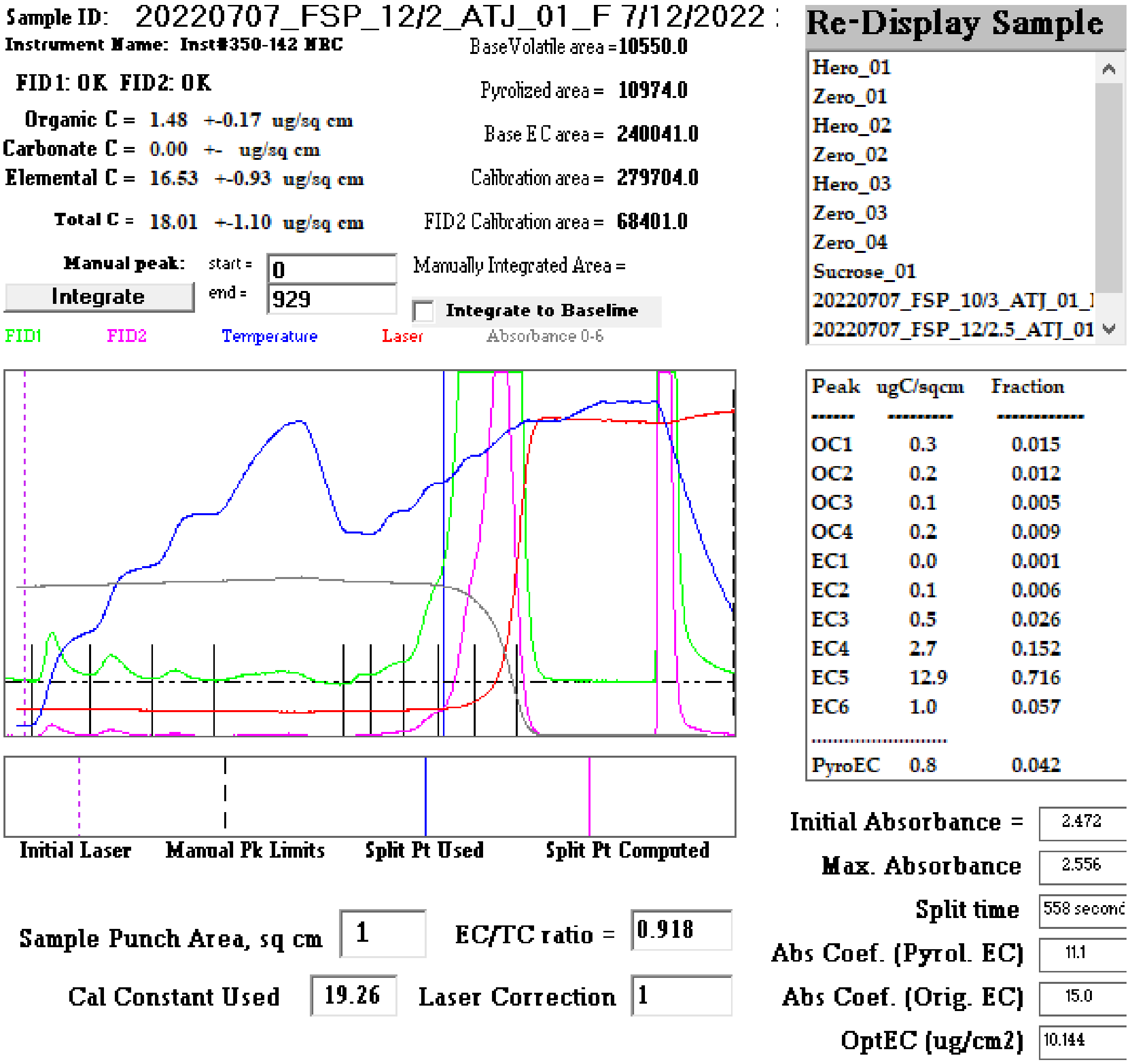

Sample ID: 20220707_FSP_12/2_ATJ_01_F 7/12/2022 :

Instrument Name: Inst#350-142 NBC

FID1: OK FID2: OK

Organic C = 1.48 +-0.17 ug/sq cm

Carbonate C = 0.00 +- ug/sq cm

Elemental C = 16.53 +-0.93 ug/sq cm

Total C = 18.01 +-1.10 ug/sq cm

Base Volatile area = 10550.0

Pyrolized area = 10974.0

Base E C area = 240041.0

Calibration area = 279704.0

FID2 Calibration area = 68401.0

Manual peak: start = 0

end = 929

Manually Integrated Area =

☐ Integrate to Baseline

Peak	ugC/sqcm	Fraction
OC1	0.3	0.015
OC2	0.2	0.012
OC3	0.1	0.005
OC4	0.2	0.009
EC1	0.0	0.001
EC2	0.1	0.006
EC3	0.5	0.026
EC4	2.7	0.152
EC5	12.9	0.716
EC6	1.0	0.057
PyroEC	0.8	0.042

Initial Absorbance = 2.472

Max. Absorbance 2.556

Split time 558 seconc

Abs Coef. (Pyrol. EC) 11.1

Abs Coef. (Orig. EC) 15.0

OptEC (ug/cm2) 10.144

Sample Punch Area, sq cm 1

EC/TC ratio = 0.918

Cal Constant Used 19.26

Laser Correction 1

Figure A24: Detailed TOA elemental, organic, and total carbon results for the 1st set of a ATJ 12/2.00 flame condition.

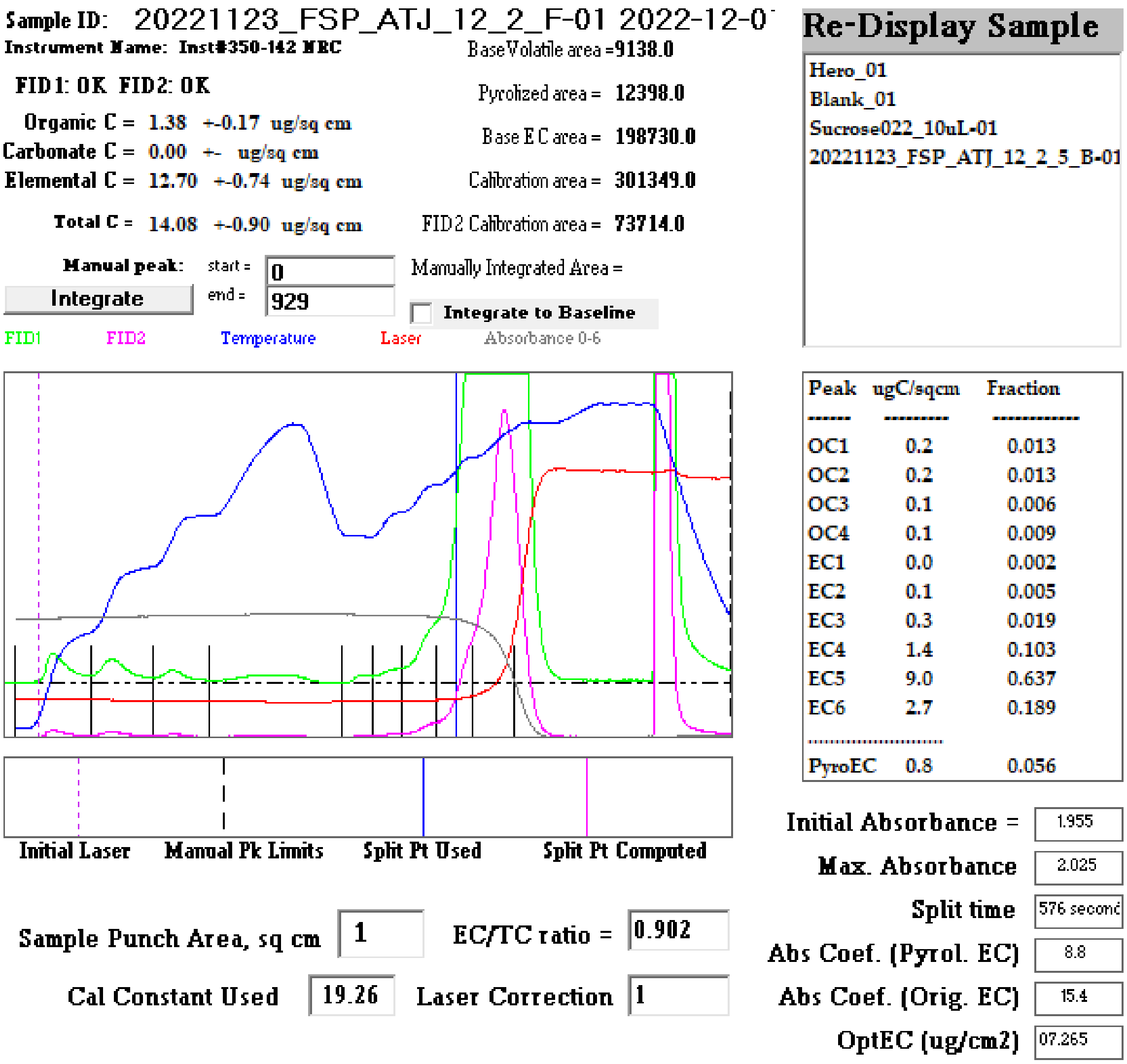

Sample ID: 20221123_FSP_ATJ_12_2_F-01 2022-12-0

Instrument Name: Inst#350-142 NRC

FID1: OK FID2: OK

Organic C = 1.38 +-0.17 ug/sq cm

Carbonate C = 0.00 +- ug/sq cm

Elemental C = 12.70 +-0.74 ug/sq cm

Total C = 14.08 +-0.90 ug/sq cm

Base Volatile area = 9138.0

Pyrolized area = 12398.0

Base EC area = 198730.0

Calibration area = 301349.0

FID2 Calibration area = 73714.0

Manual peak: start = 0 end = 929

Manually Integrated Area =

☐ Integrate to Baseline

Hero_01
Blank_01
Sucrose022_10uL-01
20221123_FSP_ATJ_12_2_5_B-01

Peak	ugC/sqcm	Fraction
OC1	0.2	0.013
OC2	0.2	0.013
OC3	0.1	0.006
OC4	0.1	0.009
EC1	0.0	0.002
EC2	0.1	0.005
EC3	0.3	0.019
EC4	1.4	0.103
EC5	9.0	0.637
EC6	2.7	0.189
PyroEC	0.8	0.056

Sample Punch Area, sq cm: 1

EC/TC ratio = 0.902

Cal Constant Used: 19.26

Laser Correction: 1

Initial Absorbance = 1.955

Max. Absorbance: 2.025

Split time: 576 second

Abs Coef. (Pyrol. EC): 8.8

Abs Coef. (Orig. EC): 15.4

OptEC (ug/cm2): 07.265

Figure A25: Detailed TOA elemental, organic, and total carbon results for the 2nd set of a ATJ 12/2.00 flame condition.

Appendix B - FSP Start-up and Shutdown Procedure

Startup Procedure:

1. Turn on Computer, SMPS (Electrostatic Classifier and Particle Counter) devices
    a. Power button on the front of the PC, power switch on back of Electrostatic Classifier and Particle Counter
    b. Turn the key and hit X-ray button on Electrostatic Classifier
    c. Sign into PC (password: Test1234)

2. Plug in CO_2 analyzer power cables

3. Turn on pump & controllers
    a. Turn on right power bar
    b. Turn on Teledyne pump
    c. Turn on D-series pump controller

4. Turn on water (4 valves on back wall)
    a. Turn on LS-FSR cooling water, or wait until about to ignite pilot flame
    b. Make sure once LS-FSR burner flow is switched, there is flow in the two flow meters (just below max)

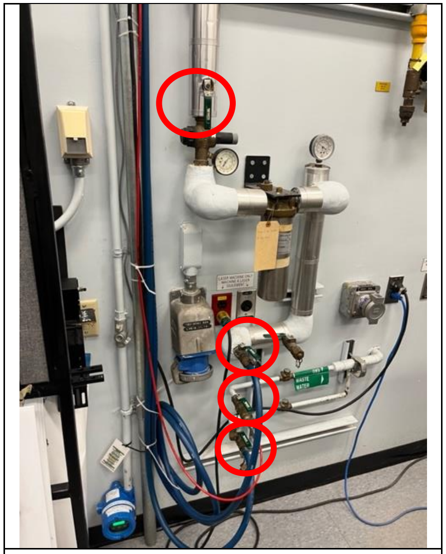

Water valves on back wall

5. Turn on air
    a. Open green valve and make pressure 40 psi.
    b. Return to station and turn air valve (pressure should be 35 psi)
    c. Double check wall supply pressure and correct to 40 psi if needed
    d. Double check Dekati pressure gauge is set 35 psi. Adjust variable dial valve if necessary

Compressed air Valve on Back wall

6. Remove foam from FSP burner

7. Unwrap quartz glass tube

8. Log in DAQ to power and to laptop
    a. Record Data using DAQ, ensure channels are on with proper units and ranges, check to ensure data is collecting properly (no high variance, data accurate to current CO2 readings on analyzer)

9. Open gas canisters off safety

Compressed Gas Canisters

10. Once SMPS is warmed up, launch AIM 10 on Windows computer
    a. Select new, then AIM file from your last operation, change the Date, and Ok
    b. Change the scan time to 45 Seconds, and hit ‘set to Max Range’

11. To start fume hood, set louver dial to 100% and hit start on High option

12. Refill the pump
    a. Have arrows on valve facing downward
    b. Refill until bottle is almost empty
    c. Flip valve so arrows pointing upwards
    d. Set to constant flow

Fuel Pump valve

13. Turn on vacuum pump

14. Open methane and oxygen valve for pilot flame

15. Adjust oxygen pressure to 2 bar (this needs to be repeated each time the dispersion oxygen is changed)

16. Pump fuel with the “Run” key

Pump Controller

17. Open Nitrogen valve

18. Begin recording data (AIM 10 and DAQ)

Shut Down Procedure:

1. Stop fuel flow from pump

2. Close gas cylinder valves to stop pilot flame and nitrogen flow

3. Shut off vacuum pump

4. Empty fuel pump
    a. With valve pointed upwards, refill the pump for 75 ml to empty the line
    b. Flip valve to point downward, and pump fuel into the bottle at a constant flow of 150 mL
    c. Once pump is empty, flip valve back up and refill pump with 50ml of air
    d. Once again flip valve down and pump air into fuel bottle to clear line
    e. Pull hose out of fuel bottle, pinching the paper towel around it to absorb fuel on outside of the tubing
    f. Wrap hose tip in paper towel
    g. Cap fuel and return to the flammable liquids cabinet

5. Power down controllers
    a. Flick pump controller to standby
    b. Turn off pump
    c. Turn off right power bar

6. Unplug CO_2 analyzer

7. Turn off and unplug DAQ

8. Export data from DAQ using SD card

9. Turn off SMPS
    a. Turn x-ray neutralizer key to off position
    b. Power off using switches on the back of the Particle Counter and Electrostatic Analyzer

10. Export SMPS data from computer (using USB)

11. Turn off computer

12. Close compressed gas valves (both on Dekati supply line, and on wall)

13. Shut off water (burner supply valves, and 4 valves on wall for supply and returns)

14. Shut down exhaust hood
    a. Hit stop on fume hood control panel.
    b. Close louver control dial to 0%.

15. Close compressed gas cylinders

16. Remove glass tube from burner and clean
    a. Clean glass, burner and probe tip using paper towel and ethanol
    b. Wrap glass in the paper it was removed from

17. Place foam on burner surface to protect from settling particles